LBNL-39873
UC-404

ERNEST ORLANDO LAWRENCE
BERKELEY NATIONAL LABORATORY

A Study of Non-Equilibrium Phonons in GaAs/AlAs Quantum Wells

Zhenpeng Su
Materials Sciences Division

November 1996
Ph.D. Thesis

LBNL-39873
UC-404

A Study of Non-Equilibrium Phonons in GaAs/AlAs Quantum Wells

Zhenpeng Su
Ph.D. Thesis

Department of Physics
University of California, Berkeley

and

Materials Sciences Division
Ernest Orlando Lawrence Berkeley National Laboratory
University of California
Berkeley, CA 94720

November 1996

This work was supported by the Director, Office of Energy Research, Office of Basic Energy Sciences, Materials Sciences Division, of the U.S. Department of Energy under Contract No. DE-AC03-76SF00098.

A Study of Non-Equilibrium Phonons in GaAs/AlAs Quantum Wells

by

Zhenpeng Su

B.S. (University of Science and Technology of China) 1988

M.A. (University of California at Berkeley) 1992

A dissertation submitted in partial satisfaction of

the requirements for the degree of

Doctor of Philosophy

in

Physics

in the

GRADUATE DIVISION

of the

UNIVERSITY of CALIFORNIA at BERKELEY

Committee in charge:

Professor Peter Y. Yu, Chair

Professor Steven G. Louie

Professor T. Kenneth Gustafson

1996

A Study of Non-Equilibrium Phonons in GaAs/AlAs Quantum Wells

by

Zhenpeng Su

Abstract

A Study of Non-Equilibrium Phonons in GaAs/AlAs Quantum Wells

by

Zhenpeng Su

Doctor of Philosophy in Physics

University of California at Berkeley

Professor Peter Y. Yu, Chair

In this thesis we have studied the non-equilibrium phonons in GaAs/AlAs quantum wells via Raman scattering. We have demonstrated experimentally that by taking into account the time-reversal symmetry relation between the Stokes and anti-Stokes Raman cross sections, one can successfully measure the non-equilibrium phonon occupancy in quantum wells. Using this technique, we have studied the subject of resonant intersubband scattering of optical phonons. We find that interface roughness plays an important role in resonant Raman scattering in quantum wells. The lateral size of the smooth regions in such interface is estimated to be of the order of 100 Å. Through a study of photoluminescence of GaAs/AlAs quantum wells under high intensity laser excitation, we have found that band nonparabolicity has very little effect on the electron subband energies even for subbands as high as a few hundred meV above the lowest one. This finding may require additional theoretical study to understand its origin. We have also studied phonon confinement and propagation in quantum wells. We show that Raman scattering of non-equilibrium phonons in quantum wells can be a sensitive measure of the spatial extent of the longitudinal optical (LO) phonons. We deduce the coherence length of LO phonons in GaAs/$Al_xGa_{1-x}As$ quantum wells as a function of the Al concentration x.

Table of Contents

Acknowledgments

I am most indebted to my advisor, Professor Peter Y. Yu, for his guidance and support throughout the course of this dissertation research.

My colleagues Drs. Tony Chen and Keith Wald had been very helpful when I first started to work in the laboratory. Dr. Tobias Ruf's excellent lab notes were also very helpful to me. Dr. K. T. Chan kindly provided us with the GaAs/AlAs quantum well samples. Collaboration with Dr. D. S. Kim on the study of phonon confinement and propagation in quantum wells is gratefully acknowledged.

Everett Lipman and Drs. Tom Donnelly and Martin Hoffer in Professor Falcone's group deserve many of my thanks for giving me the laser recipe and loaning me equipment when I was constructing a cw/self-modelocked Ti:sapphire laser.

I am also grateful to Keith Schwab in Professor Packard's group for loaning me vacuum equipment.

Finally I would like to thank my wife Xiaohong Sun, for all her love and support that eventually lead to the completion of this dissertation.

Chapter I: Introduction

When we talk about hot phonons or non-equilibrium phonons, we usually refer to phonons created during the relaxation of energetic carriers in solids. For example., when a voltage is applied to a semiconductor device, electrons in the device will be accelerated and therefore gain a large amount of kinetic energy. These electrons are often referred to as hot electrons because if we assume that they reach a quasi-thermal equilibrium among themselves, then the characteristic temperature of these electrons will be much higher than that of the surrounding crystal lattice. The imbalance in temperature between the electrons and the lattice necessarily results in the electrons losing some of their energy to the lattice, thereby creating phonons. Phonons created in this way will have certain distribution in momentum space because of the requirement of conservation of energy and quasi-momentum during the hot electron relaxation process. Therefore phonons of different wave vectors may have different occupancies. These phonons are clearly not in thermal equilibrium, so they are often called hot phonons or non-equilibrium phonons. The relaxation of hot electrons to create hot phonons is achieved through electron-phonon interaction, a process which also determines some of the important properties of many devices, like carrier mobility. Because of their relevance to practical device applications, hot electron relaxation and electron-phonon interaction have attracted a lot of research interests from both theoreticians and experimentalists [1].

With the availability of picosecond and femtosecond lasers, ultrafast optical spectroscopy has come to play an important role in the study of electron-phonon

interactions. Hot electrons can be easily generated via photoexcitation using laser pulses to mimic the excitation of hot electrons by the electric field in real devices. It has been known that immediately after they are created, hot electrons can thermalize to reach an quasi-equilibrium distribution on a time scale of 0.1 picosecond or less. Then the hot electron gas starts to cool down by emitting hot phonons on a time scale of 0.1 picosecond. These phonons have typical lifetimes of a few picoseconds as a result of decaying into acoustic phonons. Picosecond and sub-picosecond Raman spectroscopy using ultrafast lasers has proven to be a very powerful tool in studying hot phonons in bulk GaAs [2,3]. With the ever increasing use of devices based on semiconductor quantum wells and superlattices, it is natural to extend the technique of Raman scattering to study non-equilibrium phonons in these microstructures. However, when compared to bulk GaAs, quantum wells introduce many new complications and challenges.

The formation of quantum wells modifies both the electron and phonon structure, it also modifies the electron-phonon interaction. There are three prevailing theoretical models about the confined longitudinal optical (LO) phonons in quantum wells in the literature, namely the "slab model" [4], the "guided-mode model" [5] and the "Huang-Zhu model" [6]. It was found that the electron LO phonon scattering rates depend strongly on the model used [7]. Therefore it is essential to experimentally test the validity of these models. In a recent paper, Tsen *et al.* [8] have suggested that the Huang-Zhu model is the only one that can successfully explain their experimental result. However, further experimental tests of this result are desirable.

We note that part of the reason that time-resolved Raman scattering has been quite successful in studying non-equilibrium phonons in bulk GaAs is that it probes phonons

whose wave vectors lie very close to the peak of non-equilibrium phonon distribution in momentum space [2]. In semiconductor quantum wells, however, only the component of wave vector parallel to the layer plane is conserved. This change in the Raman-active wave vector in quantum wells has a significant impact on Raman scattering. As we will show later in this thesis, in most cases the Raman-active wave vector lies outside of the range of those of non-equilibrium phonons. In principle, this means that Raman scattering is not capable of directly determining the occupancy of non-equilibrium phonons in quantum wells. However, we will show that intersubband scattering in quantum wells where the subband separation is close to the one LO phonon energy offers a unique opportunity to observe non-equilibrium phonons via Raman scattering. We will investigate this possibility theoretically and experimentally in this thesis.

Another challenge in studying non-equilibrium phonon lies in the resonant Raman effect. Resonant Raman scattering in quantum wells can greatly enhance the otherwise weak Raman signal, on the other hand, it was found that because of the resonant effect, the conventional way used to determine phonon occupancy in bulk GaAs failed in the case of quantum wells. This has led some researcher to question the ability of Raman scattering in probing non-equilibrium phonon in quantum wells [9].

Our interest in studying non-equilibrium phonons via Raman scattering is further stimulated by some interesting work reported recently by Kim *et al.* [10] on the subject of propagation and confinement of LO phonons in GaAs quantum wells. These authors have studied the non-equilibrium occupancy in a series of GaAs/$Al_xGa_{1-x}As$ superlattices as a function of either the Al concentration or the thickness of the $Al_xGa_{1-x}As$ barrier. They found a sudden drop in the measured phonon occupancy when the Al concentration

or the barrier thickness reaches some critical value. They have interpreted their results as being due to a transition of the LO phonon from a propagating state to a confined one in the well. However there is no theoretical underpinning of the assertion that Raman scattering is capable of determining whether a phonon is confined or propagating. In this thesis we have attempted to develop a theory which qualitatively explained the experimental results.

This thesis is organized as follows: Chapter I contains the introduction. In Chapter II, we will discuss the basic theory about electron-phonon interaction in quantum wells. Using the Huang-Zhu model of confined phonon modes, we perform a model calculation of the occupancy of non-equilibrium phonons generated by intersubband and intrasubband scattering in quantum wells. In Chapter III we present our experimental investigation of resonant intersubband scattering of optical phonons. We discuss and compare our experimental results with the theoretical predictions from Chapter II. In Chapter IV, we present our experimental investigation of highly excited GaAs/AlAs quantum wells via photoluminescence. In Chapter V, we present our investigation of the propagation and confinement of LO phonons in quantum wells. We summarize the research work in this thesis in Chapter VI.

References

[1] See for example, *Hot Carriers in Semiconductor Nanostructures: Physics and Applications*, edited by J. Shah (Academic Press, Boston, 1992).

[2] C.L. Collins and P.Y. Yu, Phys. Rev. B **30**, 4501 (1984).

[3] D. S. Kim and P. Y. Yu, Phys. Rev. B **43**, 4158 (1991).

[4] R. Fuchs and K.L. Kliewer, Phys. Rev. **140**, A2076 (1965); J.J. Licari and R. Evrard, Phys. Rev. B **15**, 2254 (1977).

[5] B.K. Ridley, Phys. Rev. B **39**, 5282 (1989); B.K. Ridley and M. Babiker, Phys. Rev. B **43**, 9096 (1991).

[6] K. Huang and B. Zhu, Phys. Rev. B **38**, 13377 (1988).

[7] S. Rudin and T. L. Reinecke, Phys. Rev. B **41**, 7713 (1990); **43**, 9298 (E) (1991).

[8] K. T. Tsen, K. R. Wald, T. Ruf, P. Y. Yu, H. Morkoç, Phys. Rev. Lett. **67** 2557 (1991).

[9] See for example, J. F. Ryan, in *Hot Carriers in Semiconductor Nanostructures: Physics and Applications*, edited by J. Shah (Academic Press, Boston, 1992).

[10] D. S. Kim, A. Bouchalkha, J. M. Jacob, J. F. Zhou, J. J. Song, and J. F. Klem, Phys. Rev. Lett. **68**, 1002 (1992); J. M. Jacob, D.S. Kim, A. Bouchalkha, J. J. Song, J. F. Klem, H. Hou, C.W. Tu, and H. Morkoç, Solid State. Commun. **91**, 721 (1994); D. S. Kim, A. Bouchalkha, J. M. Jacob, J.J. Song, J. F. Klem, H. Hou, C. W. Tu, and H. Morkoç, Phys. Rev. B **51**, 5449 (1995).

Chapter II: Resonant Intersubband Scattering of Optical Phonons in GaAs/AlAs Quantum Wells - Model Calculations

In this chapter we will study the issue of resonant generation of non-equilibrium phonons (NOP) via intersubband scattering in quantum wells (QWs) and superlattices (SLs) from a theoretical point of view. We will perform a model calculation of the electron-phonon interactions in GaAs/AlAs QWs based on the theoretical model proposed by Huang and Zhu [1] to obtain the NOP distribution in QWs and to establish a relationship between the NOP occupancy and the width of the QWs. It was suggested by Briggs and Leburton [2] that when the separation between two subbands is close to the energy of the longitudinal optical (LO) phonons, intersubband scattering will become important to the relaxation of hot electrons. This is referred to as RISOP (resonant intersubband scattering of optical phonons). Pictorially this can be visualized as electrons in an upper subband dropping almost vertically in momentum space to a lower subband, thereby creating a large number of small wave vector phonons. This problem is interesting in that here we have a unique situation where the wave vectors of the NOP are in a range that can be probed directly by Raman scattering. This is very different from most other NOP experiment in the literature. In this chapter we will quantify the suggestion of Briggs and Leburton. This chapter is organized as follows: we start out by looking at the effects of quantum confinement on electrons and phonons in QWs; then we will examine the three prevailing theoretical models in the literature for the confined phonon modes in QWs; following our discussion on the electron-phonon interactions and

the conservation of wave vector in a quasi-two dimensional system and its consequence on Raman scattering in QWs, we will perform numerical calculations to obtain the NOP distribution in momentum space due to intrasubband scattering as well as intersubband scattering in QWs. Through our model calculation, we separate the effect of intersubband and intrasubband scattering on NOP, and establish a relationship between the NOP occupancy due to intersubband scattering and the width of the QWs. This provides a test ground for our experimental investigation of RISOP which will be presented in Chapter III.

2.1 Electrons in GaAs/AlAs quantum wells

In order to carry out the model calculation, it is necessary for us to know the electron and phonon wave functions, and the electron-phonon interaction. In addition we also need to know how the momentum conservation result and Raman scattering are modified in QWs. So we begin our discussion by first examining electrons in QWs.

Semiconductor QWs and SLs are artificial microstructures fabricated by growing alternating layers of two different materials using molecular beam epitaxy (MBE) or metal-organic chemical vapor deposition (MOCVD) method. Fig. 2-1 shows schematically a GaAs/AlAs QW band structure. GaAs has a bandgap of around 1.43 eV at room temperature while AlAs has a bandgap of around 3 eV. When these two materials are brought into contact with each other, their conduction and valence bands will aligned in such a way that the AlAs conduction band is about 1 eV above that of GaAs, and the AlAs valence band is about 500 meV below that of GaAs (this is often referred to as a

type-I band alignment with a 60-40 band offset in the literature). The AlAs layers serve as barriers for both electron and hole motions along the growth direction in GaAs.

Motions of electrons in QWs and SLs along the growth direction are usually described with the envelope function model [3]. In this model the electrons are treated as particles with an effective mass m^* and an envelope wave function $\Psi_n(z)$. The energy levels E_n of the electrons due to quantum confinement can then be calculated by solving the Schrödinger equation,

$$\left[-\frac{\hbar^2}{2m^*}\frac{d^2}{dz^2}+V_h(z)\right]\Psi_n(z)=E_n\Psi_n(z) \tag{2-1}$$

where V_h is the confinement potential whose height is determined by the band offset. When the potential well is deep, like in the case of GaAs/AlAs QWs, we can approximate it by an infinitely deep well. Within this approximation the energy levels E_n and the wave functions $\Psi_n(z)$ are readily found to be:

$$E_n=\frac{\hbar^2 k_n{}^2}{2m^*}\,, \qquad k_n=n\pi/L\,, \qquad n=1,2,3,\cdots \tag{2-2}$$

and

$$\Psi_n(z)=\begin{cases}\sqrt{2/L}\cos(k_n z) & n=1,3,5,\ldots \\ \sqrt{2/L}\sin(k_n z) & n=2,4,6,\ldots\end{cases} \tag{2-3}$$

where k_n is the wave vector of the electron along the growth direction, L is the width of QW, and the center of the QW is taken to be $z=0$. Although this infinite well approximation gives slightly higher energy levels, we do not expect k_n and $\Psi_n(z)$ to be

far from their actual values for GaAs/AlAs QWs, and the simplicity of their analytic forms makes them very useful in our model calculations. In order to calculate the electron energy levels, we use the Ben Daniel-Duke model [3, 4]. In this model, the envelope functions are chosen to be either sine or cosine functions (depending on the parity) in the QWs, and they decay exponentially inside the barrier. By requiring $\Psi_n(z)$ and $\frac{1}{m^*(z)}\frac{d\Psi_n(z)}{dz}$ (the effective mass m^* is different in the well and the barrier) to be continuous at the interface, we have the following equations:

$$\cos\left(\tfrac{1}{2}k_A L_A\right) - \frac{m_B}{m_A}\frac{k_A}{k_B}\sin\left(\tfrac{1}{2}k_A L_A\right) = 0 \qquad \text{for even states,} \tag{2-4}$$

$$\cos\left(\tfrac{1}{2}k_A L_A\right) + \frac{m_A}{m_B}\frac{k_B}{k_A}\sin\left(\tfrac{1}{2}k_A L_A\right) = 0 \qquad \text{for odd states,} \tag{2-5}$$

where A and B stand for GaAs and AlAs layers respectively. After solving for the electron wave vector k, we can use Eq. (2-2) to calculate the electron energy, replacing k_n with k. The energy levels are found to depend almost exactly on the square of the subband index n, as in the infinite well case due to the fact that we have a deep QW. Another popular approach for calculating the electron energy levels in QWs is the one developed by Bastard based on the Kane model [3, 5, 6].We have also used this model to calculate the energy levels and found that for the first subband the difference in energy between these two models is less than 1%, and is therefore completely negligible. For higher subbands, Bastard's model gives lower energy levels than those of the Ben Daniel-

Duke model. A detailed discussion of the Bastard's four band model can be found in reference [3].

One should remember that despite the confinement along the growth direction, electrons are able to move freely in the plane perpendicular to the growth direction, and therefore have a free particle-like energy spectrum in the QW plane.

2.2 Phonons in quantum wells and superlattices

The formation of QWs and SLs not only changes the electronic band structure, but also dramatically modifies the phonon modes in these microstructures. Since the acoustic phonon branch of GaAs and of AlAs overlap with each other, acoustic phonons can freely propagate from one material to the other as they do in bulk materials. However, the new periodicity in the microstructure along the growth direction gives rise to a folding of the Brillouin zone, leading to a folding of the acoustic phonon dispersion curve. Acoustic phonons whose wavevector q satisfies the following condition

$$q = \frac{2m\pi}{L}, \qquad m = 1,2,\cdots,n, \tag{2-6}$$

where L is the period of QWs or SL, will be folded back to the zone center (Fig 2-2). This effect has been amply demonstrated by Raman scattering in QWs and SLs. [7]

Optical phonons in QWs or SLs, on the other hand, behave quite differently from acoustic phonons. In fact, they behave in a way much similar to confined particles in a well. We know that confinement of electrons is caused by the bandgap mismatch of the two materials forming the microstructure, creating potential wells for electrons. Similarly for optical phonons, if there is no overlap in the phonon dispersion curves of two

materials, optical phonons cannot freely propagate from one material to the other. This results in the confinement of optical phonons within the two materials. For the GaAs/AlAs QWs we have studied, the zone center longitudinal optical (LO) phonon of GaAs has an energy of 36.5 meV while the LO phonon energy in AlAs is 44 meV. Furthermore, the optical phonon dispersion curves of GaAs and AlAs do not overlap (Fig. 2-2). Therefore it can be envisioned that in GaAs/AlAs QWs the wave function of optical phonons in one material will be heavily damped in the other, leading to confinement of optical phonons within each individual layer [8]. In the ideal case of a perfect confinement, each phonon mode can be assigned a wavevector q_m given by

$$q_m = \frac{m\pi}{nd}, \qquad m = 1,2,\ldots,n, \tag{2-7}$$

where d is the monolayer thickness, and n is the number of monolayers in the individual layer.

In addition to the confined phonon modes, the presence of interfaces between GaAs and AlAs layers introduces new vibrational modes known as the interface modes. Since these modes decay exponentially away from the interfaces, they have been found to play a very important role in electron-phonon interaction in thin GaAs/AlAs QWs (well width $\leq$ 5nm). However for the samples used in our experiment, the typical well width is larger than 15 nm, therefore, contribution from interface modes can be neglected, and we shall focus on the confined phonon modes only in the rest of this thesis. Interested readers are referred to reference [9] for a discussion of interface phonons.

2.3 Macroscopic models of confined phonon modes

Although microscopic lattice dynamics calculation of the motion of atoms in QWs is possible [10], it is not very convenient to use this method to calculate the physically measurable quantities like the electron-phonon scattering rates. During the past few years, much research effort has been made to find analytical formula for the wave functions of the confined LO phonon modes. The three most popular macroscopic models proposed in the literature so far are the slab model [11], the guided mode model [12], and the Huang-Zhu model [1]. They differ mainly in their way of handling boundary conditions. In a recent paper, Knipp and Reinecke have put forward a generalized method to handle the boundary conditions [13]. Here, however, we will only limit ourselves to the discussion of the three macroscopic models mentioned above.

2.3.1 The slab model

The slab model is also known as the dielectric continuum model. In this model, the SL is treated as a stack of dielectric slabs, and at the boundary of each slab, the Maxwell's boundary conditions are imposed. Phonon modes derived from this model are divided into strictly into bulk-like confined modes and extended interface modes. It has been shown that this is true in the limit of zero phonon dispersion [1]. When phonon dispersion is taken into account, interface modes are partially mixed with the confined modes. The slab model was proposed by Fuchs and Kliewer in the 60's [11], much earlier than the advent of the SLs, and lately used by a number of researchers. Despite the discontinuous atomic displacement at the boundary, the slab model embodies most of the physics needed to describe phonon modes in QWs. The Huang-Zhu model, which we

shall actually use to do the model calculation, is just an improved dielectric continuum model. In the following paragraphs, we will give a brief description of the dielectric continuum approach.

We consider a SL structure consisting of two polar semiconductors labeled as 1 and 2. It is well known that the long-wavelength optical vibrations in an ionic crystal can be described by the phenomenological coupled equations proposed by Born and Huang [14]. Assuming that each layer is characterized by its respective dielectric function $\varepsilon_i(\omega)$, and that the dielectric function is dependent upon frequency, but independent of wave vector **k**, then for each layer we have the dielectric function:

$$\varepsilon_i(\omega) = \varepsilon_\infty \frac{\omega^2 - \omega_{LO,i}^2}{\omega^2 - \omega_{TO,i}^2}, \qquad i = 1,2 \tag{2-8}$$

where ω_{LO} and ω_{TO} are the longitudinal and transverse optical phonon frequencies. Since there is no net charge in the QW, we have

$$\nabla \cdot \mathbf{D} = \varepsilon_i(\omega) \nabla \cdot \mathbf{E} = 0 \tag{2-9}$$

where $\mathbf{E} = -\nabla\Phi$ is the electric field and $\Phi(\mathbf{r})$ is the scalar potential and can be written as $\Phi(r_{//}, z) = \exp(ik_{//}r_{//})\Phi_m(z)$. The solutions to Eq. (2-9) can be divided into the bulk-like confined modes and the interface modes. Interface modes are obtained by requiring $\nabla \cdot \mathbf{E} = 0$ and applying the electrostatic boundary conditions. Here we will only be interested in the bulk-like confined modes which satisfy $\varepsilon_i(\omega) = 0$, and therefore have a frequency of the bulk LO phonon ω_{LO}. For the confined modes in one layer, Eq. (2-9) also need to be satisfied in the other layer, therefore we have $\nabla \cdot \mathbf{E} = 0$ in the other layer.

Using the boundary conditions that $\mathbf{D}_Z$ and $\mathbf{E}_{//}$ are continuous across the interface, one can show that $\mathbf{E}$ vanishes in the other layer, Φ is a constant at the interface, and therefore can be chosen to vanish by a gauge transformation. We see immediately that other than the requirement that it vanishes at the interface, the choice of a functional form for $\Phi_m(z)$ is infinite. Historically a simple form for $\Phi_m(z)$ is chosen to be:

$$\Phi_m(z) = \begin{cases} \cos(m\pi z / L), & m = 1,3,5,\ldots \\ \sin(m\pi z / L), & m = 2,4,6,\ldots \end{cases} \tag{2-10}$$

where the center of the well is taken to be $z = 0$. Using the above equation, the atomic displacement $\mathbf{u}$ can be evaluated from the fact that it is proportional to the polarization $\mathbf{P}$, which in turn is proportional to the electric field $\mathbf{E}$. Therefore from the relationship $\mathbf{u} \propto \mathbf{E} = -\nabla\Phi_m$, we can see that u_z will have a maximum value instead of vanishing at the interface, and therefore it is discontinuous at the interface. This is the main drawback of the slab model.

2.3.2 The guided mode model

To remedy the problem associated with a discontinuity in the atomic displacements in the slab model, the guided mode model arbitrarily chooses to impose a mechanical boundary condition by requiring the ionic displacement at the interface to be zero. This implies that the electric field and potential vanish in the barrier. The confined phonons are described by the following potential,

$$\Phi_m(z) = \begin{cases} \sin(m\pi z / L), & m = 1,3,5,\ldots \\ \cos(m\pi z / L), & m = 2,4,6,\ldots \end{cases} \tag{2-11}$$

This approach has been used by Ridley [12]. The assumption of vanishing displacement at the interface automatically rules out the possibility of any interface modes. Another major problem of the guided mode model is that it does not satisfy the electromagnetic boundary conditions.

2.3.3 The Huang-Zhu model

To solve the dilemma of the discontinuity of the ionic displacement and of the electric potential, Huang and Zhu proposed an improved macroscopic dielectric continuum model [1]. Through a comparison with the results of their microscopic lattice dynamics calculations, Huang and Zhu devised a set of analytical equations to approximate their numerical results. These equations not only satisfy the electromagnetic boundary conditions, but also the continuity of the atomic displacements at the interface. The electric potentials for the asymmetric modes are given by,

$$\Phi_{m+}(z) = \sin(\mu_m \pi z / L) + C_m z / L, \qquad m = 3,5,7,\ldots \tag{2-12}$$

and for the symmetric modes,

$$\Phi_{m-}(z) = \cos(m\pi z / L) - (-1)^{m/2}, \qquad m = 2,4,6,\ldots \tag{2-13}$$

where μ_m and C_m are constants determined by the following two equations:

$$\tan(\mu_m \pi / 2) = \mu_m \pi / 2, \tag{2-14}$$

$$C_m = -2\sin(\mu_m \pi / 2). \tag{2-15}$$

Eq. (2-14) and (2-15) can be easily solved numerically, and one finds,

$\mu_3 = 2.8606, \quad \mu_5 = 4.918, \quad \mu_7 = 6.95,$

$\mu_9 = 8.9548, \quad \mu_{11} = 10.963, \ldots$

and the corresponding C values are given by,

$C_3 = 1.9523, \quad C_5 = -1.983, \quad C_7 = 1.992,$

$C_9 = -1.995, \quad C_{11} = 1.9964, \ldots$

A comparison of the phonon modes derived from the above three models with the exact microscopic model is shown in Fig. 2-3. As we can see, the Huang-Zhu model is the closest one to the microscopic model. Furthermore, recent experiments indicate that the scattering rate and NOP occupancy calculated using the Huang-Zhu model provide the best fit to the experimental results [15]. In the next section, we shall use this model to calculate the electron-phonon interaction and NOP distribution in QWs..

2.4 Electron-phonon interaction in GaAs/AlAs quantum wells

It is well established that in polar semiconductors the relaxation of energetic electrons is achieved predominantly via the Fröhlich interaction, a coupling of the electrons with the macroscopic electric field created by the motion of ions of opposite charges. The Fröhlich interaction Hamiltonian is given by [1,16]:

$$H_{ep} = \lambda V^{-1/2} \sum_{q,m} \sum_{\alpha=\pm} t_m(q) \Phi_{m\alpha}(z) \left[\exp(i\mathbf{q}\cdot\mathbf{r}) a_{m\alpha}(\mathbf{q}) + \exp(-i\mathbf{q}\cdot\mathbf{r}) a^{\dagger}_{m\alpha}(\mathbf{q}) \right] \qquad (2\text{-}16)$$

where V is the volume of the QW, $a_{n\alpha}(\mathbf{q})$ and $a^{\dagger}_{n\alpha}(\mathbf{q})$ are phonon creation and annihilation operators, $t_m(q) = (2I_m)^{-1/2}$ with I_m being

$$I_m = \frac{1}{L}\int_{-L/2}^{L/2} dz\left[q^2\Phi_m^2 + \left(\frac{d\Phi_m}{dz}\right)^2\right] \tag{2-17}$$

λ is given by

$$\lambda^2 = 4\pi e^2\hbar\omega_{LO}\left(\frac{1}{\varepsilon_\infty} - \frac{1}{\varepsilon_0}\right) \tag{2-18}$$

ε_∞ and ε_0 are the high-frequency and static dielectric constants for GaAs, ω_{LO} is the GaAs LO phonon frequency.

If we let $|n,\mathbf{k}\rangle$ denotes an electron residing in subband n and having a wavevector $\mathbf{k}$, then the relevant matrix element in our calculation that corresponds to the evolution of the combined electron and phonon state from $|n,\mathbf{k},N_q\rangle$ to $|n',\mathbf{k}',N_q \pm 1\rangle$ is

$$\left|\langle n',\mathbf{k}',N_q \pm 1|H_{ep}(m)|n,\mathbf{k},N_q\rangle\right|^2 = \left(N_q + \frac{1}{2} \pm \frac{1}{2}\right)\frac{\lambda^2}{V}t_m^2(q)\left|G_m^{n'n}\right|^2\delta_{\mathbf{k}',\mathbf{k}\mp\mathbf{q}} \tag{2-19}$$

where $H_{ep}(m)$ is the Hamiltonian for phonon mode m, $G_m^{n'n} = \langle n'|\Phi_m|n\rangle$, and $|n\rangle$ is the electron wave function given by Eq. (2-3). The explicit form of $G_m^{n'n}$ for the lowest three subbands can be found in the Appendix.

The rate for the creation and annihilation of NOP with mode number m as a result of hot electrons relaxation from subband n to subband n' can be calculated using Fermi's golden rule, and is given by the following equation

$$\frac{\partial N_q(n,n',m)}{\partial t} = \frac{2\pi}{\hbar}\sum_K \Big[\left| \langle n', \mathbf{k}-\mathbf{q}, N_q+1 | H_{ep}(m) | n, \mathbf{k}, N_q \rangle \right|^2 f_K(1-f_{K-q})$$

$$\times \delta(E_{\mathbf{K}-\mathbf{q}} - E_{\mathbf{k}} + \hbar\omega_{LO}) - \left| \langle n', \mathbf{k}+\mathbf{q}, N_q-1 | H_{ep}(m) | n, \mathbf{k}, N_q \rangle \right|^2 f_K(1-f_{K+q})$$

$$\times \delta(E_{\mathbf{k}+\mathbf{q}} - E_{\mathbf{k}} - \hbar\omega_{LO}) \Big] - \frac{N_q}{\tau} \qquad (2\text{-}20)$$

where f_k is the electron distribution function, τ is the phonon lifetime and is on the order of 10ps. The total rate of change in N_q is calculated by summing the above expression over all phonon modes and over all subbands. If we assume that the electrons are at quasi-equilibrium obeying a Boltzmann distribution and that f_k is much smaller than unity (which can be justified by the typical electron density we excite in our experiments), then by combining Eq. (2-17), (2-19) and (2-20), we arrive at the following equation:

$$\frac{\partial N_q(n,n',m)}{\partial t} = n_e \omega_{LO} \frac{e^2}{\hbar c}\sqrt{\frac{32\pi^3 m^* c^2}{k_B T}}\left(\frac{1}{\varepsilon_\infty} - \frac{1}{\varepsilon_0}\right)\frac{t_m^2(q)}{q}\frac{\exp(-E_n/k_B T)}{\sum_p \exp(-E_n/k_B T)}\left|G_m^{n'n}\right|^2$$

$$\times \Big[(N_q+1)\exp\left(-\frac{(E_{n'} - E_n + E_q + E_{LO})^2}{4E_q k_B T}\right)$$

$$- N_q \exp\left(-\frac{(E_{n'} - E_n + E_q - E_{LO})^2}{4E_q k_B T}\right)\Big] - \frac{N_q}{\tau} \qquad (2\text{-}21)$$

In the above equation, the quasi-equilibrium temperature T of the hot electrons is assumed to change with time as the hot electron gas cools down. Using the Boltzmann

distribution for a two dimensional electron gas, we can relate T and the average energy $\langle E(t)\rangle$ of an electron in the following way,

$$\langle E(t)\rangle = k_B T(t) + \sum_p \frac{E_p \exp\left(-E_p / k_B T(t)\right)}{\sum_n \exp\left(-E_n / k_B T(t)\right)} \tag{2-22}$$

Since electrons gain or lose energy to the phonon pool, any change of the electron energy will result in the creation or annihilation of phonons. Therefore, the energy loss rate of the electrons can be related to the rate of change of the NOP occupancy by the following equation,

$$\frac{\partial\left(N(t)\langle E(t)\rangle\right)}{\partial t} = -E_{LO}\sum_m \int \frac{\partial N_q(m)}{\partial t}\rho_q d^2 q + E_0 \frac{\partial N(t)}{\partial t} \tag{2-23}$$

where $N(t)$ is the total number of electrons at time t, the summation is over all the phonon modes, and ρ_q is two dimensional phonon density of states. The last term in Eq. (2-23) is the rate of energy input from the pulsed laser, E_0 is the initial excess energy of the electrons. By assuming a standard sech^2 type of intensity profile for the laser,

$$I(t) = I_0 \sec h^2\left(1.76t / \tau_L\right) \tag{2-24}$$

where τ_L is the laser pulse width, Eq. (2-23) can then be rewritten as:

$$\frac{\partial\langle E(t)\rangle}{\partial t} = -\frac{1}{2\pi n_e(t)}\sum_m \int \frac{\partial N_q(m)}{\partial t} q dq + \frac{\left(E_0 - \langle E(t)\rangle\right)}{n_e(t)}\frac{\partial n_e(t)}{\partial t} \tag{2-25}$$

where the electron density n_e of the two-dimensional electron gas is related to the laser intensity by the following equation:

$$n_e(t) \propto \int_{-\infty} I(t')dt' = \frac{n_e(\infty)}{2}\left(1+\tanh\left(1.76t/\tau_L\right)\right) \qquad (2\text{-}26)$$

By solving Eq. (2-21), (2-22) and (2-25) numerically, we can get information about NOP distribution in time and momentum space.

In carrying out the model calculation, we have chosen the laser pulse width to be 5ps, phonon lifetime to be 10ps, typical electron density to be 2×10^{10} cm^{-2}. Due to their smaller effective mass, most of the excess energy from the excitation photon goes to the electrons rather than the holes, so we have neglected the contributions from hole relaxation to the NOP. The initial excess energy of the electrons is set to be 500 meV to simulate our experimental condition. NOP occupancy is measured 5ps after the passage of the laser pulse. The material parameters used in the calculation are given in Table I.

2.5 Wavevector conservation for Raman scattering and electron relaxation in bulk materials and quantum wells

Before we proceed with our calculation, let us first examine the difference in wavevector conservation for bulk GaAs and QWs, and see how it will affect Raman scattering and NOP generated by hot electron relaxation. For Raman scattering, we need to define a scattering geometry because it determines the wave vectors of phonons probed by Raman scattering. As in most NOP experiments, we choose the quasi-backscattering geometry which is shown schematically in Fig. 2-4. Although the photon is incident on the sample at the angle of about 45°, due to the large index of refraction of GaAs (n ~ 3.5), the wave vector inside the sample is almost perpendicular to the sample surface (so named quasi-backscattering). This geometry is preferred due to the fact that in order to

excite hot electrons, photons with energy much higher than the band gap of GaAs are used, and that these photons are strongly absorbed by GaAs within an absorption depth of about 200 nm. During the Raman scattering process, energy and quasi-momentum (or equivalently wave vector) need to be conserved. Hence for a given scattering geometry, the wave vector of the phonons that participate in Raman scattering can be easily calculated from the following equations:

$$\mathbf{K}_i' - \mathbf{K}_s' = \mathbf{Q}_{ph} \tag{2-27}$$

$$\omega_i - \omega_s = \omega_{ph} \tag{2-28}$$

where $\mathbf{Q}_{ph}$ is the phonon wave vector. $\mathbf{K}_i$' and $\mathbf{K}_s$' are, respectively, the wave vectors of the incident and scattered photons *inside* GaAs, and can be related to the corresponding wave vectors $\mathbf{K}_i$ and $\mathbf{K}_s$ of photons in air via the Snell law. ω_{ph}, ω_I and ω_s are the corresponding frequencies. We use 2 eV photons (λ = 600 nm) in our experiments, so the magnitude of the wave vector $\mathbf{K}_i$ of the incident photon is $2\pi/\lambda \sim 1\times10^5$ cm^{-1}. For bulk GaAs as schematically shown in Fig. 2-4 (a), the magnitude of the wave vector $\mathbf{Q}_{ph}$ of the phonon is about $2nK_i \sim 7\times10^5$ cm^{-1}. This value happens to be very close to the peak of the NOP distribution as calculated by Collins and Yu (Fig. 2-5) [17]. This is the main reason why Raman scattering has been a powerful tool in studying NOP in bulk GaAs. For GaAs QWs and SLs (Fig.2-4(b)), the translational symmetry of the crystal lattice is only preserved in the plane parallel to the QW layers. Therefore only the component of the wave vector parallel to the QW plane is conserved. Eq. (2-27) should be modified accordingly to reflected such a change. For our experimental geometry, we find that $\mathbf{Q}_{ph//}$ is $K_i\sin\theta \sim 7\times10^4$ cm^{-1}. This value is one order of magnitude smaller than the bulk value,

and we should expect the large difference in the wave vector of phonons probed by Raman backscattering to have a dramatic impact on Raman scattering efficiency.

Another quantity that is affected by the change of wavevector conservation is the wave vector of NOP generated by hot electron relaxation. For bulk semiconductors, one mainly needs to consider intrasubband relaxation of the hot electrons, and it has been investigated in great details by Collins and Yu [17]. The formation of subbands in QWs introduces new relaxation channels for the hot electrons, i.e. intersubband scattering. NOP generated via these two channels have very different wavevector distributions. Intuitively, one can image that intrasubband relaxation of the hot electrons will produce a hot phonon distribution similar to that in bulk materials because it is determined mostly by the band curvature. On the other hand, intersubband relaxation produces a phonon distribution that depends strongly on the separation between the two subbands. To better support the above argument, we apply energy and wave vector conservation to the hot electron relaxation shown schematically in Fig. 2-6, and we obtain the following results for intrasubband scattering:

$$\frac{\sqrt{2m^*}}{\hbar}\left(\sqrt{E_k}-\sqrt{E_k-E_{LO}}\right)<Q_{ph//}<\frac{\sqrt{2m^*}}{\hbar}\left(\sqrt{E_k}+\sqrt{E_k-E_{LO}}\right), \qquad (2\text{-}29)$$

and for intersubband scattering:

$$\frac{\sqrt{2m^*}}{\hbar}\left(\sqrt{E_k}-\sqrt{E_k+\Delta-E_{LO}}\right)<Q_{ph//}<\frac{\sqrt{2m^*}}{\hbar}\left(\sqrt{E_k}+\sqrt{E_k+\Delta-E_{LO}}\right) \qquad (2\text{-}30)$$

where E_k is the kinetic energy of the hot electrons, E_{LO} and $Q_{ph//}$ are the energy and wavevector of the LO phonon respectively, and Δ is the separation between two

subbands. Assuming that E_k ~ 500 meV, we find that $Q_{phl/}$ is between 3.5×10^5 and 1.8×10^7 cm^{-1} during intrasubband scattering, while $Q_{phl/}$ is between $\frac{\sqrt{m^*}(\Delta - E_{LO})}{\hbar\sqrt{2E_k}}$ and 1.8×10^7 cm^{-1} during intersubband scattering. It can be clearly seen that when Δ is close to E_{LO}, the wave vector of the NOP can be very arbitrarily small. When we combine the above result with our previous discussion that Raman scattering in quantum wells is only sensitive to small wave vector phonons, we conclude that *for perfect two dimensional QWs, Raman backscattering is not capable of probing NOP generated by intrasubband scattering, and that it can probe NOP generated by intersubband scattering only when the subband separation is close to the LO phonon energy.*

2.6 Results of model calculations -- NOP distribution due to intersubband and intrasubband scattering

In this section we present results of our model calculations. As we pointed out earlier, all phonon modes and electron subbands should, in principle, be included in the calculation. However, this is apparently impossible to do numerically. Therefore we need to make some reasonable approximations. Since we have assumed that the electrons obey the Boltzmann distribution which decays exponentially with the electron energy, we expect that electrons in a small number of the lowest lying subbands will contribute most to the creation of NOP. In addition, we have shown in the previous section that only those subbands whose separation is close to the LO phonon energy will contribute significantly to the creation of phonons with small wavevector via intersubband

scattering. Hence we will include only the first three subbands in our calculations. As for the phonon modes, we have tried including the first five ($m = 2,3...6$) confined modes, and the results (Fig. 2-7) show that as the order of the phonon mode increases, their contribution decreases rapidly. Hence we have only included the first five phonon modes in our calculations.

The total NOP is a sum of phonons created during intersubband and intrasubband scattering. The selection rule for phonon modes that can participate in the scattering of electrons is embodied in Eq. (2-19), specifically, it is determined by $G_m^{n'n}$. Because both the electron and phonon wave functions have definite parity, it is straightforward to show that intrasubband scattering of electrons is mediated only by the creation and annihilation of even parity phonons (m = 2,4,6,...) while intersubband scattering between adjacent subbands is mediated by odd parity phonons (m = 3,5,7,...). This analysis enables us to examine the effect of intersubband and intrasubband scattering separately.

Fig.2-8 shows the NOP distribution due to intrasubband scattering calculated for a 190 Å QW. QWs with other widths show very similar NOP distribution and will not be shown here. As we can see from Fig. 2-8, despite the quasi-two dimension nature of QWs, the distribution of NOP from intrasubband scattering bears a lot of similarity to the one obtained by Collins and Yu for bulk GaAs (Fig. 2-5). There are two distinct features in this plot, namely a sharp cut-off in the NOP at phonon wavevector of around 2×10^5 cm^{-1} and a peak in the NOP at around 10^6 cm^{-1}. This can be understood from our earlier discussion about the range of NOP wave vector. Since this range is mostly determined by the excess energy of the electrons and by the electron dispersion (determined by the

effective mass of the electron which has the same value of $0.067m_e$ for bulk GaAs and GaAs QWs), we expect to see similar results. This verifies our argument that intrasubband scattering does not contribute to the creation of small wave vector phonons.

On the other hand intersubband scattering can produce a significant number of small wave vector phonons as evidenced in Fig. 2-9. The amount of phonons produced and their wave vectors depend strongly on the subband separation, or equivalently on the width of the QWs. Fig. 2-10 shows the NOP distribution due to intersubband scattering for a number of QWs. When the well width increases from 150 Å to 240 Å, the separation between the first two subbands changes from 54.2 meV to 22.4 meV. For width equal to 180 Å the subband separation of 39.5 meV is close to the LO phonon energy of 36.5 meV. Accordingly the amount of small wave vector phonons in Fig. 2-10 varies with the well width by first increasing, reaching a maximum around 180 Å and then decreasing. To better view the dependence of the NOP occupancy with the width of the well, we plot the occupancy of NOP with wave vector equal to 7×10^4 cm^{-1}, which is the wavevector probed by our Raman scattering geometry, versus the well width. As shown in Fig. 2-11, the NOP occupancy has a peak around 185 Å where the separation of the first two subbands is resonant with the LO phonon energy, and the width of this peak is about 20 Å.

In summary, we have performed a model calculation of the NOP distribution generated by hot electron relaxation in GaAs/AlAs QWs using the theoretical model of confined phonons proposed by Huang and Zhu. We show that while intrasubband scattering produces a NOP distribution similar to that of bulk GaAs, intersubband

scattering produces NOP whose distribution depends strongly on the separation of the subbands (or the width of the QW). When the separation is close to the LO phonon energy, a large number of small wave vector NOP are generated by the intersubband scattering. This phenomenon is known as RISOP. These phonons are readily accessible by Raman scattering because wave vector conservation in QWs and SLs limits Raman scattering to probing small in-plane wave vector phonons. The experimental investigation of RISOP will be presented in chapter III.

Appendix of Chapter II

Using the phonon wave function Φ_m given in Eq. (2-12), (2-13) and the electron wave function $|n\rangle$ given in Eq. (2-3), we can evaluate $G_m^{n',n}$ used in Eq. (2-19).

$$G_m^{1,1} = \langle 1|m|1\rangle = \frac{2}{L}\int_{-L/2}^{L/2} dz \cos^2(\pi z / L) \times \Phi_m$$

$$= \begin{cases} 0 & \text{m} = 3,5,7,\ldots \\ 0.5\delta_{m,2} - (-1)^{m/2} & \text{m} = 2,4,6,\ldots \end{cases}$$

$$G_m^{1,2} = G_m^{2,1} = \langle 2|m|1\rangle = \frac{2}{L}\int_{-L/2}^{L/2} dz \sin(2\pi z / L)\cos(\pi z / L) \times \Phi_m$$

$$= \begin{cases} 16C_m / 9\pi^2 - (2\mu_m / \pi)\cos(\mu_m \pi / 2) \\ \quad \times \left[1/(\mu_m^2 - 1) - 1/(\mu_m^2 - 9)\right] & \text{m} = 3,5,7,\ldots \\ 0 & \text{m} = 2,4,6,\ldots \end{cases}$$

$$G_m^{2,2} = \langle 2|m|2\rangle = \frac{2}{L}\int_{-L/2}^{L/2} dz \sin^2(2\pi z / L) \times \Phi_m$$

$$= \begin{cases} 0 & \text{m} = 3,5,7,\ldots \\ -0.5\delta_{m,4} - (-1)^{m/2} & \text{m} = 2,4,6,\ldots \end{cases}$$

$$G_m^{1,3} = G_m^{3,1} = \langle 3|m|1\rangle = \frac{2}{L}\int_{-L/2}^{L/2} dz \cos(3\pi z / L)\cos(\pi z / L) \times \Phi_m$$

$$= \begin{cases} 0 & \text{m} = 3,5,7,\ldots \\ 0.5(\delta_{m,2} + \delta_{m,4}) & \text{m} = 2,4,6,\ldots \end{cases}$$

$$G_m^{2,3} = G_m^{3,2} = \langle 3|m|2\rangle = \frac{2}{L}\int_{L/2}^{L/2} dz \cos(3\pi z/L)\sin(2\pi z/L)\times\Phi_m$$

$$= \begin{cases} -48C_m/25\pi^2 + (2\mu_m/\pi)\cos(\mu_m\pi/2) & \text{m} = 3,5,7,\ldots \\ \quad \times\left[1/(\mu_m^2-1) - 1/(\mu_m^2-25)\right] & \\ 0 & \text{m} = 2,4,6,\ldots \end{cases}$$

$$G_m^{3,3} = \langle 3|m|3\rangle = \frac{2}{L}\int_{L/2}^{L/2} dz \cos^2(3\pi z/L)\times\Phi_m$$

$$= \begin{cases} 0 & \text{m} = 3,5,7,\ldots \\ 0.5\delta_{m,6} - (-1)^{m/2} & \text{m} = 2,4,6,\ldots \end{cases}$$

We can also evaluate I_m given by Eq. (2-17).

$$I_m = \frac{1}{L}\int_{L/2}^{L/2} dz\left[q^2\Phi_m^2 + \left(\frac{d\Phi_m}{dz}\right)^2\right]$$

$$= \begin{cases} q^2\left[0.5\left(1 - \dfrac{\sin(\mu_m\pi)}{\mu_m\pi}\right) - \dfrac{2C_m}{\mu_m\pi}\cos(\mu_m\pi/2) + \dfrac{4C_m}{(\mu_m\pi)^2}\sin(\mu_m\pi/2) + C_m^2/12\right] & \\ \quad + \dfrac{1}{L^2}\left[\dfrac{(\mu_m\pi)^2}{2}\left(1 + \dfrac{\sin(\mu_m\pi)}{\mu_m\pi}\right) + 4C_m\sin(\mu_m\pi/2) + C_m^2\right] & \text{m} = 3,5,7,\ldots \\ 1.5q^2 + 0.5(m\pi/L)^2 & \text{m} = 2,4,6,\ldots \end{cases}$$

References

[1] K. Huang and B. Zhu, Phys. Rev. B **38**, 13377 (1988).

[2] S. Briggs and J.P. Leburton, Superlatt. Microstruct. **5**, 145 (1989).

[3] See for example, G. Bastard, *Wave Mechanics Applied to Semiconductor Heterostructures*, (Halsted Press, France, 1990).

[4] D.J. Ben Daniel and C.B. Duke, Phys. Rev. **152**, 683 (1966).

[5] E.O. Kane, J. Phys. Chem. Sol. **1** 249, (1957); *Physics of III-V compounds, vol. 1*, edited by R.K. Willardson and A.C. Beer (Academic Press, New York, 1966).

[6] G. Bastard, Phys. Rev. B **25**, 7584 (1982).

[7] See for example, C. Colvard, R. Merlin, M. V. Klein and A.C. Gossard, Phys. Rev. Lett. **43**, 298 (1980).

[8] See for example, B, Jusserand, D. Paquet and A. Regreny, Phys. Rev. B **30**, 6245 (1984); A. K. Sood, J. Menendez, M. Cardona, and K. Ploog, Phys. Rev. Lett. **54**, 2111 (1985).

[9] N. Mori and T. Ando, Phys. Rev. B **40**, 6175 (1989); A. K. Sood, J. Menendez, M. Cardona and K. Ploog, Phys. Rev. Lett. **54**, 2115 (1985).

[10] H. Rucker, E. Molinari, P. Lugli, Phys. Rev. B **44**, 3463 (1991); **45**, 6747 (1992); S. Baroni, P. Giannozzi, E. Molinari, and P. Lugli, Phys. Rev. B **44**, 3463 (1991).

[11] R. Fuchs and K.L. Kliewer, Phys. Rev. **140**, A2076 (1965); J.J. Licari and R. Evrard, Phys. Rev. B **15**, 2254 (1977).

[12] B.K. Ridley, Phys. Rev. B **39**, 5282 (1989); B.K. Ridley and M. Babiker, Phys. Rev. B **43**, 9096 (1991).

[13] P. A. Knipp and T. L. Reinecke, Phys. Rev. B **48**, 18037 (1993).

[14] M. Born and K. Huang, *Dynamical Theory of Crystal Lattices* (Oxford University Press, Oxford, 1954).

[15] K. T. Tsen, K. R. Wald, T. Ruf, P. Y. Yu, H. Morkoç, Phys. Rev. Lett. **67** 2557 (1991).

[16] S. Rudin and T. L. Reinecke, Phys. Rev. B **41**, 7713 (1990); **43**, 9298 (E) (1991).

[17] C.L. Collins and P.Y. Yu, Phys. Rev. B **30**, 4501 (1984).

Table I

	GaAs	**AlAs**
Effective mass of the electron	$0.067\, m_e$	$0.15\, m_e$
Effective mass of the heavy hole	$0.377\, m_e$	$0.478\, m_e$
High frequency dielectric constant ε_∞	10.9	
Low frequency dielectric constant ε_0	13.3	
Band Gap at 300 K	1.425 eV	3.04 eV
Band Gap at 77 K	1.51 eV	3.1 eV
LO phonon energy	36.5 meV	50 meV

Figure Captions for Chapter II

Fig. 2-1 A schematic diagram for the band alignment of GaAs/AlAs quantum wells.

Fig. 2-2 Phonon dispersion curves for the longitudinal phonons in bulk GaAs (solid lines) and AlAs (dashed lines). Folded acoustic phonon and confined optical phonon dispersions in a superlattice are also shown.

Fig. 2-3 The z component of the atomic displacements (u_z) and the corresponding potentials ($\Phi(z)$) for the first few GaAs-like optical phonon modes in GaAs/AlAs quantum wells. (a), (b) and (c) are from the macroscopic models and (d) is from the microscopic calculations. Reproduced from reference [2-10].

Fig. 2-4 A schematic diagram for the quasi-back scattering geometry used in Raman scattering experiments in the case of (a) bulk GaAs, (b) GaAs/AlAs quantum wells. K_i and K_s are the wave vectors of incident and scattered photons, q is the wave vector of phonons. The incident angle θ is about 45°. GaAs has an index of refraction n of about 3.5.

Fig. 2-5 Non-equilibrium phonon distribution generated by hot electrons in bulk GaAs. Shaded region indicates the wave vectors probed by Raman back scattering. Reproduced from reference [2-17].

Fig. 2-6 A schematic band diagram showing (a) intrasubband and (b) intersubband scattering of hot electrons. q_{max} and q_{min} denote the maximum and minimum wave vector of phonons created by hot electrons with energy E_k. E_{LO} is the energy of the LO phonon.

Fig. 2-7 Non-equilibrium phonon distribution due to intrasubband and intersubband scattering for different phonon modes calculated for a 190 Å GaAs/AlAs quantum well using the Huang-Zhu model.

Fig. 2-8 Non-equilibrium phonon distribution due to intrasubband scattering calculated for a 190 Å GaAs/AlAs quantum well using the Huang-Zhu model. The vertical dashed line indicates the wave vector probed by Raman back scattering.

Fig. 2-9 Non-equilibrium phonon distribution due to intersubband scattering calculated for a 190 Å GaAs/AlAs quantum well using the Huang-Zhu model. The vertical dashed line indicates the wave vector probed by Raman back scattering.

Fig. 2-10 Non-equilibrium phonon distribution due to intersubband scattering calculated for GaAs/AlAs quantum wells of various well widths. The vertical dashed line indicated the wave vector probed by Raman back scattering.

Fig. 2-11 The occupation number of non-equilibrium phonon at wave vector 7×10^4 cm^{-1} generated by intersubband scattering of hot electrons as a function of the quantum well width. The "resonant" effect is clearly shown to occur around well width 185 Å.

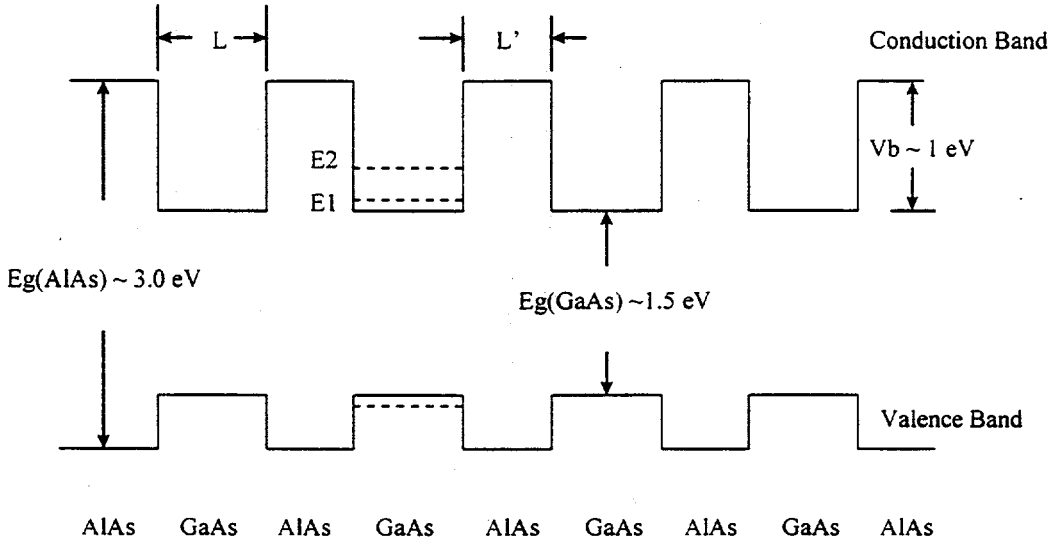
L
L'
Conduction Band
E2
E1
Vb ~ 1 eV
Eg(AlAs) ~ 3.0 eV
Eg(GaAs) ~1.5 eV
Valence Band
AlAs
GaAs
AlAs
GaAs
AlAs
GaAs
AlAs
GaAs
AlAs

Figure 2 - 1

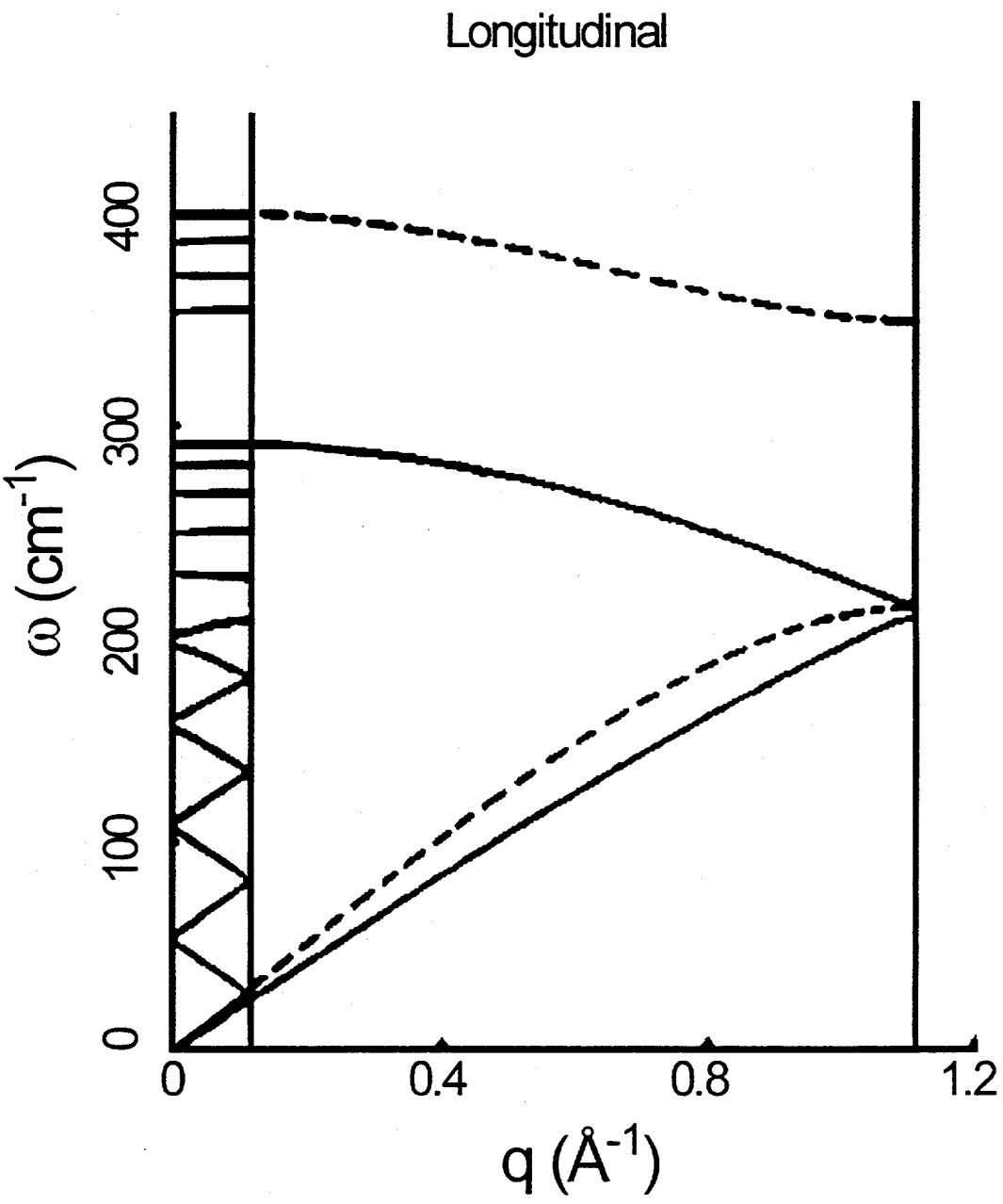

Figure 2 - 2

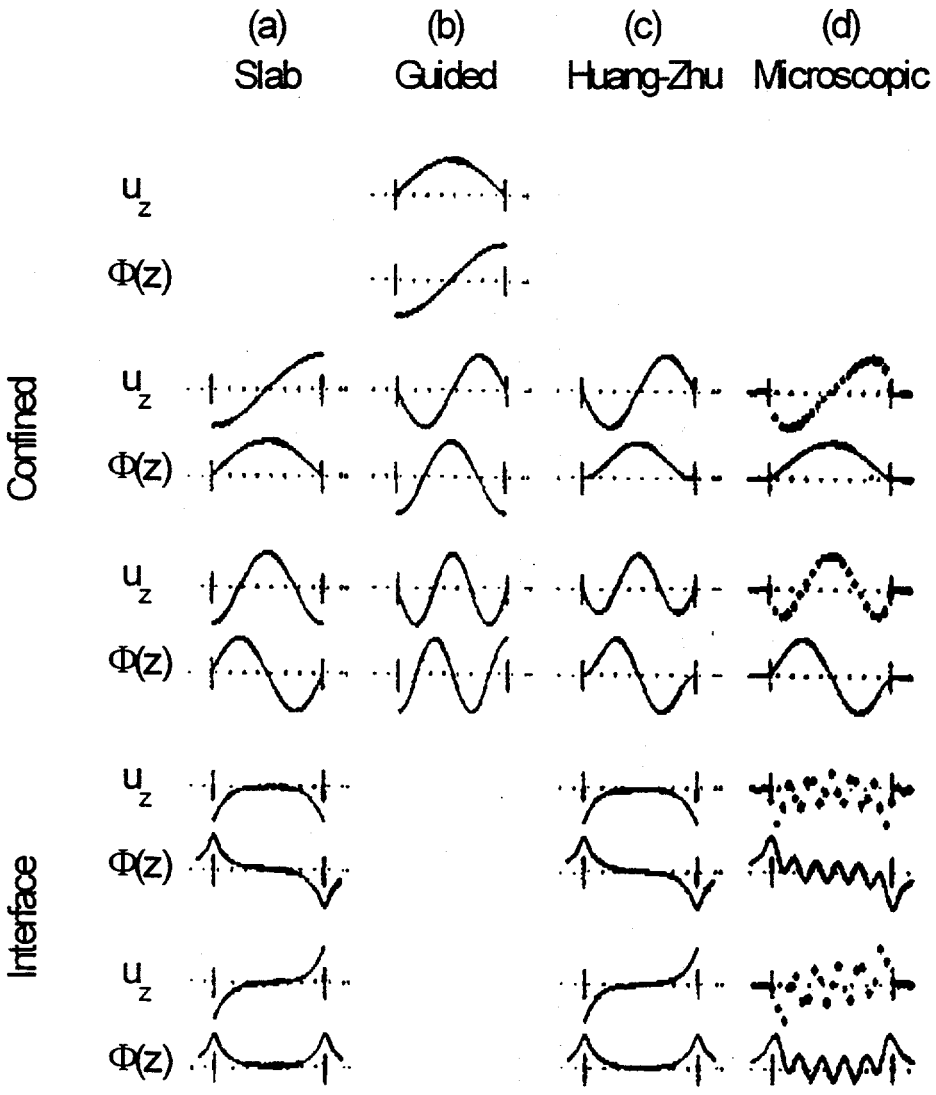
(a)
Slab
(b)
Guided
(c)
Huang-Zhu
(d)
Microscopic
Confined
Interface
u_z
$\Phi(z)$

Figure 2 - 3

Raman Backscattering

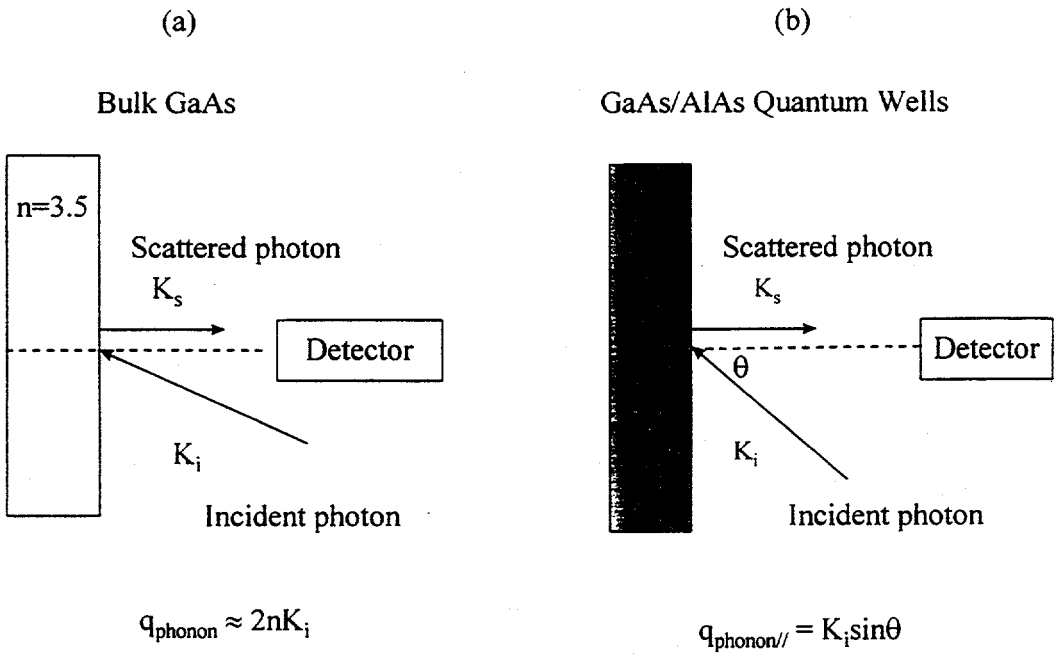

Figure 2 - 4

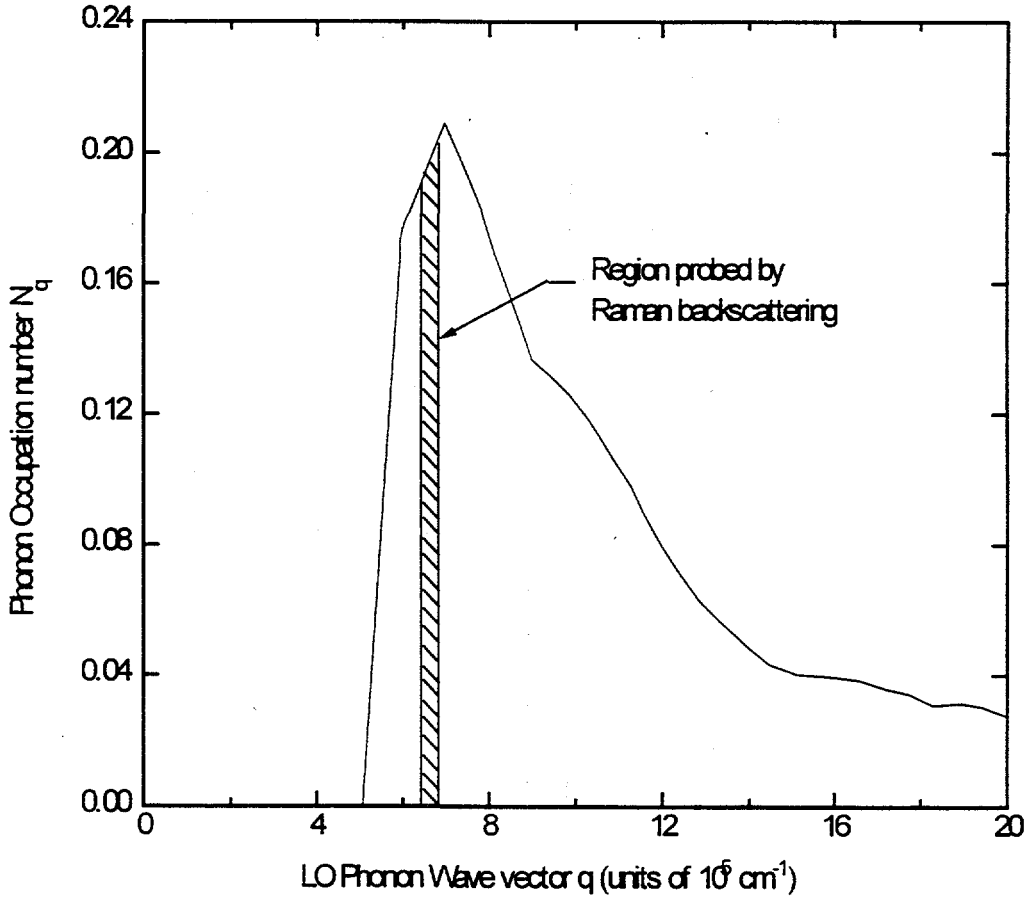
0.24
0.20
0.16
0.12
0.08
0.04
0.00
Phonon Occupation number N_q
Region probed by
Raman backscattering
0
4
8
12
16
20
LO Phonon Wave vector q (units of 10^6 cm^{-1})

Figure 2 - 5

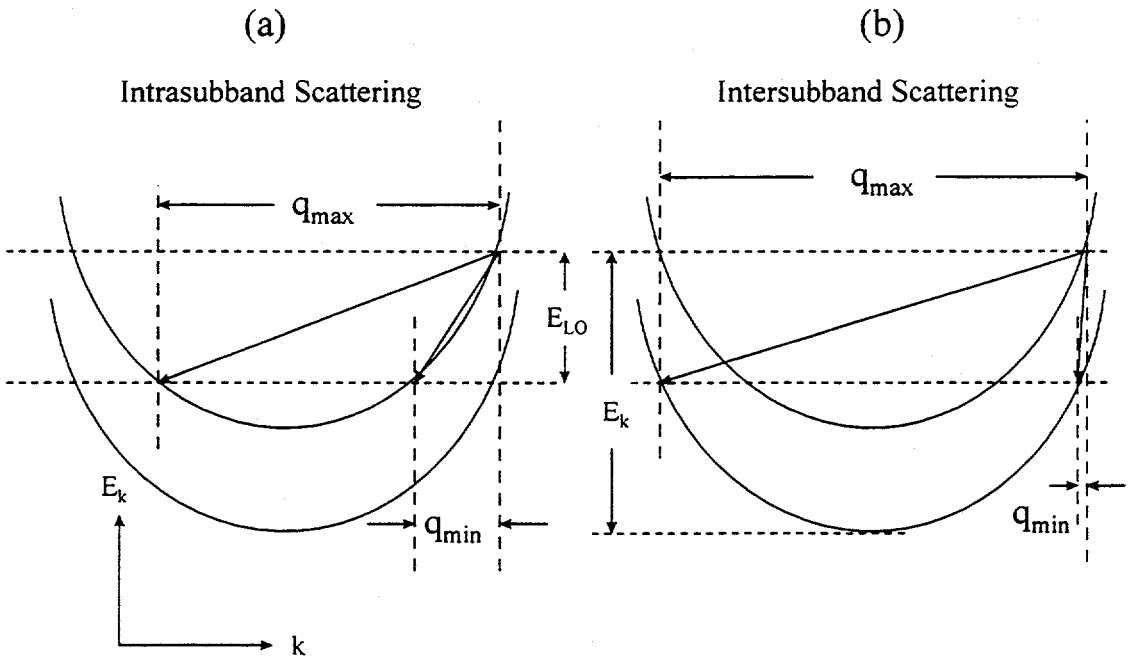
(a)
Intrasubband Scattering
q_{max}
E_{LO}
E_k
q_{min}
k
(b)
Intersubband Scattering
q_{max}
E_k
q_{min}

Figure 2 - 6

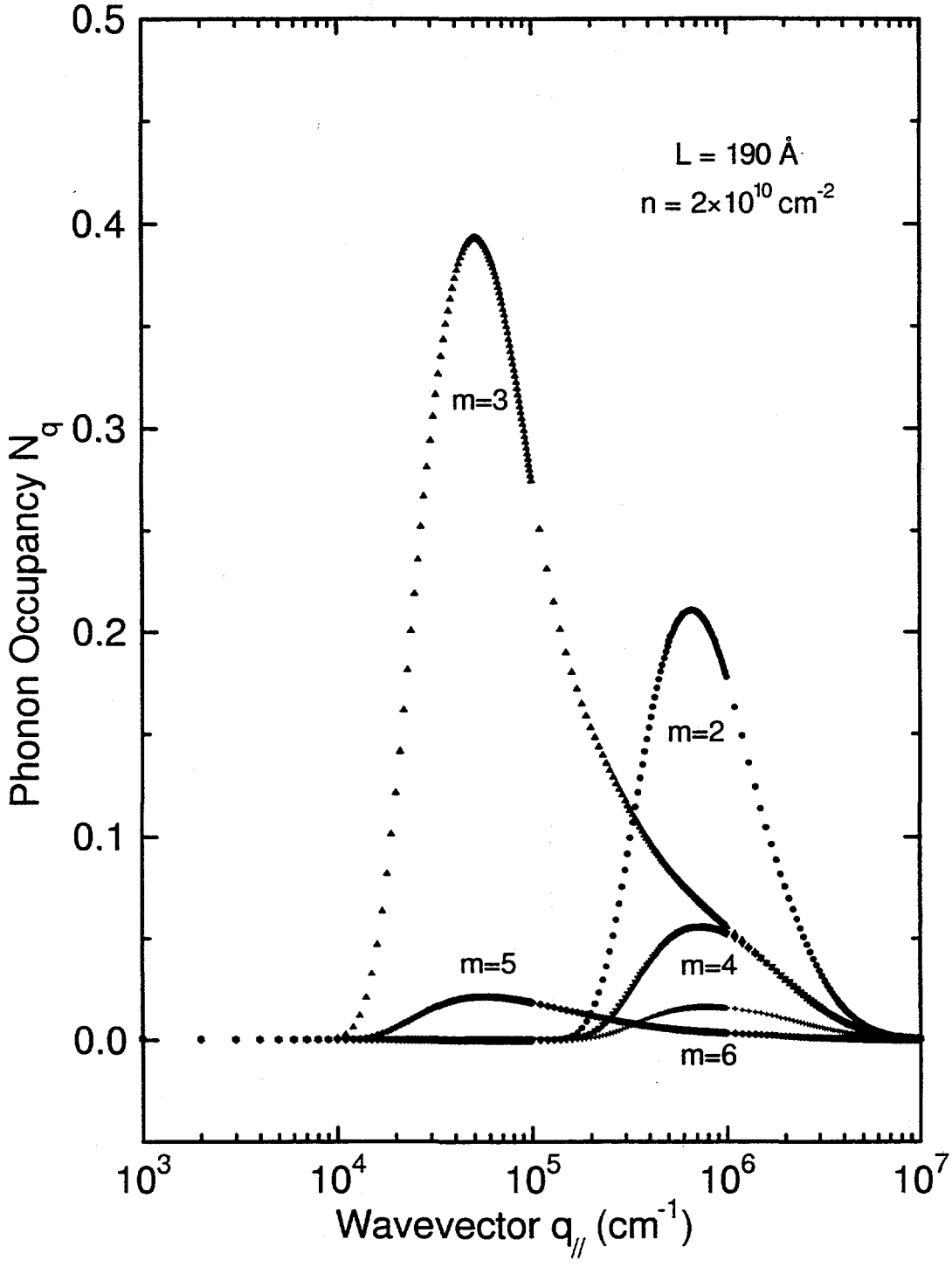
L = 190 Å
n = 2×10^10 cm^-2
m=3
m=2
m=5
m=4
m=6
Phonon Occupancy N_q
Wavevector q_// (cm^-1)
0.5
0.4
0.3
0.2
0.1
0.0
10^3
10^4
10^5
10^6
10^7

Figure 2 - 7

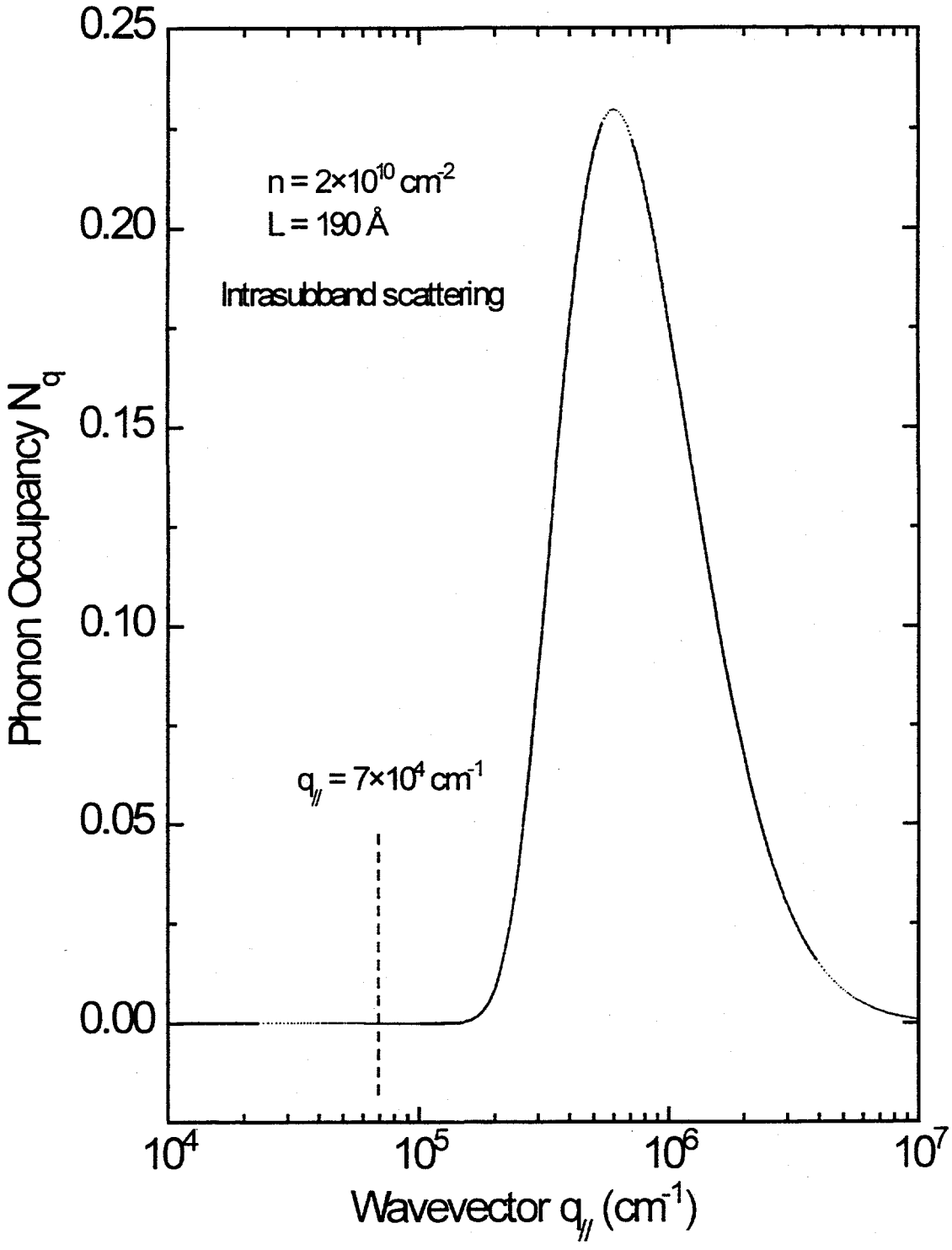
0.25
0.20
0.15
0.10
0.05
0.00
Phonon Occupancy N_q
$n = 2\times10^{10}$ cm^{-2}
L = 190 Å
Intrasubband scattering
$q_{//} = 7\times10^{4}$ cm^{-1}
10^4
10^5
10^6
10^7
Wavevector $q_{//}$ (cm^{-1})

Figure 2 - 8

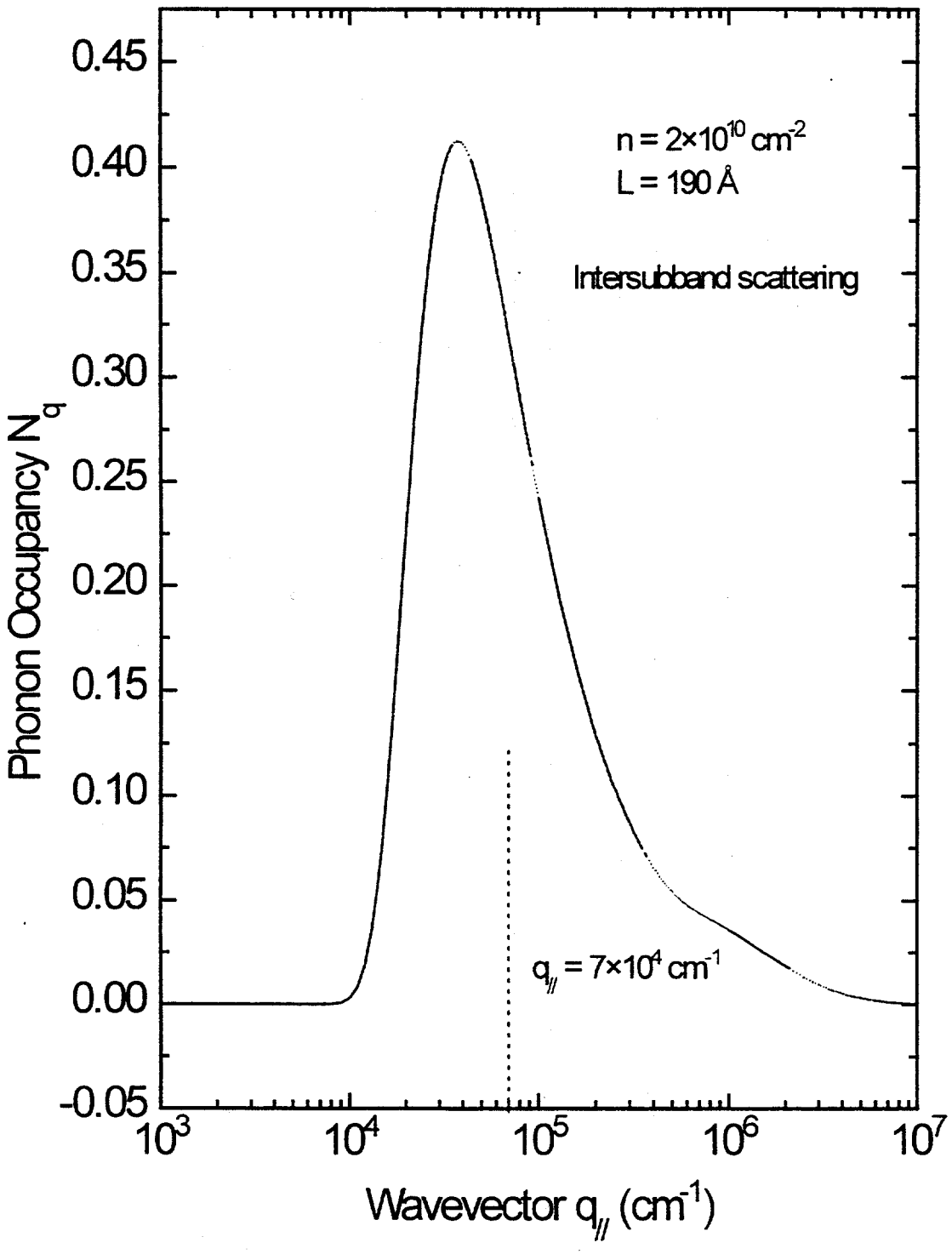
0.45
0.40
0.35
0.30
0.25
0.20
0.15
0.10
0.05
0.00
-0.05
Phonon Occupancy N_q
$n = 2\times10^{10}$ cm^{-2}
L = 190 Å
Intersubband scattering
$q_{//} = 7\times10^4$ cm^{-1}
10^3
10^4
10^5
10^6
10^7
Wavevector $q_{//}$ (cm^{-1})

Figure 2 - 9

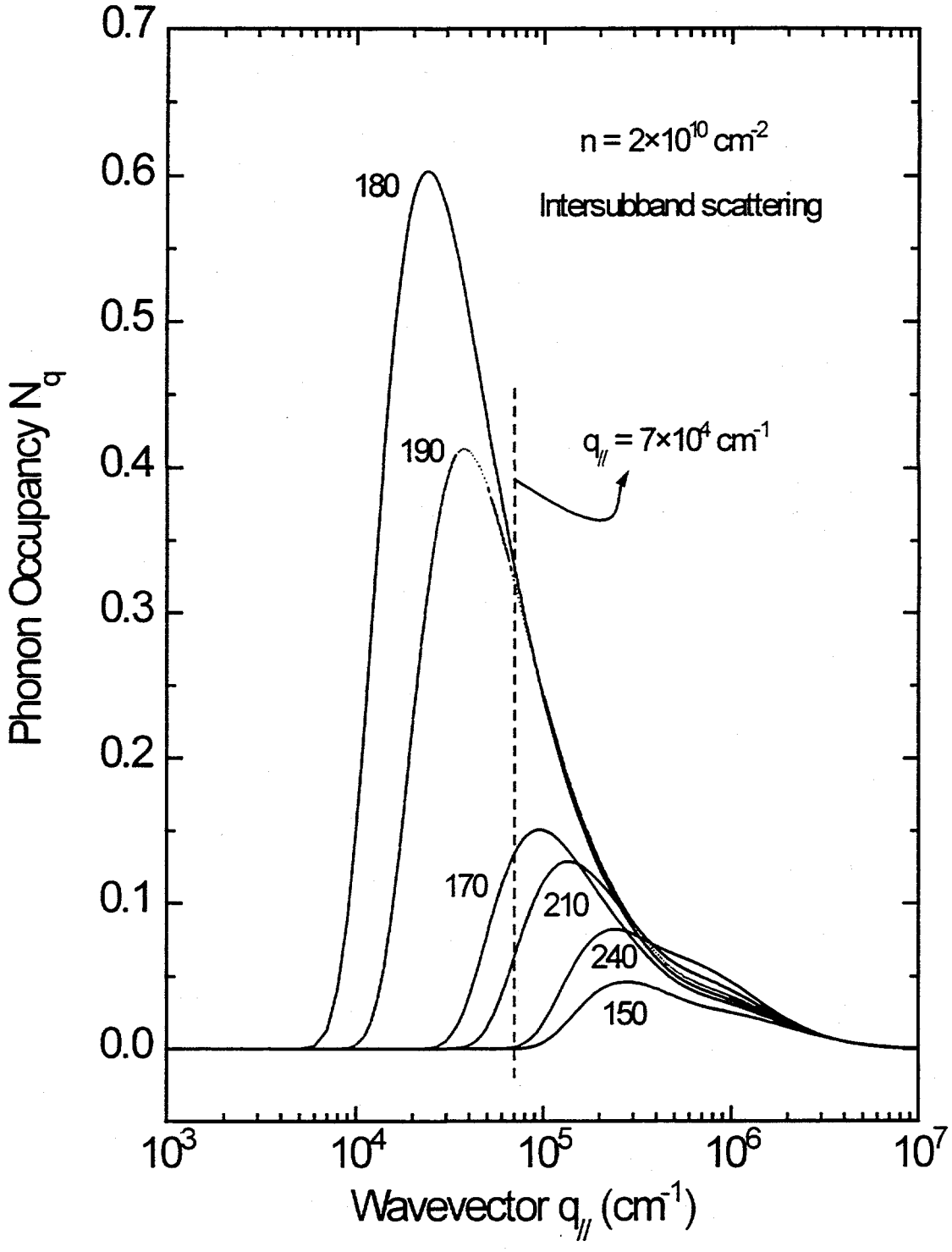
0.7
0.6
0.5
0.4
0.3
0.2
0.1
0.0
Phonon Occupancy N_q
$n = 2\times10^{10}$ cm^{-2}
Intersubband scattering
180
190
170
210
240
150
$q_{//} = 7\times10^4$ cm^{-1}
10^3
10^4
10^5
10^6
10^7
Wavevector $q_{//}$ (cm^{-1})

Figure 2 - 10

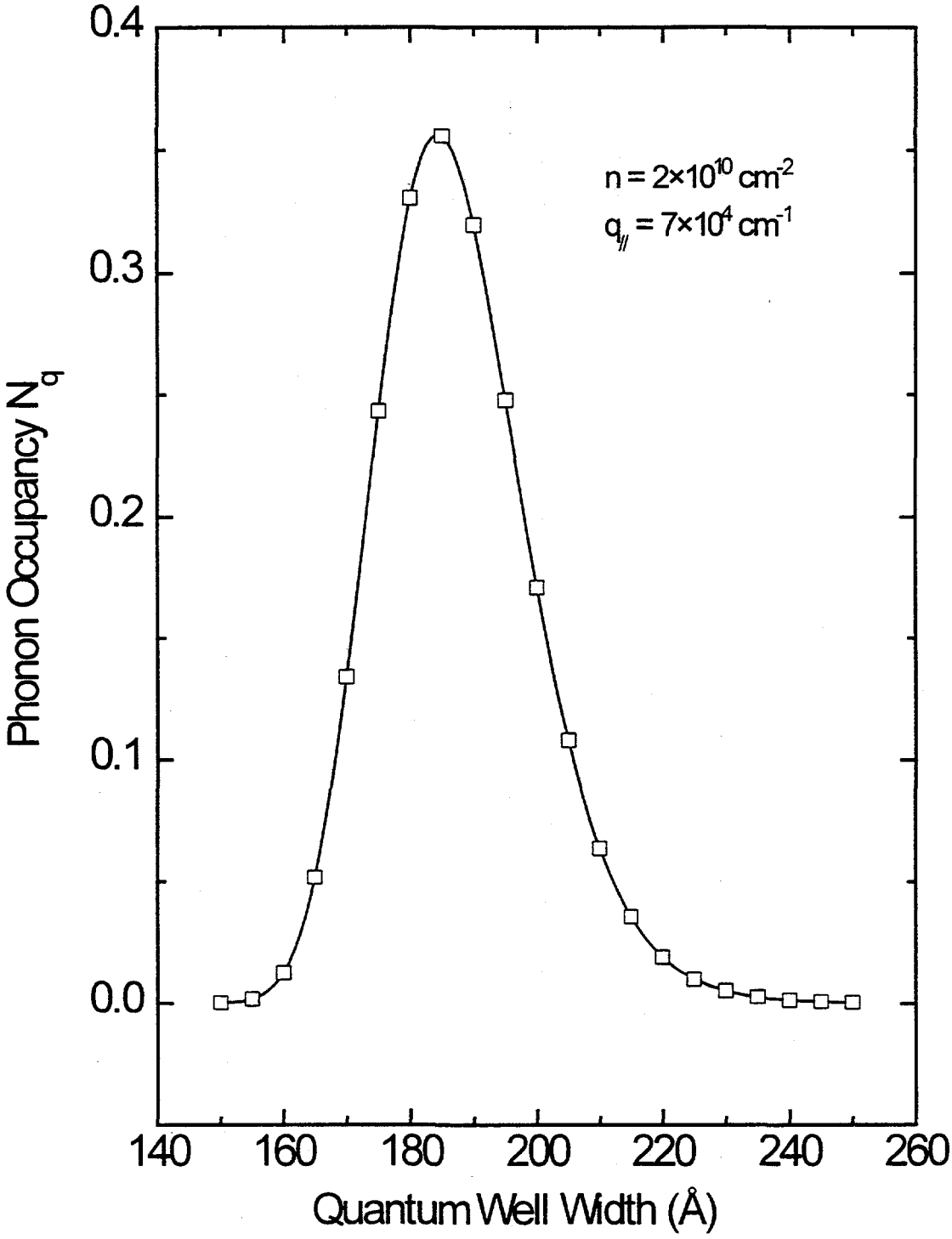
0.4
0.3
0.2
0.1
0.0
Phonon Occupancy N_q
$n = 2\times10^{10}$ cm^{-2}
$q_{//} = 7\times10^{4}$ cm^{-1}
140
160
180
200
220
240
260
Quantum Well Width (Å)

Figure 2 - 11

Chapter III: Resonant Intersubband Scattering of Optical Phonons in GaAs/AlAs Quantum Wells - Experiments

In this chapter we present our experimental investigation of the phenomenon of resonant intersubband scattering of optical phonons (RISOP) in GaAs/AlAs quantum wells (QWs). This study involves a time-resolved Raman scattering of non-equilibrium optical phonons (NOP) generated by electron relaxation in QWs. As we have shown in our model calculations in Chapter II, RISOP will generate a significant amount of small wavevector NOP which, in principle, should be easily accessible by Raman scattering. However, there exists the long standing problem of finding the correct way to measure NOP occupancy. As noted by other researchers [1], resonant Raman effects in QWs and superlattices (SLs) make it virtually impossible to determine NOP occupancy using the conventional technique that has enjoyed great success in studying NOP in bulk materials [2, 3, 4]. Here we will address this critical issue of how to determine NOP occupancy in QWs and SLs. This chapter is organized as follows. We first describe our experimental setup for performing picosecond time-resolved Raman scattering. We then move on to discuss the relation between Stokes and anti-Stokes cross section, an essential part of this experiment, and establish the correct method for measuring NOP in QWs. After testing the validity of our technique, we apply it to determine the occupancy of NOP generated by RISOP in QWs. Finally we compare and discuss the experimental results and theoretical prediction.

3.1 Experimental setup

Since LO phonons in GaAs/AlAs QWs typically have a lifetime of the order of a few picoseconds, in order to study any dynamic phenomenon related to phonons, picosecond or sub-picosecond time resolution is desirable. Fig. 3-1 shows the experimental setup. An actively modelocked Ar^+ ion laser from Spectra Physics produces 514.5 nm photon pulses with a pulse width of 200 picoseconds and a repetition rate of about 80 MHz. We use it to pump synchronously a home-build dye laser by matching the cavity lengths of the Ar^+ laser and the dye laser. Typical output from the dye laser is of the order of 100 mW (or 1 nJ per pulse) and pulse width is about 5 picosecond. Rhodamine 6G is used as the active lasing media, and this enables us to tune the laser wavelength from about 550 nm to 630 nm to study the resonant Raman effect. A beam splitter is used to send a small fraction of the dye laser output into an autocorrelator to monitor the laser operation and to measure the pulse width. The remaining output is sent through a series of Brewster-angle prisms to filter out the spontaneously emitted dye fluorescence which would otherwise overwhelm the weak Raman signal. It is then directed to the sample at an angle of about 45°. Due to the large index of refraction of GaAs ($n \sim 3.5$), the beam direction inside the sample is about 80°, this gives us a scattering geometry very close to backscattering. Both emission and scattered light are collected by a camera lens and dispersed with a SPEX 1877D Triplemate spectrometer. Photoluminescence signal is detected with a cooled GaAs photomultiplier tube using standard photon counting electronics. Raman signal on the other hand is detected with a ITT Mepsicron, a multichannel detector, coupled to a position computer.

We have performed measurements on several GaAs/AlAs multiple QW samples grown by molecular beam epitaxy (MBE) on [100] substrates. Each sample consists of about 30 QWs with identical well and barrier width. Fig. 3-2 shows schematically the QW structure. Samples were attached to the cold finger of a liquid nitrogen dewar. Experiments were carried out either at room temperature or at liquid nitrogen temperature. The excitation density was estimated both from the absorption coefficient and the laser spot size on the sample, and from analyzing the photoluminescence lineshape as described in Chapter IV. QW widths are important parameters in this experiment, they are obtained by analyzing the photoluminescence spectra also described in Chapter IV.

3.2 Relation between Stoke and anti-Stokes Raman cross sections

The conventional way to determine the phonon occupancy N_q is to measure the Stokes and anti-Stokes intensities at the same laser photon frequency. The intensity $I(\omega)$ of the Raman peak can be related to phonon occupancy N_q and the scattering cross section $\sigma(\omega)$ in the following way:

$$I_S(\omega) \propto (N_q + 1) \cdot \sigma_s(\omega) \tag{3-1}$$

$$I_{AS}(\omega) \propto N_q \cdot \sigma_{As}(\omega) \tag{3-2}$$

where S and AS denote Stokes and anti-Stokes respectively. If one assumes that the scattering cross section does not change dramatically with different photon frequencies,

which is found to be true for bulk GaAs away from the critical points, then N_q can easily be obtained from Eq. (3-1) and (3-2):

$$N_q = \frac{1}{I_S / I_{AS} - 1} \tag{3-3}$$

The above equation has been used successful in determining phonon occupation number in bulk semiconductors [2, 4]. However in semiconductor QWs, there are many subbands. Whenever the incident or the scattered photon energy is close to one of the subbands, one expects to see strong resonant Raman effect [5], the former one is referred to as the incoming resonance while the latter is called the outgoing resonance. Although the resonant Raman effect greatly enhances the signal, it also creates problems in determining N_q. Since the Stokes and the anti-Stokes resonances happen at different photon energies, σ_S and σ_{AS} cannot be assumed to be equal, therefore Eq. (3-3) will give different values of N_q for different incident photon energies. The value of N_q obtained in this way is not physically meaningful.

However, Loudon pointed out many years ago that in a system with time reversal symmetry, the Stokes cross section $\sigma_S(\omega)$ and the anti-Stokes cross section $\sigma_{AS}(\omega)$ satisfies the following equation [6]:

$$\sigma_S(\omega) = \sigma_{AS}(\omega - \omega_q) \tag{3-4}$$

where ω_q is the phonon frequency. The rigorous proof of the above relation using quantum mechanics can be found in reference [6]. Here we would like to present a more intuitive picture. Fig. 3-3(a) show the Stokes scattering process in which a incident

photon with frequency ω loses part of its energy to create a phonon with frequency ω_q, and is scattered off with frequency $\omega - \omega_q$. The time reversal process of this scattering event is shown in Fig. 3-3(b) in which an incident photon with frequency $\omega - \omega_q$ gains some energy by annihilating a phonon of frequency ω_q, and comes out of this scattering with frequency ω. Note that this process is exactly the anti-Stokes process for an incident photon with frequency $\omega - \omega_q$. When time reversal symmetry holds, we should have the relation given by Eq. (3-4).

After we take into account the relationship between Stokes and anti-Stokes cross sections, Eq. (3-3), is modified to become

$$N_q = \frac{1}{I_S(\omega)/I_{AS}(\omega-\omega_q)-1} \tag{3-5}$$

In the following section, we will test this relationship in GaAs/AlAs quantum wells.

3.3 Experimental verification of the relationship between Stokes and anti-Stokes cross sections

Although this important relationship has been in the literature for a long time, there has been few tests of it. In a recent paper [7], Ruf *et al.* measured the resonant Raman profile of a GaAs/AlAs QW sample at room temperature. They found that only by taking into account Eq. (3-4), could they get the right value for the thermal phonon occupancy. Here we will show that Eq. (3-4) can be used not only to determine the

thermal phonon occupancy, but also be used to determine NOP occupancy in quantum wells.

A typical Raman spectrum we obtained with the multi-channel detector system is shown in Fig. 3-4. We have combined two spectra of the Stokes and the anti-Stokes scattering. Laser photon is supposed to be at zero Raman shift. Confined GaAs LO phonon peak has a Raman shift of about 290 cm^{-1} and a width about 6 cm^{-1}. The AlAs phonon peak is also visible around 400 cm^{-1} on the Stokes side. By varying the laser photon energy, we obtained a serious of spectra similar to the one shown in Fig. 3-4, and by plotting the phonon peak intensity versus the incident laser photon energy, we obtained the resonant Raman profile of the sample.

Fig. 3-5 shows the room temperature resonant Raman profile of a 165 Å GaAs/AlAs QW sample. It can be seen that when the laser photon energy is tuned from 1.95 eV to 2.20 eV, both the Stokes and the anti-Stokes intensities change dramatically, showing strong resonant effect. The prominent resonant Raman peak corresponds to the transition between the sixth electron and heavy subbands, while the transition between the seventh subbands is responsible for the maximum in the anti-Stokes intensity around 2.17 eV. Clearly if we were to calculate phonon occupancy simply by Eq. (3-3), we would get a thermal phonon occupancy that depends strongly on the laser photon energy. However, taking a closer look we find that the resonant profile of the Stokes and anti-Stokes scattering have very similar line shapes, with the Stokes profile shifted to the high energy side by exactly one LO phonon energy of 36.5 meV relative the anti-Stokes profile. This verifies Eq. (3-4). If we shift the two profiles relative to each other by 36.5 meV and multiply the anti-Stokes intensity by a factor of 3.7, we find that we can lay the

two resonant profiles right on top of each other (Fig. 3-6). Using Eq. (3-5), we obtain a phonon occupancy of 0.37. This is quite close to the thermal phonon occupancy of 0.3 calculated from the room temperature. In order to make a more straightforward comparison, we convert the phonon occupancy into the corresponding phonon temperature. Since phonons are bosons, they follow Bose-Einstein statistics. Therefore by using the following equation,

$$N_q = \frac{1}{\exp(E_{LO} / K_B T) - 1} \tag{3-6}$$

where E_{LO} is the GaAs LO phonon energy and K_B is the Boltzmann constant and T is the temperature, we find a phonon temperature of 335 K. This is very close to the room temperature of 300K. The slight increase in phonon temperature may be attributed to laser heating of the sample.

Having successfully obtained thermal phonon occupancy by taking into account the resonant Raman effect, we want to apply this technique to study NOP in QWs. In this study, we cooled our sample to liquid nitrogen temperature (T=77K). Since at 77K, thermal phonon occupancy calculated from Eq. (3-6) is only 0.003, which may be neglected when compared to the NOP occupancy excited by picosecond laser pulses as we will show in the following paragraphs. In the actual experiments, we also need to consider possible contribution to NOP due to laser heating and non-ideal thermal contact between sample and liquid nitrogen in our simple cryogenic system. These factors can cause the sample surface temperature to be higher than 77K. Thus the thermally excited phonon occupancy needs to be subtracted from our measured phonon occupancy.

Fig. 3-7 shows the resonant Raman profile of a 195 Å QW sample at liquid nitrogen temperature. Prominent peaks in the resonant profiles corresponds to the transitions from the sixth and the seventh heavy hole subbands to the corresponding electron subbands. Again we find that the Stokes and anti-Stokes profiles of the NOP are shifted from each other by the LO phonon energy in a way similar to that of the thermal phonons. Using Eq. (3-5), we find a phonon occupancy of 0.08.

To determine the contribution from thermal phonons to the measured phonon occupancy, we performed a measurement of the density dependence of the phonon occupancy. Fig. 3-8 shows the measured phonon occupancy N_q as a function of electron density excited by laser pulses. As can be seen, N_q increases monotonically with hot electron density. This is consistent with the prediction of Eq. (2-21) in Chapter II, and we expect that as hot electron density goes to zero, NOP occupancy should go to zero. However, when we extrapolate the curve in Fig. 3-8 to zero electron density, we get a non-zero N_q. This suggests that N_q as-determined is not the true value of NOP occupancy, it contains contribution from thermal phonons. The extrapolated value of N_q to zero electron density, N_0, should correspond to the thermal phonon occupancy with no laser photon hitting the sample. From $N_0 = 0.038$, we obtained a sample surface temperature of 130 K. To determine the effect of laser heating, we performed a measurement with the laser running in continuous mode but with the same amount of power as in the pulsed mode. We measured a phonon occupancy of about 0.033. This shows that laser heating is negligible in experiments done at low temperature. In the

measurement of RISOP to be described in the next section, we will subtract the value N_0 from N_q determined directly from Eq. (3-5).

3.4 Resonant intersubband scattering of optical phonons -- experiment and discussions

In the above sections, we have shown how resonant Raman effect can greatly affect the determination of the occupancy of NOP in QWs. We also demonstrated that by taking into account the critical relationship between the Stokes and anti-Stokes cross sections, one can successfully measure the NOP occupancy. In this section, we will use this technique to investigate RISOP. We have measured the NOP occupancy for a series of QW samples at liquid nitrogen temperature. The QW widths are determined from PL measurement to be described in Chapter IV, and are so chosen that they span across the predicted resonance peak at well width of about 185 Å.

Fig. 3-9 shows our experimentally measured NOP occupancy as a function of the QW width. Also shown on the same plot is the theoretical prediction from our model calculation. Surprisingly as one can see the value of NOP occupancy measured experimentally is much lower than that of the prediction. Furthermore, there seems to be only a slight increase in NOP occupancy as the width of the QW increases, and no noticeable enhancement due to RISOP can be found.

The unexpectedly large discrepancy between the prediction from our model calculation and our experimental results needs to be explained. When we look back at our model calculation in Chapter II, we see that it is based on the assumption that quasi-

momentum parallel to the QW plane is conserved during hot electron relaxation process and during light scattering. If this assumption is relaxed, we would expect deviations from the theoretical prediction. Here we will examine the possibility that resonant Raman scattering can be mediated by interface roughness in our QW samples.

In a recent paper [8] Tatham *et. al.* showed that when Raman measurement was done in narrow quantum wells at an energy far away from the resonance, no anti-Stokes scattering could be observed. This shows the important of resonant Raman effect in detecting the NOP. Now let us consider an outgoing resonant Raman scattering at some electron and hole subband edge shown schematically in Fig. 3-10. It can be shown that as a result of the conservation of energy and quasi-momentum, phonons involved in this scattering process will have a wave vector $q_{//}$ about 4×10^5 cm^{-1}. On the other hand the change of photon wave vector parallel to the QW plane in quasi-back scattering is about 7×10^4 cm^{-1}. The large mismatch of the wave vector (or momentum transfer) means that this scattering process would, in principle, be forbidden by quasi-momentum conservation. However, the experimental observation of the resonant Raman effect suggests that it does take place. Therefore wave vector conservation has to be somehow relaxed in this case. And the most likely candidates that cause the relaxation of wave vector conservation are defects or impurities.

The idea of defect mediating resonant Raman scattering has been invoked by a number of researchers to explained their experimental results [9, 10]. For example, to explain the NOP observed in their Raman experiment on narrow GaAs/AlAs quantum wells, Tsen *et. al.* have suggested that defects may play a role in the resonant Raman

scattering, thereby shifting the wave vector probed by Raman scattering from $< 10^5$ cm^{-1} to about 4×10^5 cm^{-1}. However, if we were to choose this wave vector to be the one probed in our experiment, we should measure a NOP occupancy about 3 to 4 times larger than what we have observed. This can be deduced from the NOP occupancy curves in Fig. 2-8, 2-9, 2-10. So this is not likely to be the explanation for our experiment. We believe that a more likely explanation for the relaxation of wave vector conservation in our resonant Raman experiment is the interface roughness in GaAs/AlAs quantum wells.

Recent experimental work with scanning electron microscopy (SEM) have revealed the existence of islands at the interface of GaAs and AlAs layers. Resonant acoustic phonon scattering [11] has also found interface roughness to be important. These authors have found the lateral size of the roughness to be around a few hundred Å. Due to interface roughness, $q_{//}$ may not need to be conserved exactly in Raman scattering. Instead of probing phonons with a single value of $q_{//}$, we are in fact measuring phonons within a range of $q_{//}$. This range is approximately related to the average size d of the atomically smooth regions as $2\pi/d$. Since NOP with large wavenumber ($> 10^6$ cm^{-1}) have a rather small occupancy as can be seen from Fig. 3-11(a), the inclusion of these phonon in Raman scattering will significantly reduce the measured NOP occupancy N_q. In Fig. 3-12, we show our calculations for several different values of d. As d gets smaller, more large wave vector NOP are probed by Raman scattering, and consequently we find a smaller N_q. Qualitative agreement between experiment and calculation is found for d of the order of 100 Å. Our calculation suggests that interface roughness may be responsible for the absence of RISOP effects in the NOP measured by Raman scattering experiment.

In summary, we have shown that by taking into account the relationship between the Stokes and anti-Stokes scattering cross sections, we can successfully determine the phonon occupancy in QW and SL from their Resonant Raman profiles. We have used this technique to investigate the issue of resonant intersubband scattering of optical phonons by measuring the NOP occupancy. Our experimental results differ significantly from the theoretical prediction based on model calculations. We discussed this discrepancy in terms of the breakdown of quasi-momentum conservation caused by interface roughness. Our results suggest that interface roughness play a very import role in the measurement the NOP occupancy in quantum well samples.

References

[1] See for instance, J. F. Ryan in *Hot Carriers in Semiconductor Nanostructures: Physics and Applications*, edited by J. Shah (Academic Press, Boston, 1992).

[2] C. L. Collins and P. Y. Yu, Phys. Rev. B **30**, 4501 (1984).

[3] Von der Linde, J. Kuhl, and H. Klingenberg, Phys. Rev. Lett. **44**, 1505 (1980).

[4] D. S. Kim and P. Y. Yu, Phys. Rev. B **43**, 4158 (1991).

[5] J. E. Zucker, A. Pinczuk, d. S. Chemla, A. C. Gossard and W. Wiegmann, Phys. Rev. Lett. **51**, 1293 (1983); Phys. Rev. B **29**, 7065 (1984); R. C. Miller, D. A. Kleinman and A. C. Gossard, Sol. St. Commun. 60, 213 (1986); J. Menendez, J. Lumines.**44** 285 (1989).

[6] R. Loudon, Proc. R. Soc.London A**275**, 218 (1963).

[7] T. Ruf, K. W. Wald, P. Y. Yu, K. T. Tsen, H. Morkoç, and K. T. Chan, Superlattices and Microstructures **13**, 203 (1992).

[8] M. Tatham and J. Ryan, Semicond. Sci. Technol. **7**, B102 (1992).

[9] K. T. Tsen, K. R. Wald, T. Ruf, P. Y. Yu, and H. Morkoç, Phys. Rev. Lett. **67**, 2557 (1991).

[10] T. A. Gant, M. Delaney, M. V. Klein, R. Houdre, and H. Morkoç, Phys. Rev. B **39**, 1696 (1989).

[11] T. Ruf, V. I. Belitsky, J. Spitzer, V. F. Sapega, M. Cardona, and K. Ploog, Phys. Rev. Lett. **71**, 3035 (1993).

Figure Captions for Chapter III

Fig. 3-1 A schematic diagram of the experimental setup for the time-resolved Raman measurement.

Fig. 3-2 A schematic diagram of GaAs/AlAs multiple quantum well structure.

Fig. 3-3 A schematic diagram for (a) Stokes and (b) anti-Stokes Raman scattering. Note that (b) is a time reversal process of (a).

Fig. 3-4 A typical Raman spectrum of GaAs/AlAs quantum wells obtained with our experimental setup. The GaAs and AlAs confined phonons peaks are at 290 cm^{-1} and 400 cm^{-1}, respectively.

Fig. 3-5 Resonant Raman profiles of the Stokes (solid squares) and anti-Stokes (solid circles) Raman scattering for a 165 Å GaAs/AlAs quantum well sample measured at room temperature. Dashed lines are guides to the eyes. Note that the two profiles have similar lines shapes, and that the separation between the Stokes and anti-Stokes peaks is exactly one LO phonon energy.

Fig. 3-6 Resonant Raman profiles of the same sample as in Fig.3-5. However the anti-Stokes peak has been purposely shifted towards higher energy by one LO phonon energy, and then multiplied by a factor of 3.7. Using Eq. (3-5) and (3-6), we obtained a thermal phonon temperature of 335 K, consistent with our expectation.

Fig. 3-7 Resonant Raman profiles of (a) Stokes and (b) anti-Stokes Raman scattering of a 195 Å GaAs/AlAs quantum well sample measured at liquid nitrogen temperature. Noting again that the two profiles are quite similar with the Stokes peak position being one LO phonon energy higher than that of the anti-Stokes peaks.

Fig. 3-8 Phonon occupancy as a function of the hot electron density for a 195 Å GaAs/AlAs quantum well sample at liquid nitrogen temperature. The extrapolation to the zero electron density reveals a thermal phonon occupancy which should be subtracted off.

Fig. 3-9 Non-equilibrium phonon occupancy as a function of the width of GaAs/AlAs quantum well. Solid squares are experimental results, open circles are from model calculations in Chapter II. Lines are meant to be guides to the eyes.

Fig. 3-10 A schematic diagram for the outgoing resonant Raman process at an electron subband edge.

Fig. 3-11 (a) Non-equilibrium phonon distribution calculated for a 190 Å GaAs/AlAs quantum well sample. The sharp peak is due to intersubband scattering, while the broad peak is due to intrasubband scattering. (b) An expanded view of the sharp peak in (a). Vertical dashed line indicates the wave vector probed by Raman scattering experiment.

Fig. 3-12 Non-equilibrium phonon occupancy as a function of the width of GaAs/AlAs quantum well calculated for various interface roughness, d is the size of the island. Also shown are the experimental data (solid squares).

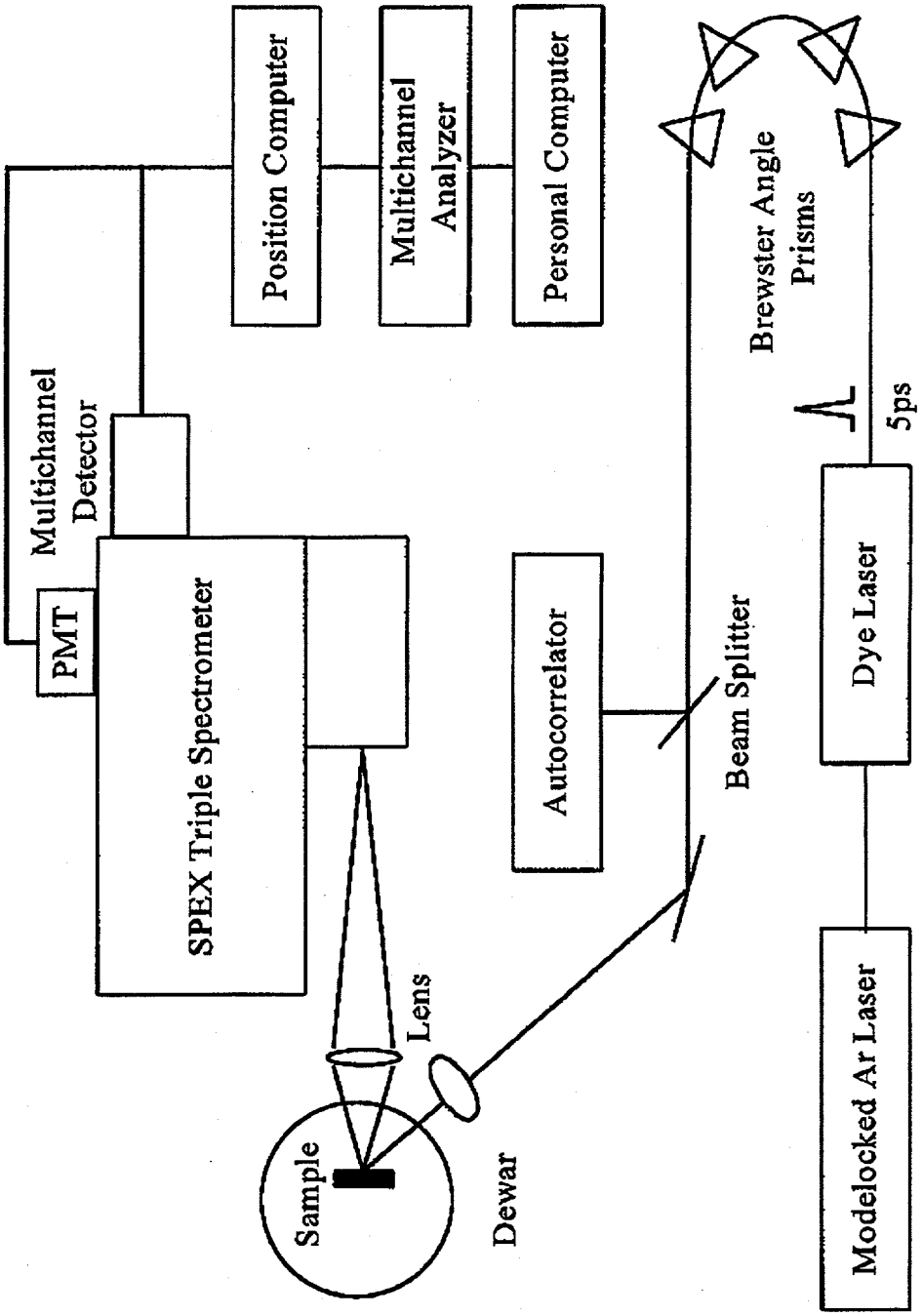
Position Computer
Multichannel Analyzer
Personal Computer
Multichannel Detector
PMT
SPEX Triple Spectrometer
Lens
Sample
Dewar
Autocorrelator
Beam Splitter
Brewster Angle Prisms
Dye Laser
5ps
Modelocked Ar Laser

Figure 3 – 2

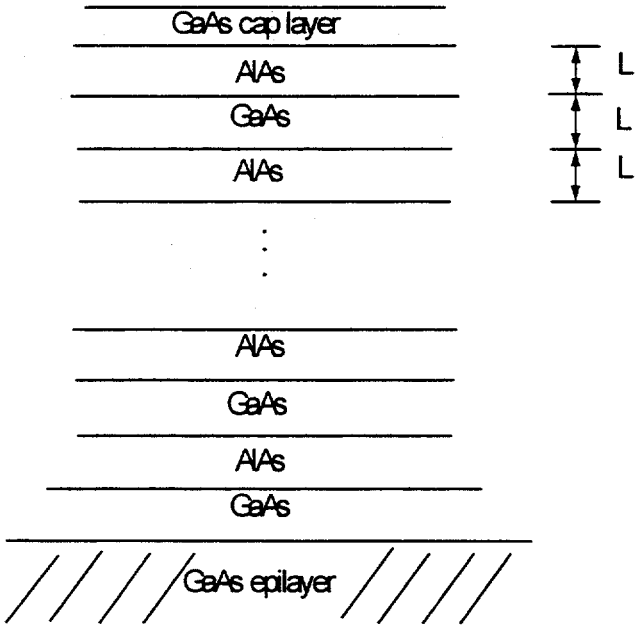
GaAs cap layer
AlAs
GaAs
AlAs
L
L
L
AlAs
GaAs
AlAs
GaAs
GaAs epilayer

Figure 3 - 2

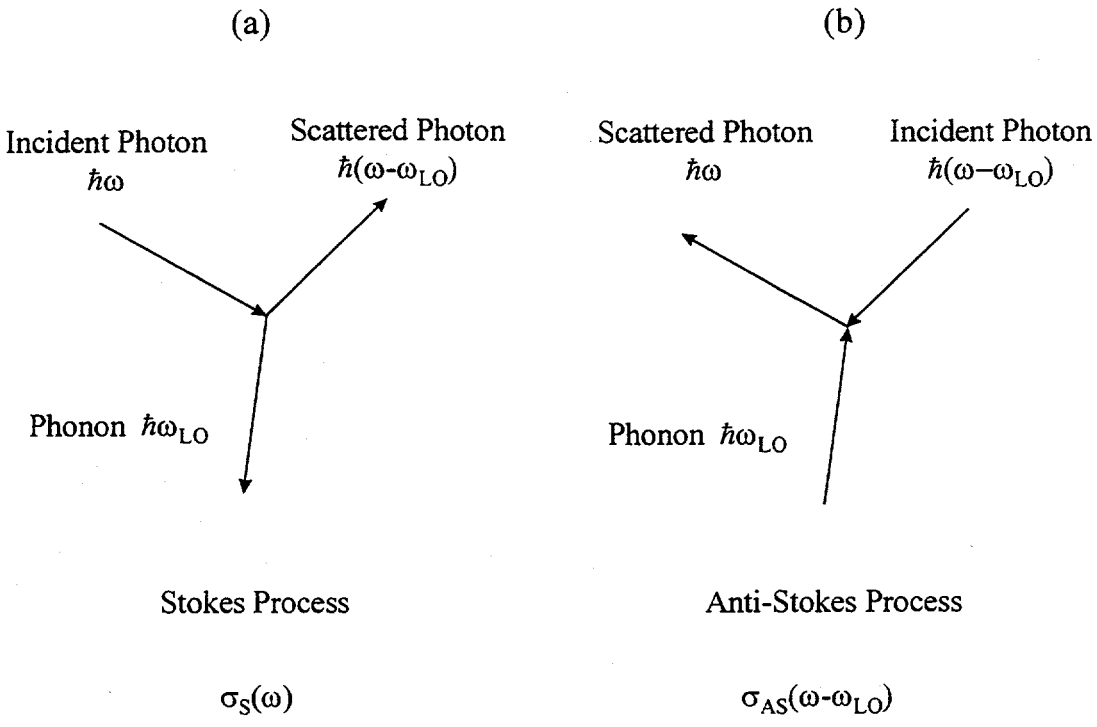
(a)
(b)
Incident Photon
$\hbar\omega$
Scattered Photon
$\hbar(\omega-\omega_{LO})$
Phonon $\hbar\omega_{LO}$
Scattered Photon
$\hbar\omega$
Incident Photon
$\hbar(\omega-\omega_{LO})$
Phonon $\hbar\omega_{LO}$
Stokes Process
Anti-Stokes Process
$\sigma_S(\omega)$
$\sigma_{AS}(\omega-\omega_{LO})$

Figure 3 - 3

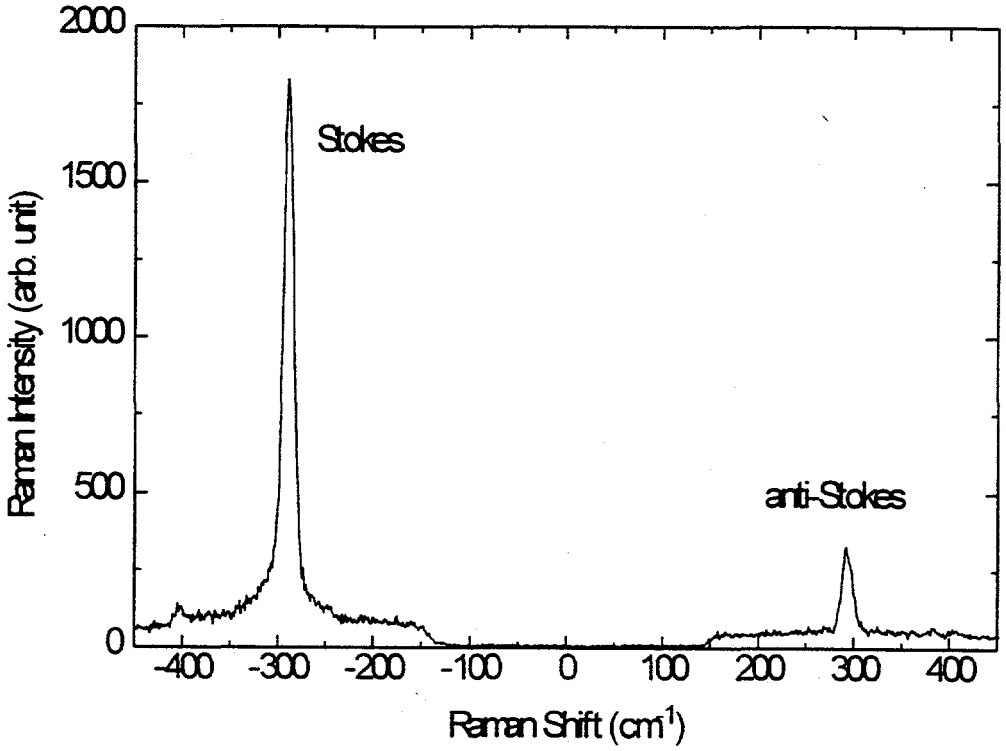
2000
1500
1000
500
0
Raman Intensity (arb. unit)
Stokes
anti-Stokes
-400
-300
-200
-100
0
100
200
300
400
Raman Shift (cm-1)

Figure 3 - 4

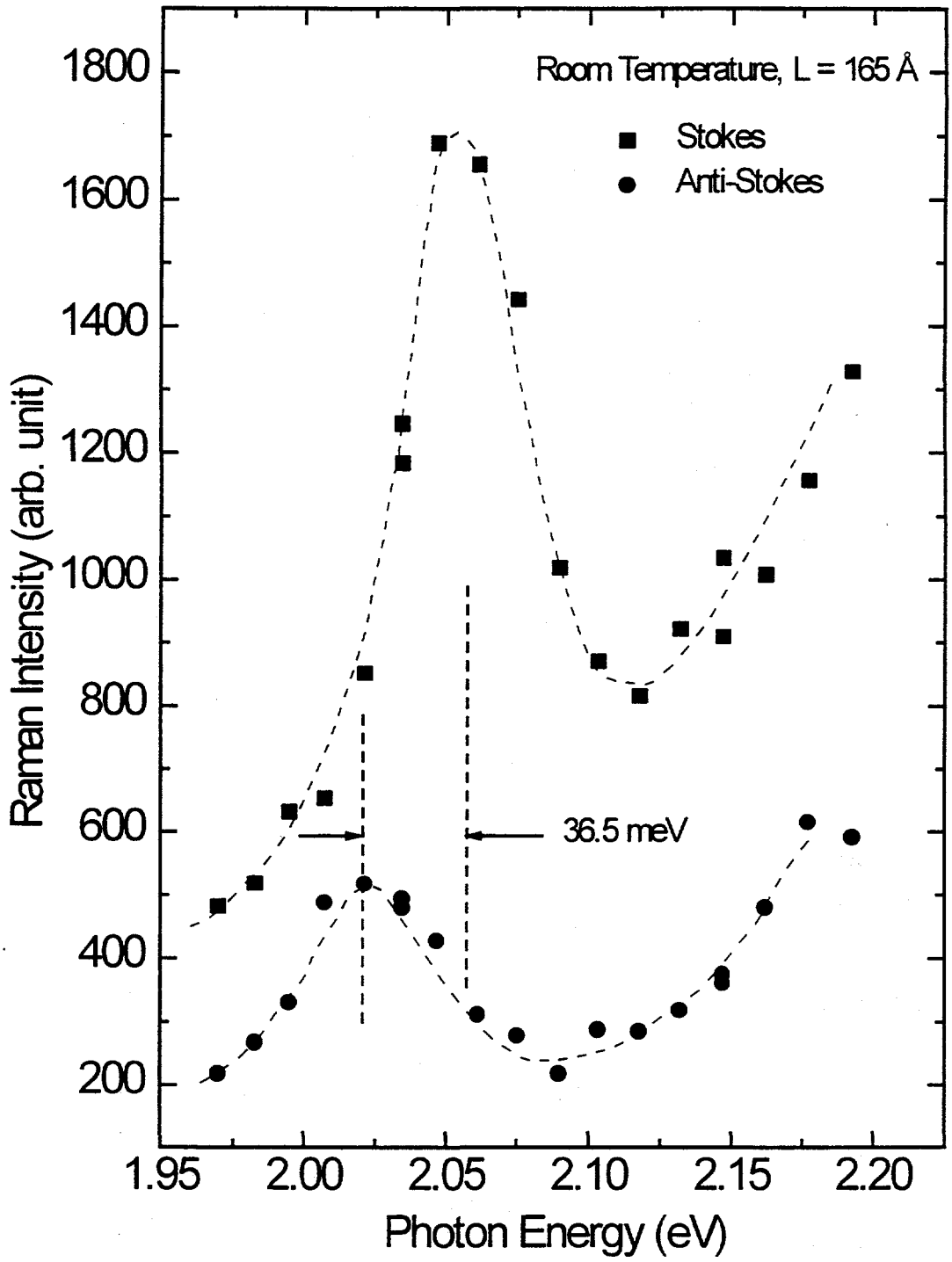
Room Temperature, L = 165 Å
Stokes
Anti-Stokes
36.5 meV
Raman Intensity (arb. unit)
Photon Energy (eV)
1800
1600
1400
1200
1000
800
600
400
200
1.95
2.00
2.05
2.10
2.15
2.20

Figure 3 - 5

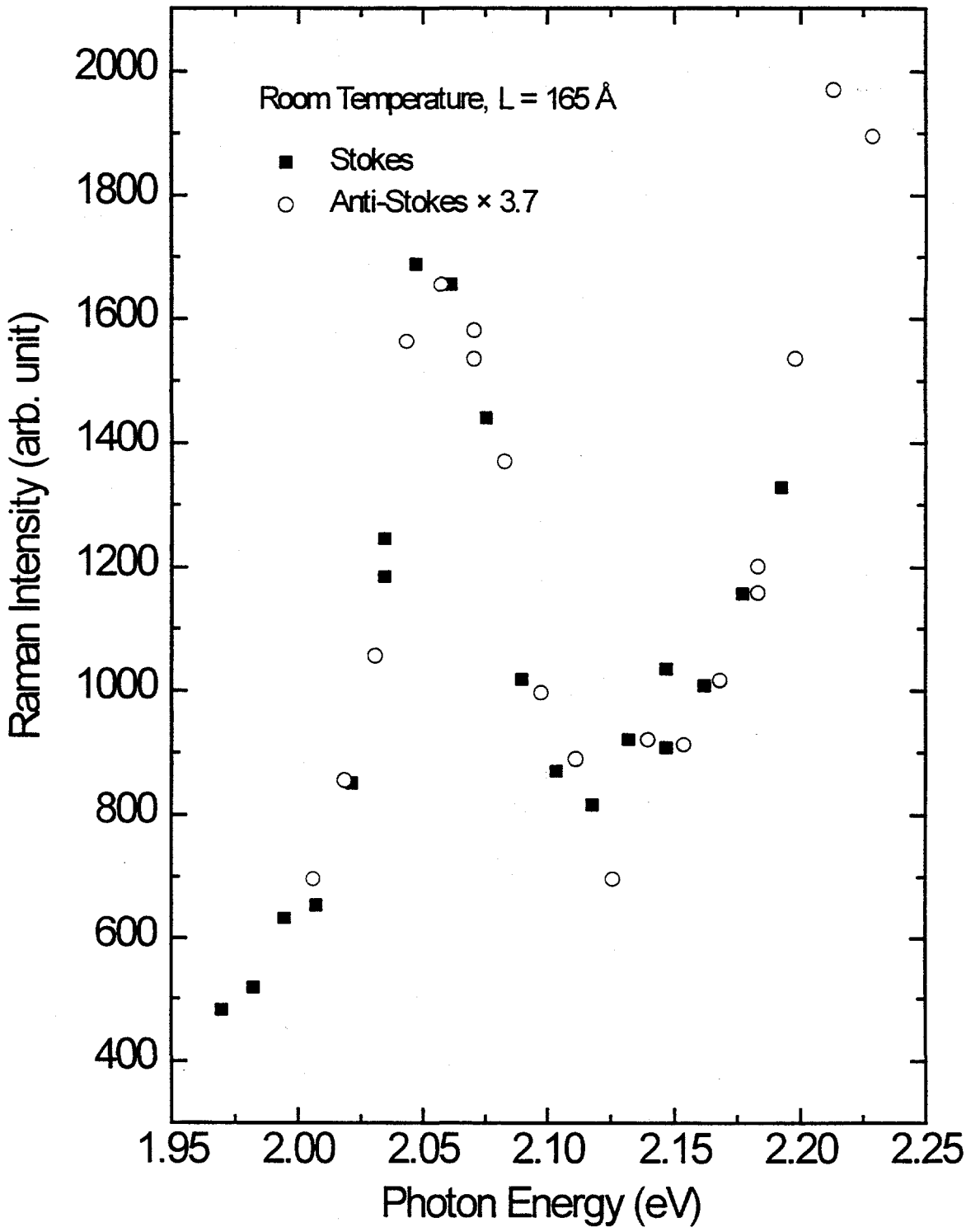
Room Temperature, L = 165 Å
Stokes
Anti-Stokes × 3.7
Raman Intensity (arb. unit)
2000
1800
1600
1400
1200
1000
800
600
400
1.95
2.00
2.05
2.10
2.15
2.20
2.25
Photon Energy (eV)

Figure 3 - 6

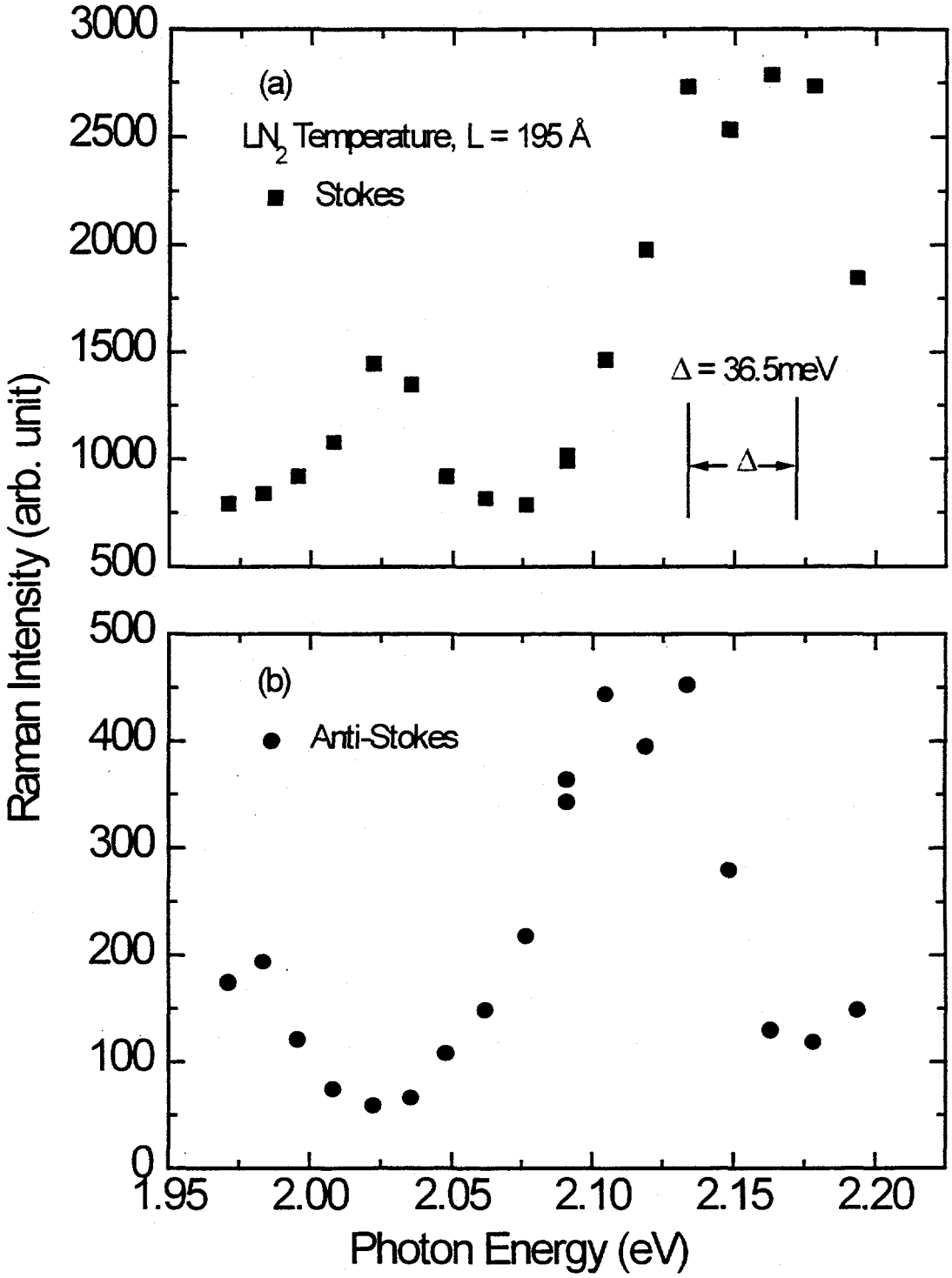
(a)
LN2 Temperature, L = 195 Å
Stokes
Δ = 36.5meV
Δ
(b)
Anti-Stokes
Raman Intensity (arb. unit)
Photon Energy (eV)
3000
2500
2000
1500
1000
500
500
400
300
200
100
0
1.95
2.00
2.05
2.10
2.15
2.20

Figure 3 - 7

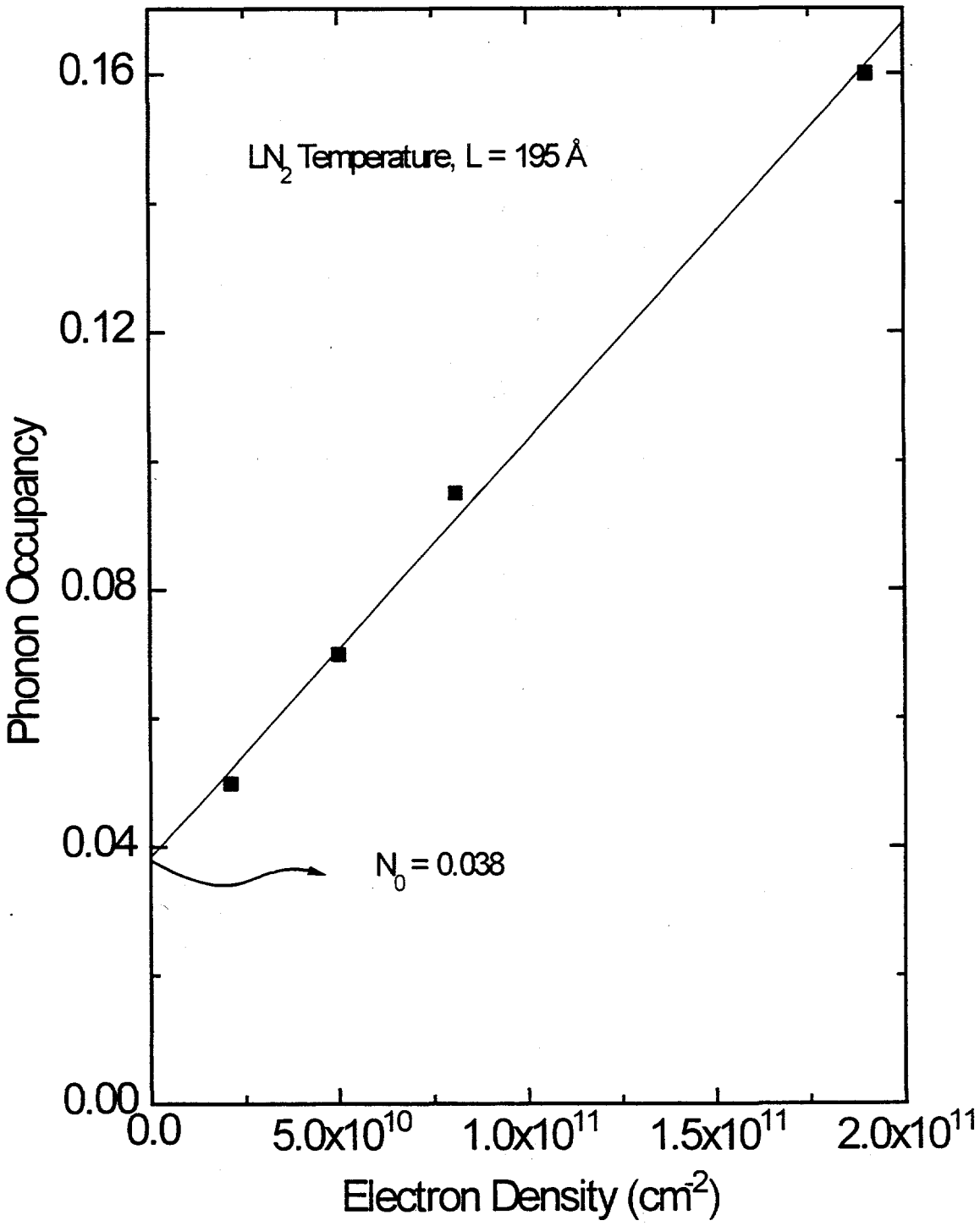
0.16
0.12
0.08
0.04
0.00
Phonon Occupancy
LN2 Temperature, L = 195 Å
N0 = 0.038
0.0
5.0x10^10
1.0x10^11
1.5x10^11
2.0x10^11
Electron Density (cm^-2)

Figure 3 - 8

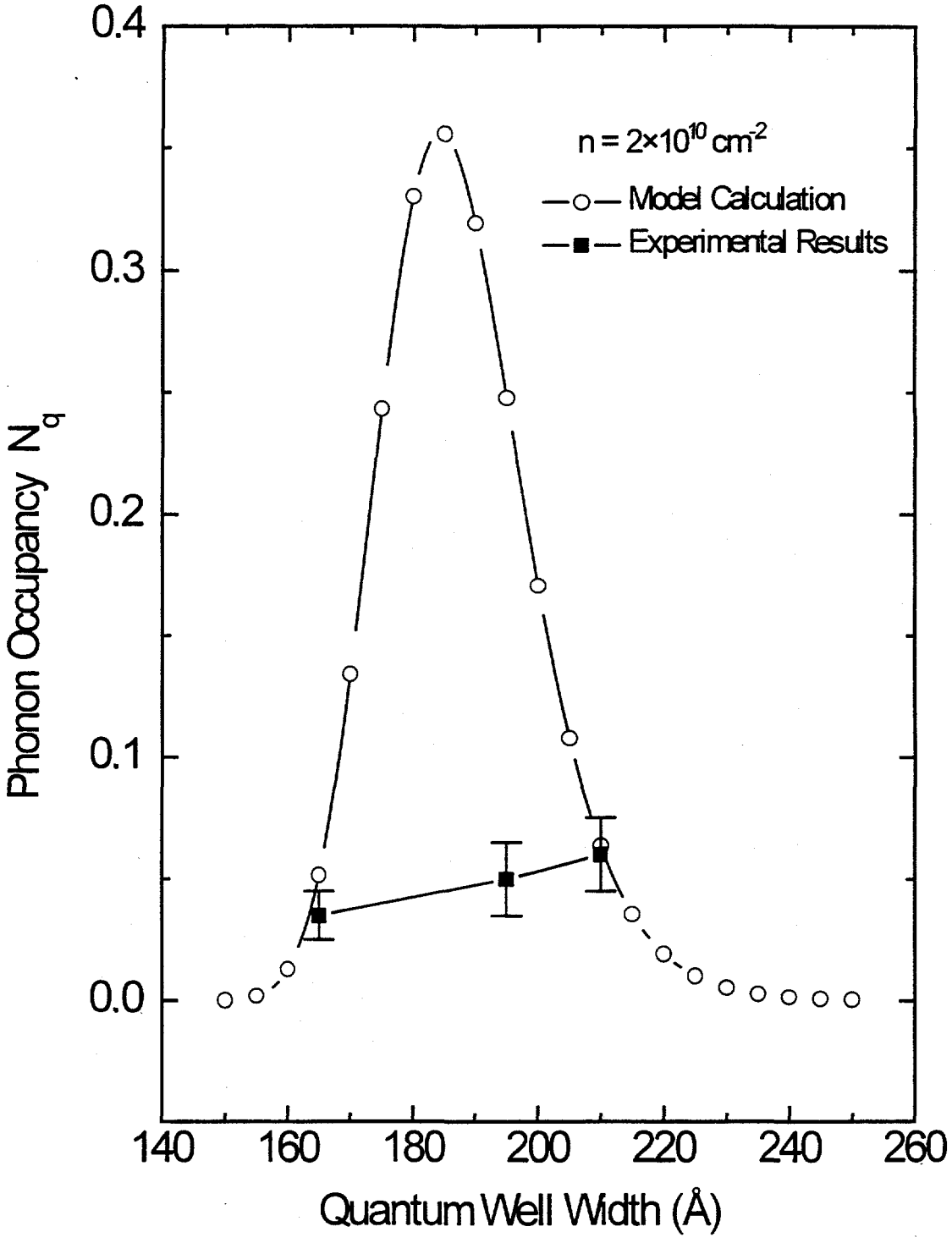
0.4
0.3
0.2
0.1
0.0
Phonon Occupancy N_q
$n = 2\times10^{10}\ cm^{-2}$
Model Calculation
Experimental Results
140
160
180
200
220
240
260
Quantum Well Width (Å)

Figure 3 - 9

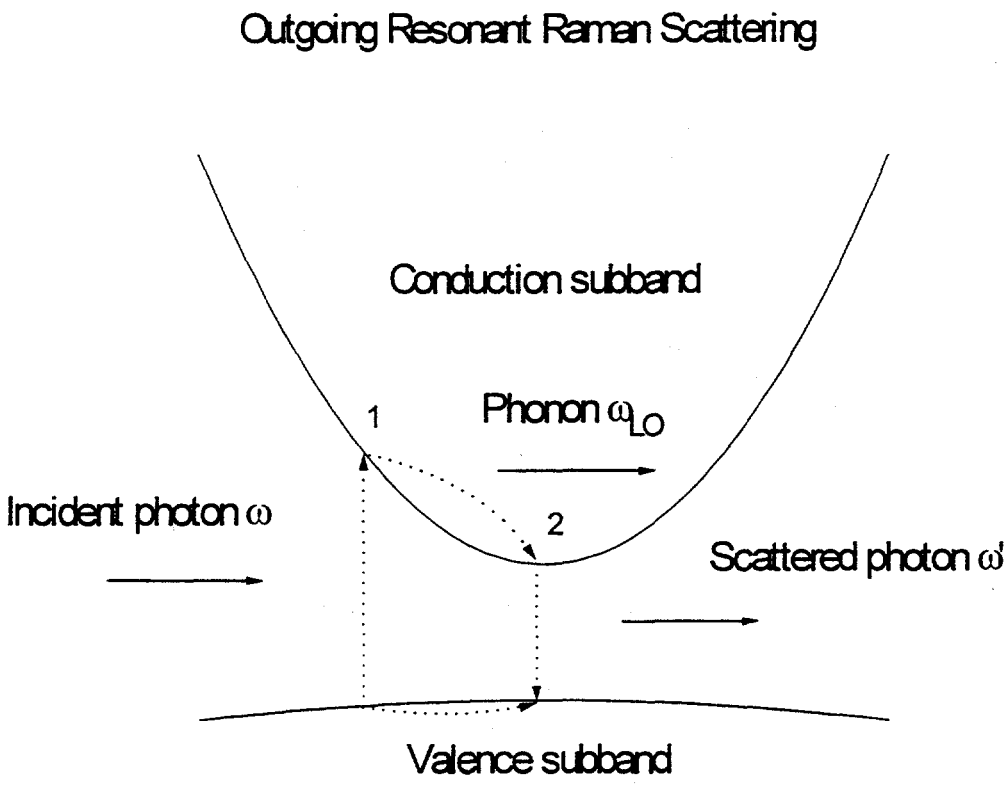
Outgoing Resonant Raman Scattering
Conduction subband
1
Phonon ω_{LO}
Incident photon ω
2
Scattered photon ω'
Valence subband

Figure 3 - 10

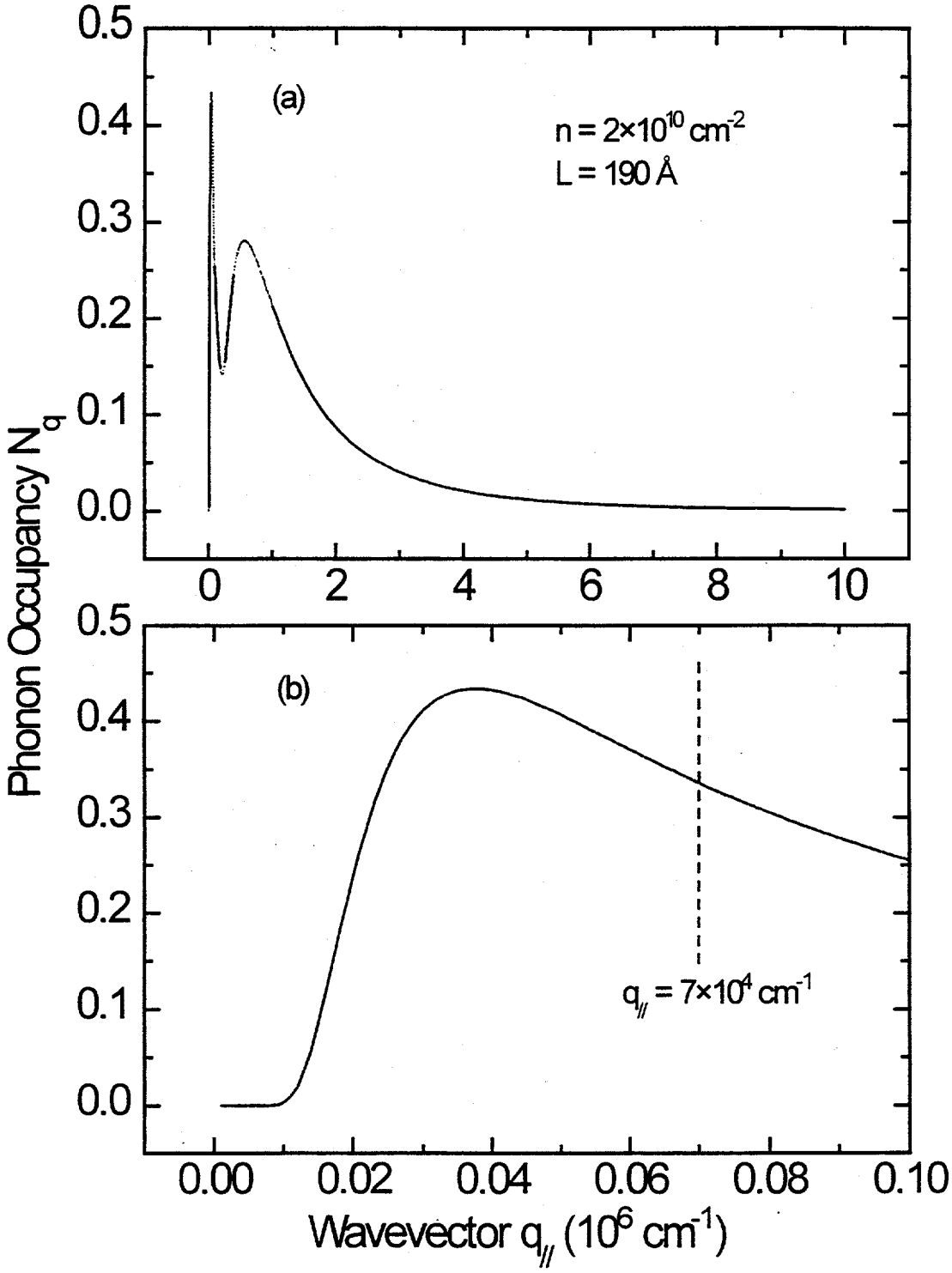
(a)
n = 2×10^10 cm^-2
L = 190 Å
(b)
q// = 7×10^4 cm^-1
Phonon Occupancy N_q
Wavevector q// (10^6 cm^-1)
0.0
0.1
0.2
0.3
0.4
0.5
0
2
4
6
8
10
0.00
0.02
0.04
0.06
0.08
0.10

Figure 3 - 11

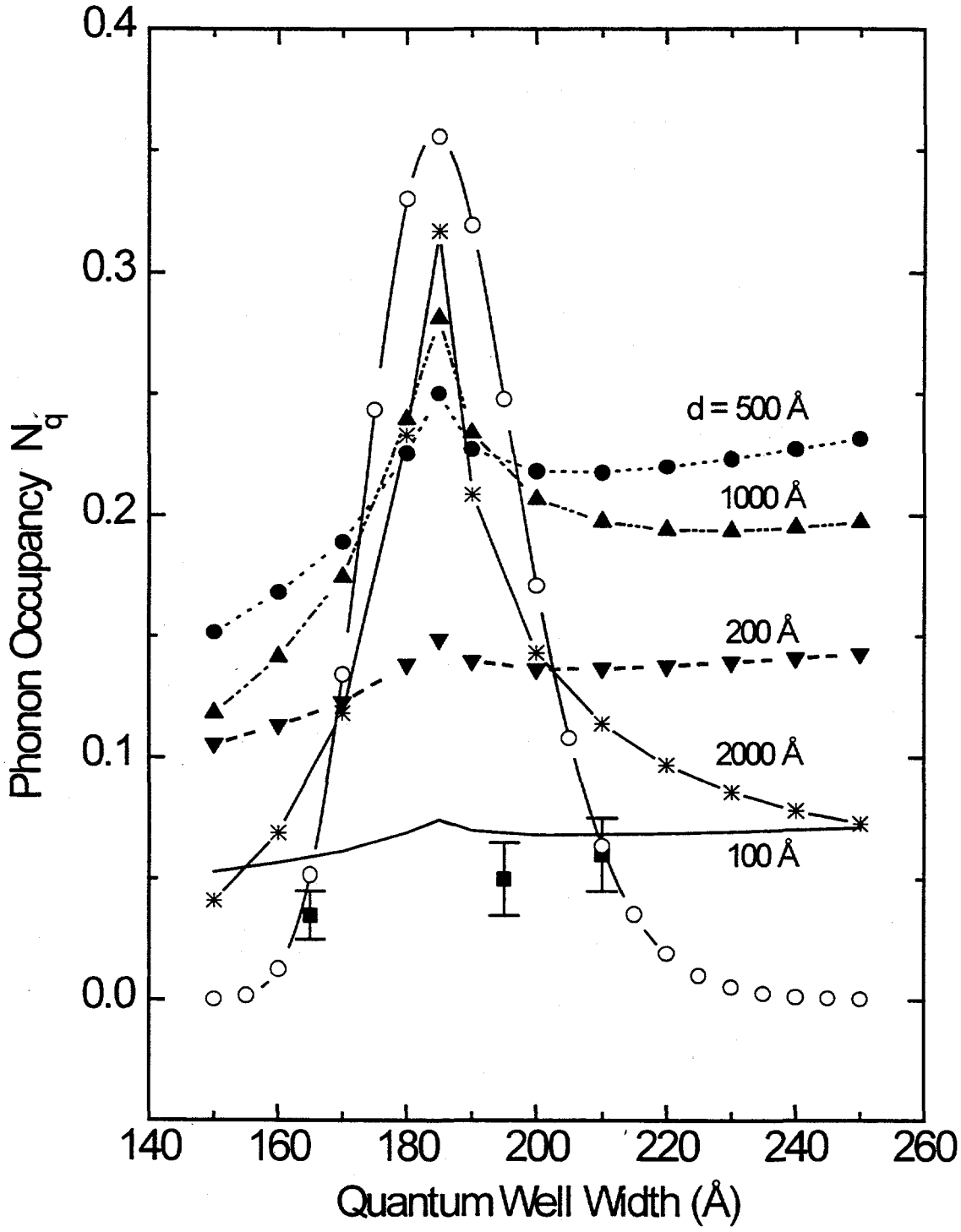
0.4
0.3
0.2
0.1
0.0
Phonon Occupancy N_q
d = 500 Å
1000 Å
200 Å
2000 Å
100 Å
140
160
180
200
220
240
260
Quantum Well Width (Å)

Figure 3 - 12

Chapter IV: Photoluminescence of Highly Excited GaAs/AlAs Quantum Wells

In this chapter we will examine the emission spectra from GaAs/AlAs quantum wells under intense picosecond laser excitation. Photoluminescence (PL) is a process where electrons are excited by photons into the conduction (sub)bands, after relaxing down to the bottom of the (sub)band, these electrons recombine with the photoexcited holes to produce photons. Under high intensity excitation, excitons (electron-hole pairs) will be ionized when the density is on the order of 10^{11} cm^{-2}, resulting in the formation of a dense two-dimensional electron-hole plasma (EHP). At these high electron densities the interaction among electrons becomes very important. Many-body interactions among electrons lead to many interesting phenomena like band gap renormalization (BGR) [1] which have been extensively studied with the PL technique. Also as electron density increases, the electron Fermi level rises and may cross higher subband levels, this is known as band filling. As high index subbands get populated, emission from these subbands appears in the PL spectra. In the following sections we will make use of the band filling features in the PL spectra from highly excited GaAs/AlAs quantum wells to deduce the width of the wells. In addition, through a lineshape fitting of the PL spectra, we can deduce the average electron density. Both the quantum well width and the electron density are important parameters for the experiment described in Chapter III. Another important thing to note is that in our experiment we have observed emission from subbands a few hundred meV above the bottom of the band. At this energy level,

band non-parabolicity is expected to be important. Therefore we are able to examine the effect of band nonparabolicity on the confined electron energy levels.

4.1 Time-integrated photoluminescence from GaAs/AlAs quantum wells under high intensity excitation

Experiments described in this section were carried out using the setup shown in Fig.1 of Chapter III. GaAs/AlAs multiple quantum well samples were held either at room temperature or liquid nitrogen temperature in an optical cryostat. The output of a picosecond dye laser was tightly focused onto the sample. Excitation intensity was changed by a variable neutral density filter. A photomultiplier tube together with the conventional photon counting electronics is used to acquire the time-integrated emission spectra.

Fig. 4-1 shows the room temperature PL spectra of a 210 Å GaAs/AlAs quantum well for several electron densities. The determination of the electron densities from analysis of the PL line shapes will be described in the next section. As we can see that at electron density 4×10^{11} cm^{-2} only two peaks are present, with the first peak dominating over the second one. When the density is increased, the relative strength of these two peaks changes, and the second one eventually becomes the dominant one. This is mostly due to the staircase type of density of state of the two-dimensional electrons in quantum wells. Upon further increasing the electron density, a third higher energy peak gradually gains strength, and when $n = 6.1\times10^{12}$ cm^{-2}, we observe as many as five peaks in the PL spectrum. This is an indication of strong band filling effects as higher subbands become

populated. The width of the spectra is mainly determined by the Fermi energy of the electrons, which in turn is determined by the electron density.

Another prominent feature in Fig. 4-1 is that with increasing electron density, the low energy edge of the spectrum moves toward lower energy by about 20 meV, showing the effect of BGR. However one notices that the positions of the PL peaks for different electron densities remain essentially unchanged. This is consistent with earlier PL studies of different highly excited quantum well structures reported in the literature [2,3]. Due to BGR, one would expect to see a PL peak at the reduced band gap. However *Cingolani et. al.* have shown in a spatially resolved PL experiment that this phenomenon is due to the spectral superposition of different radiative recombination processes originating from different lateral regions of the sample where actual carrier densities differ strongly [4]. So even though many body interaction greatly affects the high intensity PL spectra, we can still safely regard the PL peak position as the exciton transition energy.

Fig. 4-2 shows the time-integrated PL spectra of a 165 Å GaAs/AlAs quantum well. One can see that the effects of BGR and band filling are quite similar to those in the 210 Å quantum well sample although the PL peak positions are quite different. The maximum width of the spectrum, determined by the electron density and limited by our laser power, are also similar (about 250 meV) in these two cases. PL spectra measured at low temperature also display pronounced band filling and BGR effects. A typical PL spectrum under high intensity excitation at liquid nitrogen temperature is shown in Fig. 4-3 for (a) a 210 Å, (b) a 165 Å GaAs/AlAs quantum well. Compared with the room temperature PL spectra, peak intensity increases by several order of magnitude, and peak

width also becomes much smaller. This is likely due to enhancement of exciton formation at low temperature [5].

4.2 Determination of the electron density in quantum well from its PL spectrum

In this section we will deduce the average electron density through a lineshape fitting of the PL spectra. Considering the recombination of electrons and holes from a pair of subbands, the PL spectrum from this recombination is given by [5]:

$$I(E) \propto \int_c d\mathbf{k}_c \int_v d\mathbf{k}_v f_c(1-f_v)\delta(E_c - E_v - E)\delta(\mathbf{k}_c - \mathbf{k}_v) \qquad (4\text{-}1)$$

where $\mathbf{k}_c$ and $\mathbf{k}_v$, E_c and E_v, f_e and f_v are the wave vectors, energies and the Fermi distribution functions for the electrons and holes respectively. Eq. (4-1) assumes **k**-conservation during the recombination process, and it has been shown to be valid for recombination at room temperature by Christen *et al.* [5] through a comparison of experimental and theoretical line shapes of the PL spectra of GaAs QWs. At low temperature they found evidence of non-**k**-conservation recombination and attributed it to the lateral localization of excitons in potential fluctuations caused by interface roughness. Therefore Eq. (4-1) should be applicable to our room temperature PL spectra. After integrating over **k**, Eq. (4-1) can be reduced to:

$$I(E) \sim \vartheta(E - E_g) f(\varepsilon_c + E_g)\left[1 - f(-\varepsilon_v)\right] \qquad (4\text{-}2)$$

where $\vartheta(E)$ is a step function describing the two-dimensional electron density of states, E_g is the band gap, $\varepsilon_{c(v)}$ is the reduced electron and hole energy, and it is given by:

$$\varepsilon_{c(v)} = \frac{m_{h(e)}}{m_e + m_h}\left[E - E_g\right] \tag{4-3}$$

where m_e and m_h are the effective masses of the electrons and holes respectively. The total PL spectrum is then a sum of all the possible transitions weighted by the respective oscillator strength M_i associated with each transition:

$$P(E) = \sum_i M_i I_i(E) \tag{4-4}$$

In carrying the lineshape fitting using Eq. (4-4), we have made the following approximations. First, since the photoexcited holes are known to thermalize rather quickly with the lattice [6], we have assumed a Boltzmann distribution for the holes. This can be used to explain the sharp fall off in the intensity of the high energy tail of the PL spectra at low temperature as shown in Fig. 4-3. Secondly, we only consider recombination of electrons with heavy holes, since this is the most dominant process [2, 3]. Thirdly, to better fit the low energy edge of the PL spectra, we have broadened density of states for each level from a simple step function by a Lorentzian as schematically shown in Fig. 4-4. A discussion of the broadening of PL peaks can be found in references [5, 7]. We note that choosing a broadened density of states does not affect the width of the PL spectra appreciably as the width is mostly determined by the electron density. Finally the oscillator strength M_i are treated as adjustable parameters. This is because the PL spectra we measured are time-integrated. They can be viewed as a superposition of many spectra taken at different time delay after the laser pulse. Use of pulsed laser excitation means that the electron density is time dependent. In addition, as Cingolani *et al.* have shown, the high electron density at small time delay will create a

large Fermi pressure for the EHP to expand, which in turn reduces the electron density [4]. Since the PL spectra are highly dependent upon the electron density, spectra taken at different time delay will have different line shapes. This has been confirmed by time-resolved PL measurement with a steak camera [8]. The high-energy tail mainly comes from emission at early time while the low energy part contains more emission at long delay time. Therefore it is almost impossible to deduce the exact oscillator strength associated with each transition from the time-integrated spectral. So we use instead the relative strength M_i of the transition as adjustable parameters in our fitting.

The dashed line in Fig. 4-5 show a fit to a PL spectra of the 165 Å quantum wells using Eq. 4-4. There are four subband levels involved, the calculated curve fits the experimental data quite well. The electron density obtained from this curve-fitting is 5.8×10^{12} cm $^{-2}$. We notice that the above fitting method generally works well for spectra obtained at high electron densities. For spectra obtained at low electron density ($<10^{11}$ cm^{-2}) or at low temperature, the quality of the fit actually deteriorates. This is likely to be due to the fact that at low electron density or at low temperature, exciton effects on the emission spectra have to be included, and the aforementioned theory breaks down.

4.3 Determination of the width of the quantum well from its PL spectrum

Our discussions in section 4.1 have shown that the PL peak positions correspond to the transition energy between electron and hole subbands. These peak positions can be used to calculate the confined energy levels. Through comparison with model calculations of the electron energy levels described in Section 2.1 of Chapter II, we can

deduce the width of the quantum well. Fig. 4-6 shows the plot of the PL peak positions versus the subband index for three different quantum well samples measured at room temperature or liquid nitrogen temperature. We found that fits of the peak positions to a quadratic dependence on the subband index n yielded the best result. PL peak positions are well described by the following equation:

$$E_n = E_0 + \Delta \times n^2 \tag{4-5}$$

We note that E_0 here is not the true band gap of GaAs. Miller *et. al.* have shown via PL excitation spectroscopy that the PL peaks of highly excited quantum wells correspond to transitions from the electron subbands to the first heavy hole subband [9]. In this context E_0 is the bulk band gap plus the confinement energy of the first heavy hole level (for quantum well width around 180 Å, the confinement energy of the heavy hole is about 2 meV), and Δ is the confinement energy of the first electron level.

We have also noticed that the quadratic dependence of the subband levels on the subband index also worked extremely well on the peak positions taken from the PL spectra for the highly excited GaAs/$Al_xGa_{1-x}As$ and $In_xGa_{1-x}As$/InP quantum wells in references [2, 3]. Typical error is less than 1%. As a result of this curve-fitting, we obtained two important parameters, namely the bulk GaAs band gap E_g (after subtracting off 2 meV from E_0) and the first electron subband energy level Δ. One can see that the value of Δ obtained for the three samples from fitting the room temperature data are quite consistent with those obtained from fitting the liquid nitrogen temperature data. As we have mentioned in Chapter II, the first subband level calculated using the Ben-Daniel Duke model (parabolic approximation) or the Bastard model (non-parabolic

approximation) yields essential the same value. By using the Ben-Daniel Duke model we found that the widths of the three quantum well samples are 165, 195 and 210 Å respectively. The band gap energy E_g = 1.430 eV at room temperature and E_g = 1.509 eV at liquid nitrogen temperature are in very good agreement with the values of 1.425 eV and 1.510 eV quoted in the literature.

The quadratic dependence of the subband levels on the subband index is consistent with the fact that we have a deep quantum well. However, when the electron energy is a few hundred meV above the bottom of the band, one may expect to see the effect of band non-parabolicity. A plot showing the comparison between calculations using parabolic band approximation and the Bastard model [10] is shown in Fig. 4-7. Clearly, the parabolic band approximation agrees very well with our experimental results while the Bastard model gives a much lower energy level for high index subbands (the difference can be as large as 50 meV). There are some studies in the literature about the effect of band non-parabolicity on the subband levels [10, 11], and an energy dependent effective mass associated with the band non-parabolicity is often used in the calculation which results in lower subband levels than those obtained with parabolic band approximation. These studies often focused on low index subbands of quantum wells with small well widths where the separation between subbands are relatively large and non-parabolicity is expected to have a more pronounced effect, however there is considerable spread among the results [12]. Our finding that band non-parabolicity has little effect on the subband levels requires further theoretical investigation into this subject.

In summary we have studied the PL spectra under high intensity excitation in GaAs/AlAs quantum wells. These spectra reveal strong band filling and band gap renormalization. Despite the many body interactions, PL peak positions still correspond to the transitions between electron and hole subbands. The position of the PL peaks can be well described by a quadratic dependence on the subband index. even for electron energy as high as about 250 meV above the bottom of the first subband. Band non-parabolicity seems to play a minimum role in determining the confined electron energy levels. Through curve-fitting, we have determined the average electron areal density and the width of the quantum wells both of which are important parameters for our experimental investigation of the non-equilibrium phonons in quantum wells described in Chapter III.

References

[1] S. Schmitt-Rink and C. Ell, J. Lumin. **30,** 585 (1985); D.A. Kleinmen and R. C. Miller, Phys. Rev. B **32,** 2266 (1985); S. Das Sarma, R. Jalabert, and S.-R. Eric Yang, Phys. Rev. B **41**, 8288 (1990); J. C. Ryan and T. L. Reinecke, Phys. Rev. B **47**, 9615 (1993)

[2] E. Lach, A. Forchel, D. A. Broido, T. L. Reinecke, G. Weimann and W. Schlapp, Phys. Rev. B **42**, 5395 (1990).

[3] V. D. Kulakovskii, E. Lach, A. Forchel, and D. Grutzmacher, Phys. Rev. B **40**, 8087 (1990)

[4] R. Cingolani, K. Ploog, A. Cingolani, C. Moro and M. Ferrara, Phys. Rev. B **42**, 2893 (1990).

[5] J. Christen and D. Bimberg, Phys. Rev. B **42**, 7213 (1990).

[6] J. Shah, B. Deveaud, T.C. Damen, W. T. Tsang, and P. Lugli, Phys. Rev. Lett. **59**, 2222 (1987).

[7] P.T. Landsberg, Phys. Stat. Sol. **15**, 623 (1966).

[8] R. Cingolani, L. Lage, L. Tapfer, H. Kalt, D. Heitmann, and K. Ploog, Phys. Rev. Lett. **67**, 891 (1991).

[9] R. C. Miller, D. A. Kleinman, O. Muntaenu, and W.T. Tsang, Appl. Phys. Lett. **39**, 1 (1981)

[10] G. Bastard, Phys. Rev. B **25**, 7584 (1982); G. Bastard and J. A. Brum, J. of Quan. Elec. QE-22, 1625 (1986).

[11] U. Ekenberg, Phys. Rev. B **40**, 7714(1989); D. F. Nelson, R. C. Miller, and D. A. Kleinman, Phys. Rev. B **35**, 7770 (1987), K. H. Yoo, L.R.Ram-Mohan and D. F. Nelson, Phys. Rev. B **39**, 12808 (1989).

[12] See, for example, E. Finkman, M.D. Sturge, M.-H. Meynadier, R. E. Nahory, M.C. Tamargo, D. M. Hwang and C.C. Chang, J. Lumin. **39**, 57 (1987).

Figure Captions for Chapter IV

Fig. 4-1 Time-integrated photoluminescence spectra of a 210 Å GaAs/AlAs quantum well measured at room temperature for various electron densities. The electron densities are obtained from curve-fitting described in the text. PL peaks correspond to exciton transitions in the quantum well.

Fig. 4-2 Time-integrated photoluminescence spectra of a 165 Å GaAs/AlAs quantum well measured at room temperature for various electron densities.

Fig. 4-3 Time-integrated photoluminescence spectra under high intensity excitation of (a) a 210 Å GaAs/AlAs quantum well; (b) a 165 Å GaAs/AlAs quantum well measured at liquid nitrogen temperature.

Fig. 4-4 A schematic diagram of the broadened density of states (solid line) used in the lineshape fitting. This is similar to an energy level broaden by a Lorentzian function. The step-function like density of state for an ideal two-dimensional electron gas is shown in dash line.

Fig. 4-5 A time-integrated photoluminescence spectrum of a 165 Å GaAs/AlAs quantum well measured at room temperature. The dashed line is the result of a theoretical curve-fitting based on Eq. (4-4). The average areal electron density obtained from the fitting is 5.8×10^{12} cm^{-2}.

Fig. 4-6 A plot of the photoluminescence peak positions versus the subband index for three different GaAs/AlAs quantum wells. (a) Measurement done at liquid nitrogen temperature, (b) measurement done at room temperature. Symbols are experimental data, solid lines are quadratic fits to the data. The gap energy E_0 and the confinement energy Δ for the first subband obtained from fitting are also shown in the plot. Data measured at different temperature show good consistency. Quantum well widths are obtained by comparing the value of Δ with the results of model calculation described in section 2.1 of Chapter II.

Fig. 4-7 A comparison between the energy levels calculated using different models for (a) a 195 Å GaAs/AlAs quantum; (b) a 165 Å GaAs/AlAs quantum well. Symbols are experimental data, solid lines are from a parabolic band approximation, dashed lines are from the Bastard's four band model.

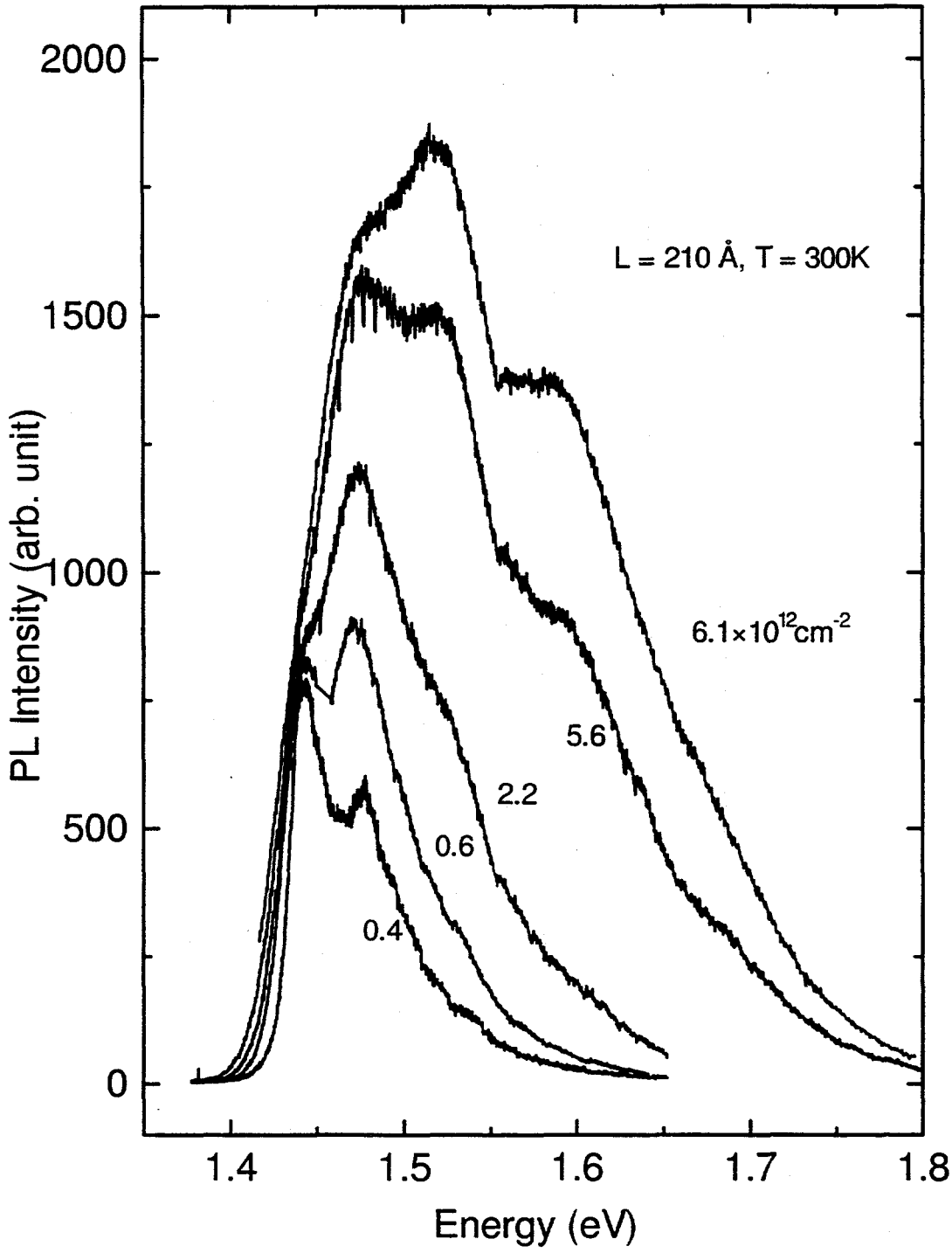
2000
1500
1000
500
0
PL Intensity (arb. unit)
1.4
1.5
1.6
1.7
1.8
Energy (eV)
L = 210 Å, T = 300K
6.1×10^12cm^-2
5.6
2.2
0.6
0.4

Figure 4 - 1

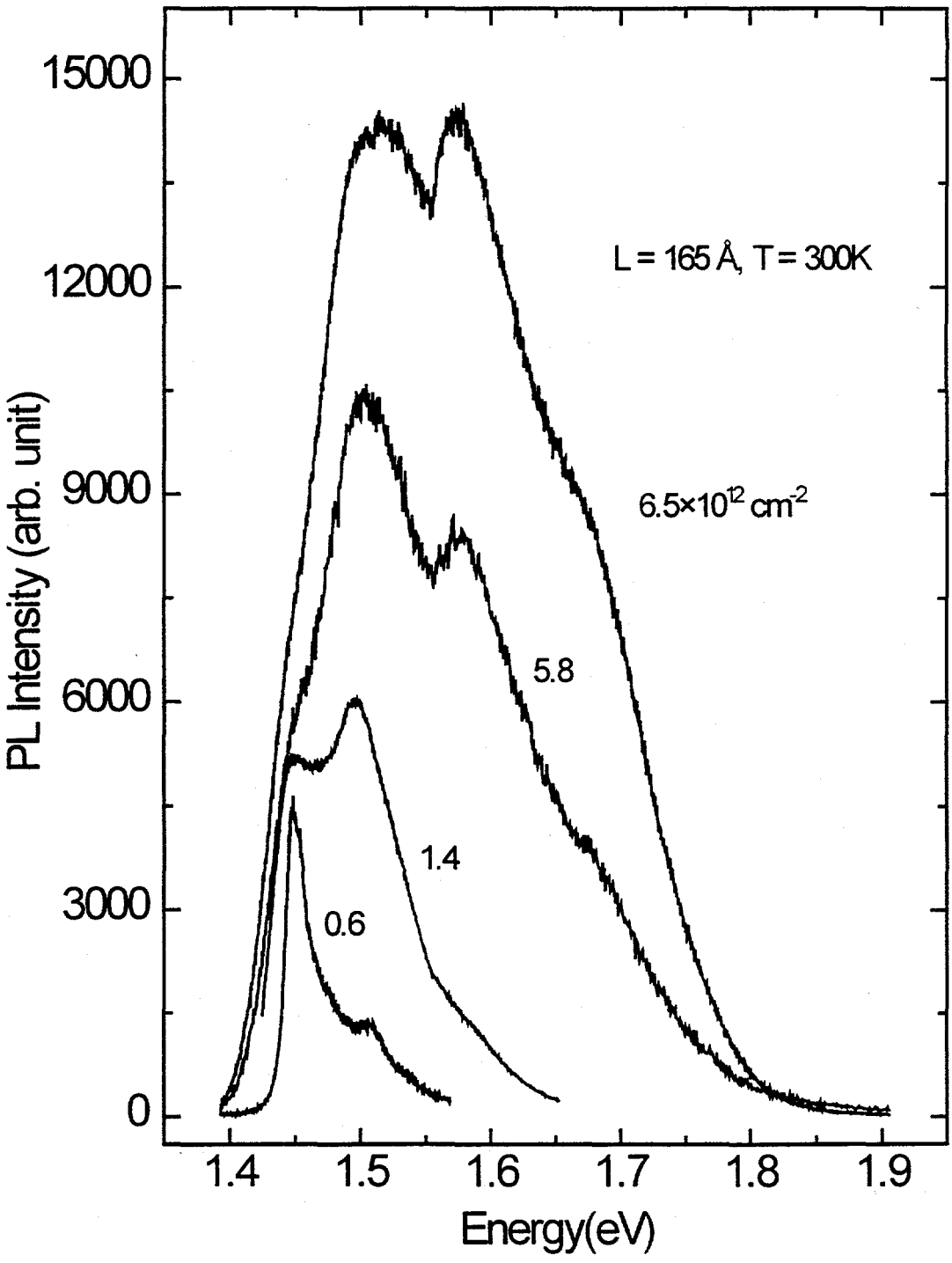
15000
12000
9000
6000
3000
0
PL Intensity (arb. unit)
1.4
1.5
1.6
1.7
1.8
1.9
Energy(eV)
L = 165 Å, T = 300K
6.5×10^12 cm^-2
5.8
1.4
0.6

Figure 4 - 2

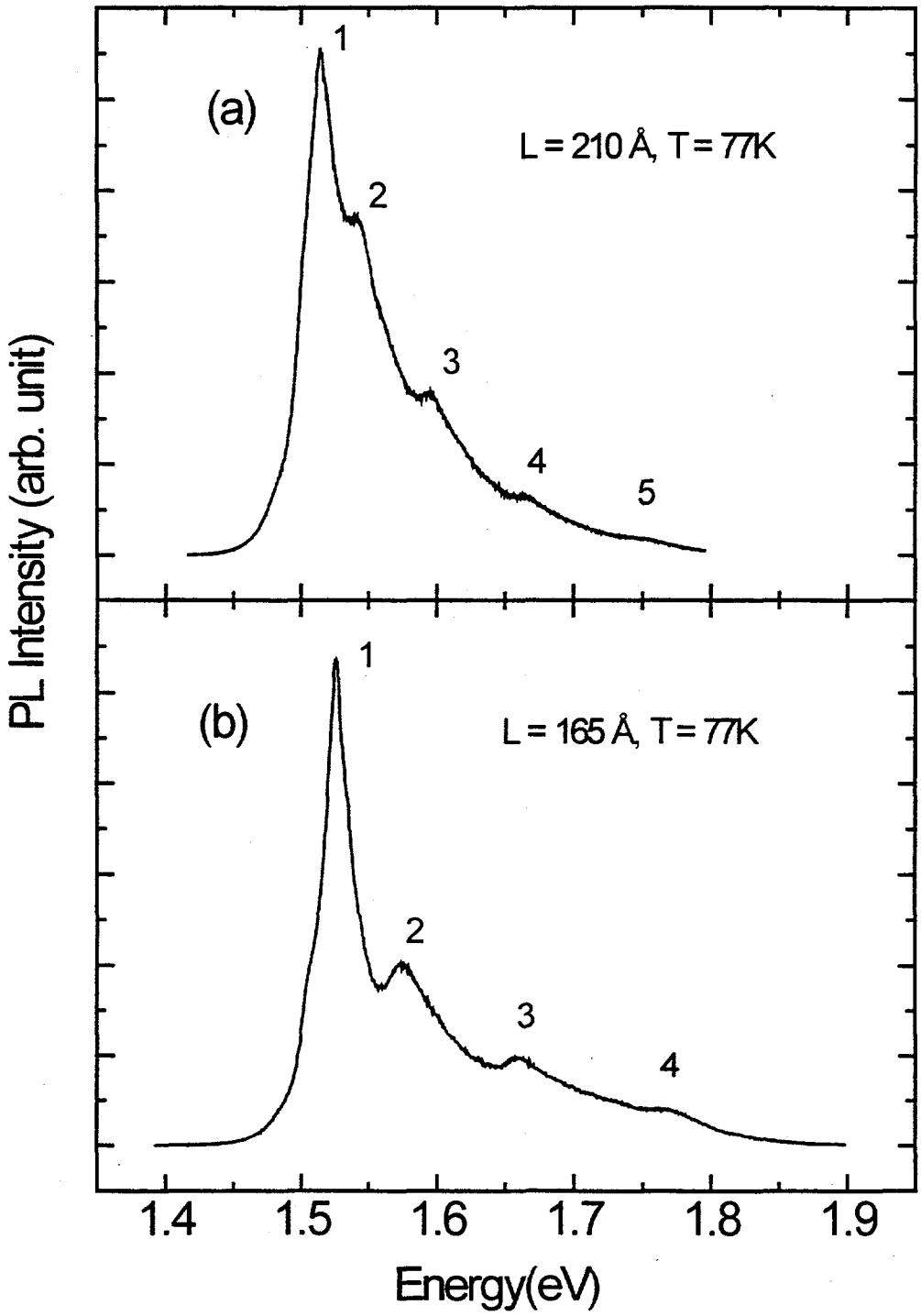
(a)
L = 210 Å, T = 77K
1
2
3
4
5
(b)
L = 165 Å, T = 77K
1
2
3
4
PL Intensity (arb. unit)
1.4
1.5
1.6
1.7
1.8
1.9
Energy(eV)

Figure 4 - 3

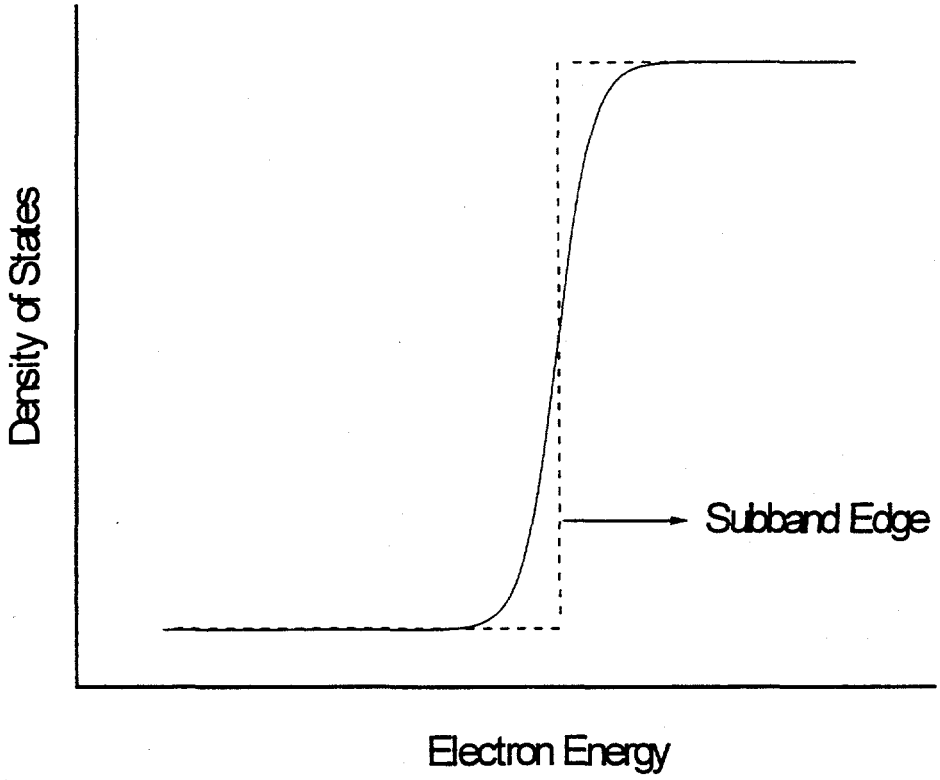

Figure 4 - 4

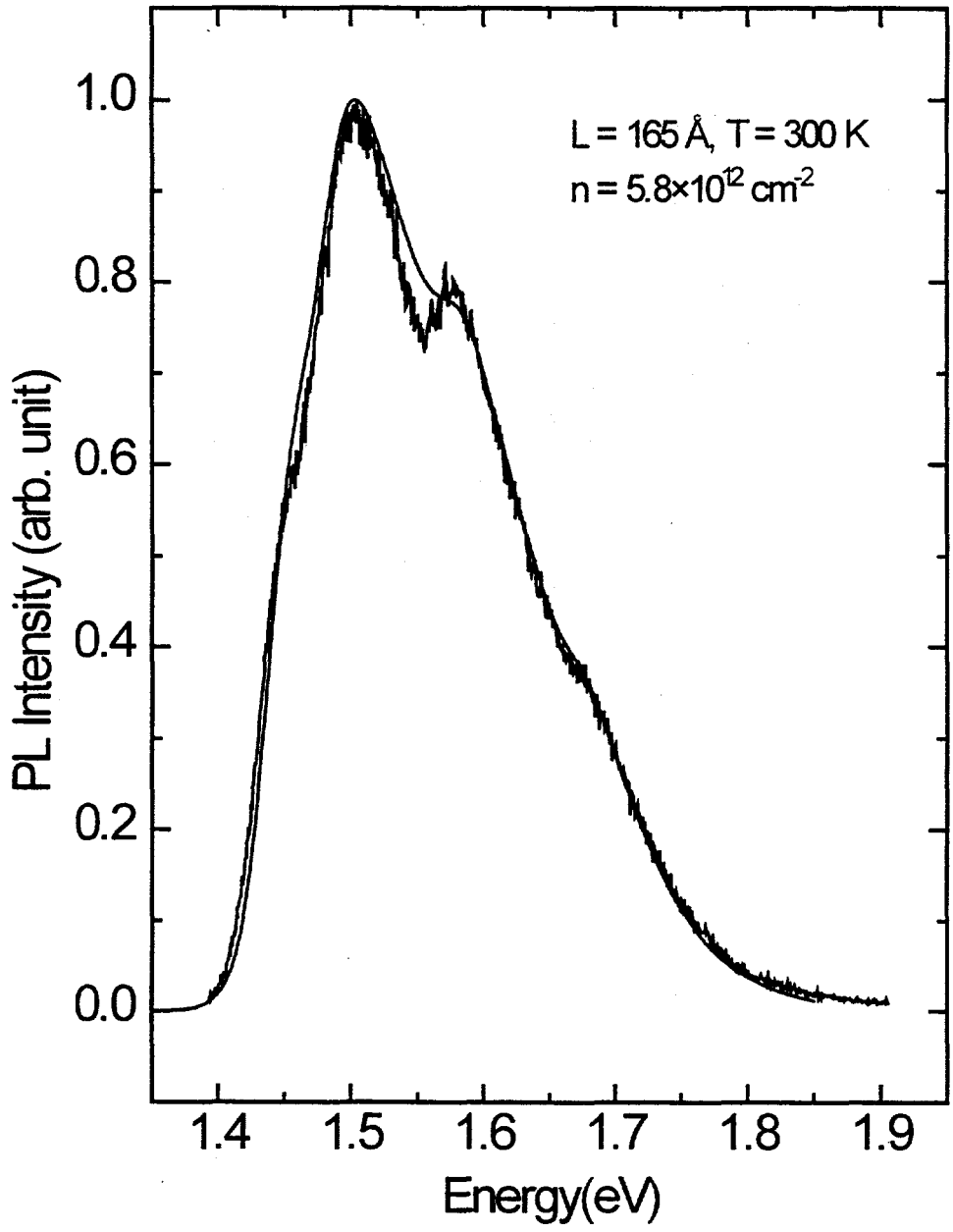
L = 165 Å, T = 300 K
n = 5.8×10^12 cm^-2
PL Intensity (arb. unit)
Energy(eV)
0.0
0.2
0.4
0.6
0.8
1.0
1.4
1.5
1.6
1.7
1.8
1.9

Figure 4 - 5

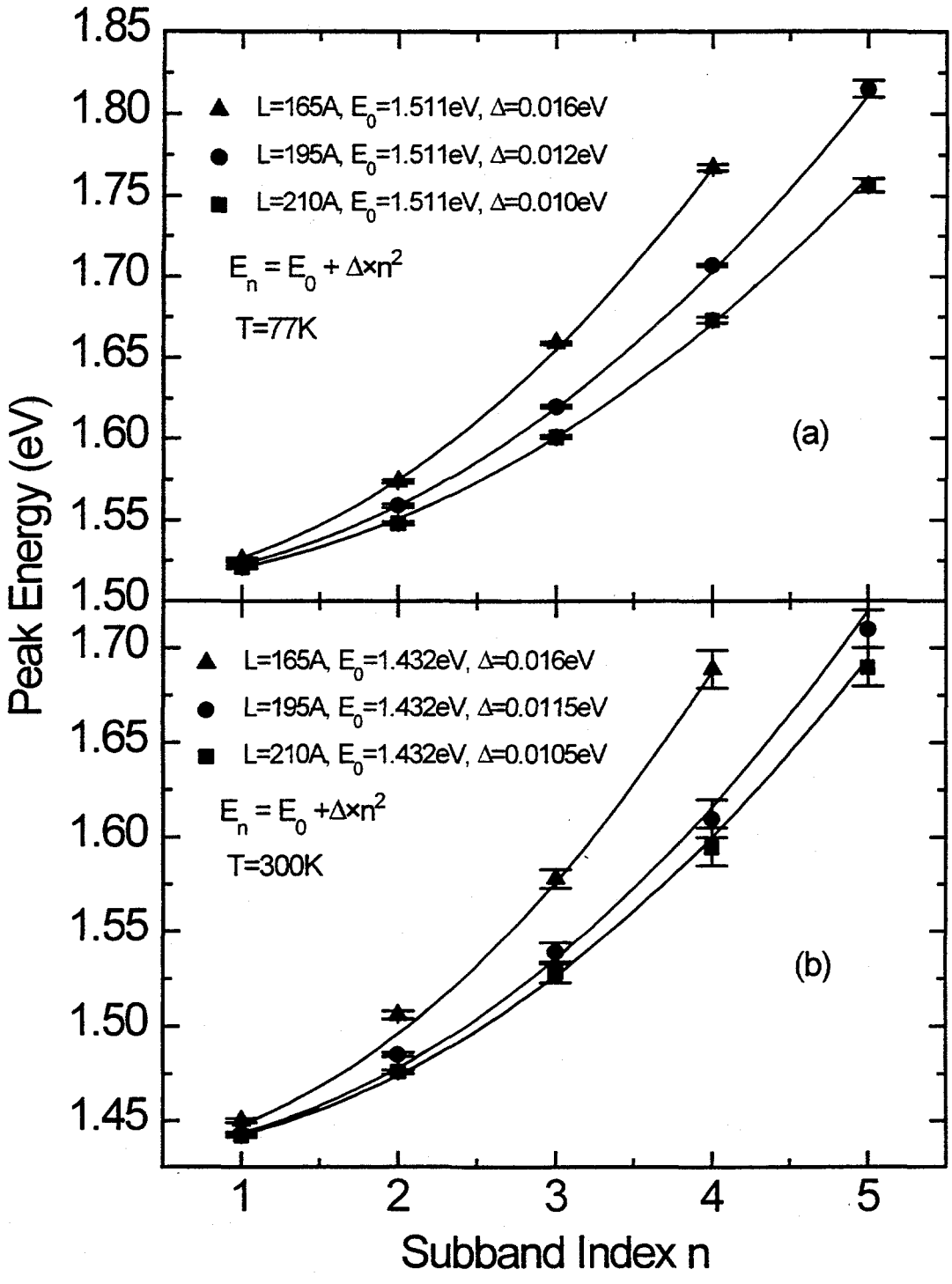
1.85
1.80
1.75
1.70
1.65
1.60
1.55
1.50
L=165A, E0=1.511eV, Δ=0.016eV
L=195A, E0=1.511eV, Δ=0.012eV
L=210A, E0=1.511eV, Δ=0.010eV
En = E0 + Δ×n2
T=77K
(a)
1.70
1.65
1.60
1.55
1.50
1.45
L=165A, E0=1.432eV, Δ=0.016eV
L=195A, E0=1.432eV, Δ=0.0115eV
L=210A, E0=1.432eV, Δ=0.0105eV
En = E0 +Δ×n2
T=300K
(b)
Peak Energy (eV)
1
2
3
4
5
Subband Index n

Figure 4 - 6

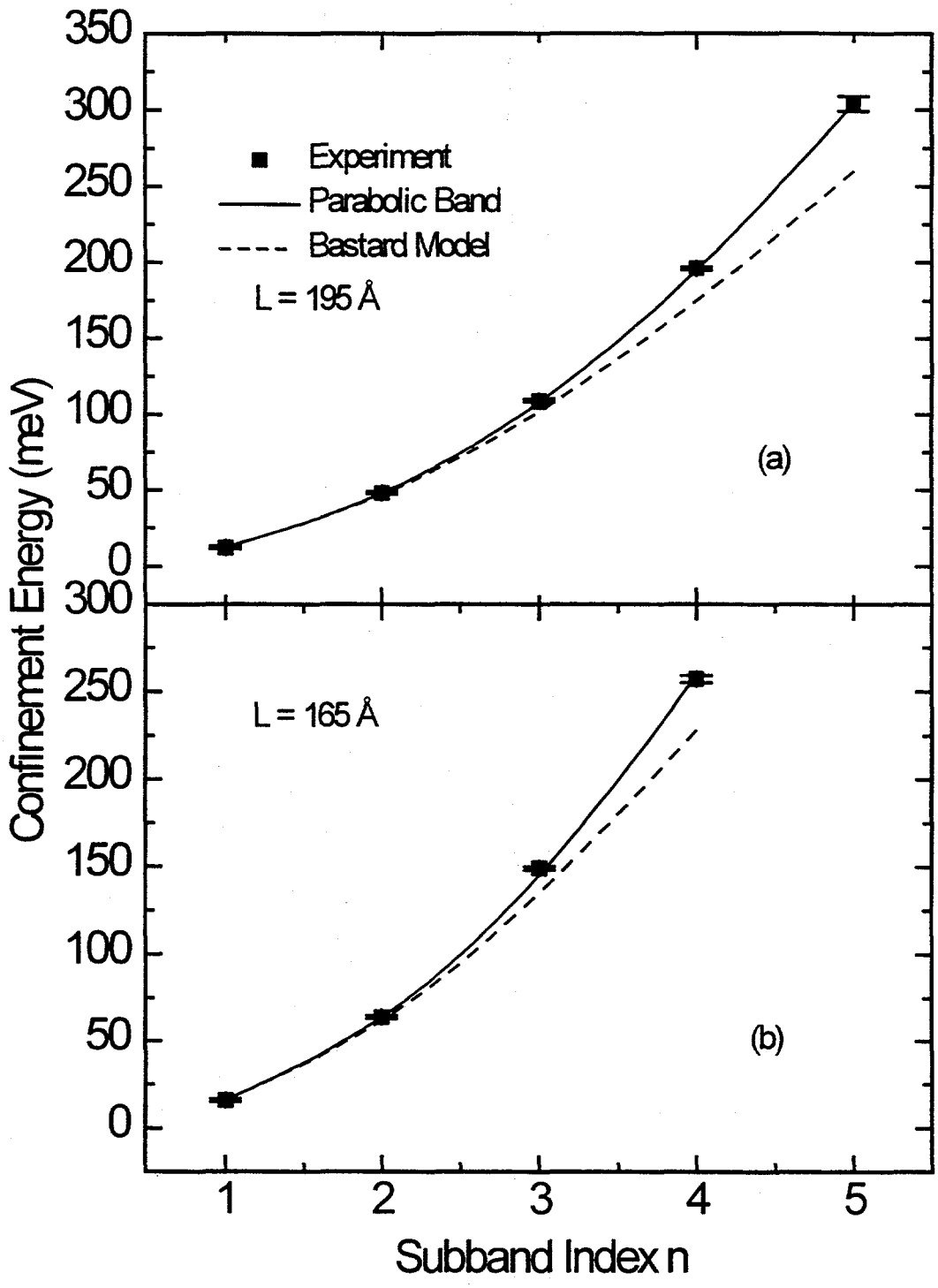
Confinement Energy (meV)
Subband Index n
Experiment
Parabolic Band
Bastard Model
L = 195 Å
L = 165 Å
(a)
(b)
350
300
250
200
150
100
50
0
300
250
200
150
100
50
0
1
2
3
4
5

Figure 4 - 7

Chapter V: Probing Optical Phonon Propagation in $GaAs/Al_xGa_{1-x}As$ Quantum Wells via Non-Equilibrium Phonon Populations

In this chapter we will examine the issue of confinement and propagation of optical phonons in $GaAs/Al_xGa_{1-x}As$ quantum wells. Recently, Kim *et al.* [1-3] have studied NOP occupancy in a series of $GaAs/Al_xGa_{1-x}As$ quantum wells as a function of either the Al fraction x or the thickness of the barrier (L_b), and they found a sudden increase in NOP population when $x < 0.3$ or when the barrier is thinner than 10 Å. Kim and co-workers have interpreted these results as due to a sudden transition of the optical phonons in the well from a confined state to a propagating state. These experimental results have stimulated much theoretical interest in the issue of phonon confinement and propagation in quantum wells [4-7]. However, there appear to be no theoretical underpinning of the NOP technique in determining whether a phonon is confined or propagating. Here, we perform a model calculation of the NOP distribution, and examine quantitatively the consequences of phonon confinement and propagation on the NOP population observed by Raman backscattering experiments. We argue that the relaxation rates of energetic hot electrons in quantum wells and superlattices are essentially the same as in bulk samples. We can then perform analytical calculations to relate the coherence length of LO phonons in the growth direction to the observed NOP population. We then analyze the NOP experiments by Kim *et al.*. Using this model, we show that the coherence length of the LO phonons is a sensitive function of x. Therefore, whether LO

phonons are localized within a quantum well or can penetrate into adjacent wells depends very much on the structural parameters of the samples.

5.1 Wave vector of confined and propagating LO phonons probed by Raman scattering

Let us begin our discussion by defining the back-scattering geometry in most NOP experiment, which is schematically shown in Fig. 5-1 along with a schematic picture of the wave function for the Raman-active LO phonon. We have shown in Chapter II that in such a scattering geometry, Raman scattering probes only phonons with $Q_z \sim 7\times10^5$ cm^{-1} in bulk GaAs due to quasi-momentum conservation. Since this happens to be very close to the peak of the NOP distribution for bulk GaAs, one usually measures a relatively large NOP occupation number as predicted by theory. On the other hand, quasi-momentum conservation along the quantum well plane direction dictates that Raman back-scattering will be able to probes only phonons with $Q_{//} < 10^5$ cm^{-1} in GaAs/AlAs quantum wells. And from our model calculations in Chapter II, we know that there is no NOP in this wave vector range except in the case when the separation of two subbands is close to the LO phonon energy, and resonant intersubband scattering of optical phonons (RISOP) becomes possible. So in principle one does not expect to measure any NOP in quantum wells via Raman back-scattering. However, as we have discussed in Chapter III, the breakdown of quasi-momentum conservation caused by defect or impurity may allow resonant Raman scattering to probe a much wider range of in-plane phonon wave vectors, allowing one to measure a small NOP occupancy.

Following this argument, we can see that when the observed NOP occupancy drops precipitously, it may be suggestive of a transition from a three dimensionally propagating phonon mode to a confined phonon mode of two dimensional nature. The above discussion only applies to the two extreme cases of pure 3-D and 2-D, and there is no theory that can accurately describe the transition region. In order to bridge the transition from a propagating mode to a confined mode, what we will do here is to start out from the 3-D extreme and assume that the propagating phonon modes have an infinite spatial extent. Then we introduce a coherence length ξ to describe a phonon wave packet of finite size. By changing the coherence length or the size of the wave packet, we try to simulate the transition from a propagating to a confined mode. We will examine how the NOP occupancy is affected by the phonon coherence length ξ.

We first consider the wave function of a propagating optical phonon mode (also referred to as a folded optical phonon mode in the literature) which would be valid for superlattices with ultrathin barriers or $Ga_xAl_{1-x}As$ barriers with low Al concentration. The Bloch function of the phonon mode is given by:

$$\Psi_q = \exp(iqz)u_q(z) \tag{5-1}$$

where u_q is a periodic function with periods equal to $L_z + L_b$, L_z and L_b being, respectively, the well and barrier widths. The wave vector $\boldsymbol{Q}$ of the Raman-active modes in this case is determined by both the bulk property and the period of the superlattice:

$$Q_z = Q_0 \pm 2m\pi/(L_z + L_b) \tag{5-2}$$

where m = 0, 1, 2..., and Q_0 is the wave vector of the Raman-active phonons in bulk GaAs as defined by the scattering geometry. The strongest Raman peak will have Q_z corresponding to m = 0 and hence Q is essentially the same as in bulk GaAs. In other words when optical phonons can propagate in a superlattice, the wave vector of the strongest mode probed by Raman scattering is essentially the same as in bulk GaAs. This is shown more clearly in Fig. 5-2 where the solid curve is a schematic wave function of a Raman-active propagating optical phonon mode in a superlattice. Notice that the dominant Fourier component for this wave function occurs at $Q_0 = 2\pi / \lambda_0$. When compared with the corresponding phonon wave function in the bulk in Fig. 5-1 one sees that phonons of essentially similar wave vectors are probed by Raman scattering in superlattices and in the bulk.

When the phonon starts to change from a propagating mode to a localized mode (Fig. 5-3), phonon wave function will no longer be infinitely extended, instead it will form a wave packet of finite size. The spatial confinement of the phonon wave function results in a spread of wave vector around Q_0. The more the phonon is localized, the smaller the wave packet, then larger is the spread in its wave vectors. Therefore Raman scattering will not just be probing one single phonon wave vector, but a range of wave vectors around Q_0 in this case. As we shall see in the following sections, this will have an important consequence on the NOP occupancy measured by Raman scattering, and hence the ability of NOP as a probe of the spatial extent of LO phonons.

5.2 Model calculations of non-equilibrium phonon distributions in bulk GaAs

To decide whether the NOP can be a sensitive tool to determine the spatial extent of the LO phonons, we need to know first the distribution of NOP generated by hot electron relaxation. We know that in quantum wells with large well width, phonons will only be weakly confined, and as the well width increases, the constraint on the phonon propagation will gradually disappear, and we should be gradually approaching the bulk limit. In principle, we can use the models in Chapter II to calculation the NOP. However, for well width approaching infinity, the subbands are closely spaced. To include all of them in the calculation is computationally impossible. On the other hand, we know that in this extreme quantum wells should behavior like a bulk material. Therefore, we will start out by assuming a bulk GaAs NOP distribution for the propagating phonons considered here. We can calculate the NOP distribution N_q generated by hot electron relaxation in bulk GaAs in a similar fashion as we did in Chapter II using the following rate equation:

$$\frac{\partial N_q}{\partial t} = \frac{2\pi}{\hbar}(N_q + 1)\Sigma_K \left|M_q\right|^2 f(\mathbf{K},t)\left[1 - f(\mathbf{K}-\mathbf{q},t)\right]\delta(E_{K-q} - E_K + E_{LO})$$

$$-\frac{2\pi}{\hbar}N_q \Sigma_K \left|M_q\right|^2 f(\mathbf{K},t)\left[1 - f(\mathbf{K}+\mathbf{q},t)\right]\delta(E_{K+q} - E_K - E_{LO}) - \frac{N_q}{\tau_q} \qquad (5\text{-}3)$$

where $|M_q|^2$ is the bulk GaAs electron-LO phonon (Fröhlich) interaction matrix element squared, $\boldsymbol{K}$, E_K and $f(\mathbf{K},t)$ are, respectively, the electron wave vector, energy and distribution function, E_{LO} and τ_q are, respectively, the LO phonon energy and lifetime. Although both electrons and holes are excited by the pump laser, most of the excess energy of the photon is imparted to the electrons due to their much lighter effective mass

and hence we have neglected the hole contribution to N_q in Eq. (5-3). In experiments where the NOP population in GaAs is probed at low temperatures within a few ps after excitation by a pump pulse, the phonon decay term in Eq. (5-3) can be neglected since τ_q is about 10 ps long.

In bulk GaAs the Fröhlich interaction matrix element $|M_q|^2$ is given by the familiar expression:

$$\left|M_q\right|^2 = \frac{2\pi e^2}{Vq^2}\left(\frac{1}{\varepsilon_\infty} - \frac{1}{\varepsilon_0}\right)E_{LO} \tag{5-4}$$

where e is the electron charge, V is the volume of the crystal, ε_∞ and ε_0 are, respectively, the high frequency and low frequency dielectric constants. We assume that the excited electron-hole density is $<10^{17}$ cm^{-3} so that screening of the Fröhlich interaction by the photoexcited electrons is negligible. On the other hand the density is $>10^{15}$ cm^{-3} so that the electron thermalization time is much less than the laser pulse duration of about 1 ps. By assuming that the electron distribution function can be approximated by a Boltzmann distribution with temperature T_e, and that there is only one spherical conduction band, Eq. (5-3) can be integrated to yield:

$$\frac{\partial N_q}{\partial t} = \frac{2E_{LO}e^2}{\hbar^2 c}\left[\frac{2\pi^2 m^* c^2}{k_b T_e}\right]\left(\frac{1}{\varepsilon_\infty} - \frac{1}{\varepsilon_0}\right)\frac{N_e}{q^3}\exp\left(-\frac{E_{q2}}{k_b T_e}\right)\left(1 - \frac{N_q}{N_{eq}}\right) \tag{5-5}$$

In Eq. (5-5) N_e is the electron density, k_b is the Boltzmann constant, m^* is the electron effective mass, E_{q2} and E_q are defined as:

$$E_{q2} = \frac{\left(E_q + E_{LO}\right)^2}{4E_q} \tag{5--6}$$

and

$$E_q = \frac{\hbar^2 q^2}{2m^*} \tag{5-7}$$

and N_{eq} is the LO phonon population when the electrons and the LO phonons are in thermal equilibrium :

$$N_{eq} = \frac{1}{\exp\left(\frac{E_{LO}}{k_b T_e}\right) - 1} \tag{5-8}$$

The generation of NOP via the relaxation of hot electrons cools the electron gas so that T_e is a function of time, and hence N_{eq} also depends on time. The rate equation for the average energy of an electron $\langle E \rangle = (3/2)k_b T_e$ is given by:

$$\frac{\partial \langle E \rangle}{\partial t} = -\frac{E_{LO}}{N_e} \int \left(\frac{\partial N_q}{\partial t}\right) D_q d\mathbf{q} \tag{5-9}$$

where D_q represents the LO phonon density of states.

Fig. 5-4 shows the NOP distribution obtained by solving simultaneously Eqs. (5-6) and (5-9) for a bulk GaAs under the assumption that the electrons are excited by a delta-function pulse in time with initial average electron energy of 0.5 eV. The NOP distribution is measured at 1 ps after the passage of the excitation pulse. The material parameters of GaAs going into this calculation can be found in Table I in Chapter II. There are two important features in Fig. 5-4 that worth noting. First, there is a peak in

N_q occurring at the value of q ~ 4×10^5 cm^{-1} which is very close to the value of Q_0 in Raman scattering in bulk GaAs. Secondly, N_q drops very rapidly to zero as the value of q decreases. This sharp cut-off in N_q occurs at q_{min}~$2x10^5$ cm^{-1}. The existence of this cut-off in N_q has already been mentioned in Chapter II and it results from the conservation of energy and momentum during the electron-LO phonon scattering process. The value of q_{min} is determined by the LO phonon energy and the electron effective mass m^*. We should point out that the NOP distribution in bulk GaAs generated by the relaxation of a nonequilibrium distribution of electrons has been calculated previously by Collins and Yu [8]. These authors have assumed a lower electron density ($<10^{16}$ cm^{-3}) so that the electron-electron interaction can be neglected. As a result, their nonequilibrium electron distribution was represented by a series of delta functions (as opposed to the Boltzmann distribution assumed in the present calculation) separated from each other in energy by the LO phonon energy. In spite of this difference their results are qualitatively similar to ours because the peak in N_q and the cut-off at q_{min} are both determined by the band curvature and the LO phonon energy and therefore are not very sensitive to the electron distribution. Calculations similar to ours but including screening and other effects have recently been presented by other groups [9, 10].

5.3 Effects of phonon localization on non-equilibrium phonon occupancy observed in Raman scattering

As we have discussed in Section 5.1, the wave vector probed by Raman scattering for propagating phonons with infinite spatial extent is the same as that in the

case of bulk GaAs, therefore we have the largest NOP value as Q_0 is close to the NOP peak position. For propagating phonons with a finite spatial extent ξ, Raman scattering will probe a range of phonon wave vectors around Q_0, and since NOP has certain distribution in momentum space, probing a range of wave vectors will result in a decrease in the measured NOP occupancy when NOP of smaller occupancy are included. When the phonons are localized in quantum wells, the coherence length is equal to well width L_z, so the wave vectors of phonons sampled by Raman scattering is determined mainly by the well width L_z and can be much larger than Q_0 if L_z is small (say on the order of 100 Å). When Q_R is much larger than 10^6 cm^{-1} (the position of the peak in the hot phonon distribution function), the measured NOP population is expected to be significantly smaller than that of bulk GaAs.

To quantitatively examine the effect of a finite coherence length on the measured NOP, we utilize the following relation:

$$\lim_{\eta\to 0} e^{-\frac{x^2}{\eta^2}} = \sqrt{\pi}\eta\delta(x) \tag{5-10}$$

where $\delta(x)$ is the Dirac delta function. Using Eq. (5-10), we can write the NOP observed by Raman scattering in bulk GaAs as:

$$\langle N_{Q_0} \rangle = \int N_q \delta(q - Q_0) d\mathbf{q} \tag{5-11}$$

Then, to introduce a coherence length ξ for the phonon, we can use the Gaussian function in Eq. (5-10) to approximate the delta function in Eq. (5-11) and arrive at the result:

$$\left\langle N_{Q_0} \right\rangle = \frac{\xi}{\sqrt{\pi}} \int N_q e^{-\xi^2 (q-Q_0)^2} d\mathbf{q} \tag{5-12}$$

Let us examine the implications of Eq. (5-12). When the coherence length ξ goes to infinity, we recover the bulk limit where only N_{Q_0} is measured . On the other hand, when the coherence length is determined by the well width L_z, the region of wave vectors probed is a Gaussian centered around Q_0, with its full width at half maximum given by $\sim(\log_e 2)^{1/2}/L_z$, as schematically shown in Fig. 5-5. As a result of this averaging over those contributions from the relatively large q phonons with small nonequilibrium population, the measured NOP population would be smaller than that of bulk GaAs. As pointed out before only the peak of the NOP distribution is probed in the latter case.

The expression in Eq. (5-12) allows the coherence length of the LO phonons to be related to the NOP population observed by Raman scattering. In real space, Eq. (5-12) corresponds to making the following approximation for the Raman-active phonon wave function (Ψ_R), which is the Fourier transform of $\exp[-\xi^2 (q - Q_0)^2]$:

$$\Psi_R = \left[\frac{1}{4\pi\xi^2}\right]^{\frac{1}{4}} \exp(iQ_0 z) \exp\left(-\frac{z^2}{4\xi^2}\right) \tag{5-13}$$

The wave function in Eq. (5-13) has the advantage that it can be applied to both the bulk propagating phonons and to the confined ones in describing their spatial extent. In principle, one can further generalize the wave function in Eq. (5-13) to describe a Bloch wave of a finite spatial extent, as schematically shown in Fig. 5-6, with the following expression:

$$\Psi_R = \left[\frac{1}{4\pi\xi^2}\right]^{\frac{1}{4}} \exp(iQ_0 z)\exp\left(-\frac{z^2}{4\xi^2}\right)u_{Q_0}(z) \qquad (5\text{-}14)$$

Where $u_{Q_0}(z)$ is a periodic function with the periodicity of the superlattice. In the schematic picture of the phonon wave function shown in Fig. 5-6, we purposely omit the phase factor $\exp(iQ_0 z)$. However, as far as NOP is concerned it is difficult to determine the periodic part of the wave function. In any case we do not expect that using Eq. (5-14) instead of Eq. (5-13) would change the results appreciably. In particular if $Q_0\xi$ is $<<1$ then the periodic part is completely negligible. Therefore, from now on we shall concentrate on the relationship between the NOP population measured and the phonon coherence length ξ using Eq. (5-12). This approximation is equivalent to using the Gaussian wave function in Eq. (5-13) instead of the Bloch wave function in Eq. (5-14).

With the above approximation we can calculate, from the theoretical hot phonon distribution of Fig. 5-5, the normalized NOP population measured in Raman scattering as a function of ξ. It is assumed that the NOP population is normalized to the value for bulk GaAs which corresponds to ξ approaching infinity. The results are shown in Fig. 5-7. We note that the NOP population increases monotonically with ξ. It goes to zero as ξ approaches zero because Raman scattering starts to probe more large wave vector LO phonons with small occupation numbers. One may say that Fig. 5-7 is the basis for using the experimental normalized NOP population as a probe of the coherence length or the spatial extent of the Raman-active LO phonon modes. It should be kept in mind that the various approximations used in arriving at Fig. 5-7 make it difficult to determine quantitatively the coherence length. However, if the wave function of the phonon

involved changes suddenly from that of a propagating wave to a localized one as in an Anderson localization, we expect a large sudden decrease in ξ accompanied by a corresponding decrease in the NOP population. With this in mind, we shall analyze in the next section some Raman measurements of the NOP population performed on GaAs/$Al_xGa_{1-x}As$ quantum wells in which the phonon coherence length is varied by changing the structural parameters, such as the Al concentration in the $Al_xGa_{1-x}As$ barrier layers.

5.4 Discussion of non-equilibrium phonon population in GaAs/$Al_xGa_{1-x}As$ quantum wells

Recently, Kim *et al.* have studied over 30 GaAs/$Al_xGa_{1-x}As$ quantum well samples with a constant well width L_z = 100 Å and barrier width L_b > 20 Å but with different amounts of Al fraction x in the barrier. The NOP population was determined from the ratio of Stokes to anti-Stokes intensities after correcting the resonant Raman effect and subtracting the thermal background phonon population. The experimental details have been described in references [1-3]. Fig. 5-8 shows the NOP populations normalized to the bulk value (solid circles) as a function of the aluminum fraction x measured by Kim *et al.*. For L_b > 20 Å the NOP population depends only weakly on L_b, but more strongly on x [1]. And each data point in Fig. 5-8 represents the averaged result of many samples with different L_b's but with the same nominal x. The striking feature in Fig. 5-8 is that the normalized NOP population drops quickly to only 0.1 for x between 0.2 to 0.4. This result was found to be essentially independent of temperature.

We interpret the sudden decrease in the NOP population in terms of a corresponding decrease in the coherence length of the LO phonons along the growth direction. By combining Figs. 5-7 and 5-8 we can obtain a plot of the LO phonon coherence length ξ as a function of x. To obtain such a plot we first draw a smooth curve through the data points in Fig. 5-8 (solid curve) and the resultant ξ versus x plot is shown in Fig. 5-9. The main feature to note in Fig. 5-9 is that, for x between 0.2 to 0.4, ξ drops to a small constant value of around 60 Å. If the GaAs LO phonons become localized completely within the quantum well as x exceeds some critical value then we expect the coherence length to reduce to the well width of 100 Å. Considering the simplifications we have made, the difference of a factor of ~2 between the value of coherence length deduced and the well width is not unreasonable. The important point is that Fig. 5-9 does show *the spatial extent of the LO phonon wave function, as deduced from the NOP experiment, approaches a constant value of the order of magnitude of the well width for x exceeding a certain critical value*. This is exactly what is expected from a simple physical picture in which the GaAs phonon wave function can penetrate through the $Al_xGa_{1-x}As$ barrier when x is small. But as the Al concentration increases the phonon will be scattered by the Al atoms with smaller masses than the Ga atoms. For x larger than a certain value the GaAs phonons will be localized inside the well and the coherence length reduces to the well width. Thus we contend that, even given our many simplifications, the NOP technique is at least capable of distinguishing between an extended phonon mode and a localized one. In the case of the LO phonons in $GaAs/Al_xGa_{1-x}As$ quantum wells this transition from an extended to a localized mode occurs when x is somewhere

between 0.2 and 0.4. We shall discuss the implications of this result in the following paragraphs.

We first consider whether the above conclusion regarding the spatial property of LO phonons in GaAs/$Al_xGa_{1-x}As$ is consistent with existing theories and experimental results. Multiple LO phonon peaks in the Raman spectra of GaAs/AlAs quantum wells have been reported by many authors [11]. It is now generally agreed that these peaks result from the confinement of the LO phonons, either in the GaAs well or in AlAs barrier. Both kinds of phonons are strongly confined in their respective layers because of the large separation in energies between the GaAs and AlAs optical phonon branches. All the observed GaAs Raman peaks have been explained quantitatively by this confinement model using the phonon dispersion curves of bulk GaAs. The situation in GaAs/$Al_xGa_{1-x}As$ quantum wells has been complicated by the so-called "two-mode" behavior of optical phonons in $Al_xGa_{1-x}As$. The reason is that the energy of the GaAs-like LO phonons in $Al_xGa_{1-x}As$ lies very close to that of the GaAs LO phonons. It is, therefore, possible that GaAs LO phonons can propagate through the $Al_xGa_{1-x}As$ barriers provided the Al fraction x in the barrier is small. However, the important issue of whether the GaAs LO phonons can propagate through $Al_xGa_{1-x}As$ at a critical value of x has been investigated only by theoreticians and not yet extensively by experimentalists [4-7]. We note that Kash and coworkers have investigated the localization of phonons in $Al_xGa_{1-x}As$ alloys using the NOP technique [12]. They also predicted a decrease in the NOP population if the phonons become localized. They investigated a series of $Al_xGa_{1-x}As$ samples with the Al fraction x=0.07, 0.11 and 0.24. They found that the NOP population could be observed even for x=0.24. Hence they concluded that, if there is a transition from propagating

phonons to localized phonons in $Al_xGa_{1-x}As$, this transition occurs at x>0.24. In a quantum well sample with well width L=500 Å. They found that wave vector conservation is relaxed to the point that forward and backward scattering give identical results. This is consistent with our expectation. Because bulk GaAs LO phonon probed by Raman back scattering has a wavelength about 900 Å (Fig. 5-1), a 500 Å quantum well will put some geometrical constraint on the phonon propagation, causing a spread in phonon wave vector in magnitude comparable to Q_0. In this case the scattering geometry becomes relatively unimportant in determine the NOP occupancy. The strong dependence of the localization properties of the GaAs LO phonons on the Al fraction in the $Al_xGa_{1-x}As$ barrier we deduced from our experiments is also in good qualitative agreement with some recent theoretical work.

The fact that the onset of the propagating-to-localized transition of the LO phonons coincides roughly with the direct-to-indirect band gap transition in $Al_xGa_{1-x}As$ as a function of x also raises the question whether the sudden decrease in the NOP population with increasing x may be explained by the lowering of the X conduction band valleys relative to the conduction band minimum at the zone center. If this direct-to-indirect cross-over of the $Al_xGa_{1-x}As$ band gap is included in our model calculation then its contribution to the decrease of the NOP population is expected to be less than 50% rather than by a factor of ten. The effect of intervalley scattering on the efficiency of NOP generation has been studied in bulk GaAs by Collins and Yu [8]. They found that this effect reduced the NOP population by only about 30%. Since most of the high energy electrons excited by the laser pulses which undergo intervalley scattering will eventually return to the Γ valley, most of them will still lose their energies in the Γ valley by

emitting NOP, intervalley scattering is not expected to be important to our model. On the other hand, the direct-to-indirect bandgap cross over may be related to a second order phase transition, as has been suggested recently [13]. In this case, one cannot rule out the possibility that the confined-to-propagating transition of optical phonons in $Al_xGa_{1-x}As$ and the direct-to-indirect transition of the bandgap may have the same physical origin.

Finally, we can ask what is the accuracy of the value of x we deduced for the transition from a propagating to a localized state for phonons in $GaAs/Al_xGa_{1-x}As$ quantum wells. By assuming a bulk-like hot electron relaxation, we tend to overestimate the NOP, for in quantum wells confinement of electrons can greatly suppress the generation of small q hot phonons [14, 15]. Therefore, the experimental NOP is expected to be smaller than the calculated value based on the bulk-like hot electron relaxation approximation. Hence we probably underestimate the coherence length of the LO phonons, especially for large values of x. In other words, it is possible that the propagating to localized transition occurs closer to x=0.4 rather than x=0.2. This result would be in better agreement with the theoretical results of Fertig and Reinecke [4] who conclude that optical phonons can be propagating for x as large as 0.4.

In summary, we have studied the confinement and propagation of LO phonons in $GaAs/Al_xGa_{1-x}As$ quantum wells, and developed a simple model to correlate the NOP population to the coherence length of the GaAs LO phonons. We argue that the NOP population can be a sensitive measure of the spatial extent of the LO phonons. Using our model, we deduced the coherence length of the GaAs LO phonons in $GaAs/Al_xGa_{1-x}As$ quantum wells as a function of the Al fraction x from the experimental NOP population measured by Kim *et al.*.

References

[1] D. S. Kim, A. Bouchalkha, J. M. Jacob, J. F. Zhou, J. J. Song, and J. F. Klem, Phys. Rev. Lett. **68**, 1002 (1992).

[2] J. M. Jacob, D.S. Kim, A. Bouchalkha, J. J. Song, J. F. Klem, H. Hou, C.W. Tu, and H. Morkoç, Solid State. Commun. **91**, 721 (1994).

[3] D. S. Kim, A. Bouchalkha, J. M. Jacob, J.J. Song, J. F. Klem, H. Hou, C. W. Tu, and H. Morkoç, Phys. Rev. B **51**, 5449 (1995).

[4] H. A. Fertig and T. L. Reinecke, Phys. Rev. B **49**, 11168 (1994).

[5] L. Colombo, C. Molteni and L. Miglio, *Proceedings of the 21st International Conference on the Physics of Semiconductors*, edited by P. Jiang and H.Z. Zheng (World Scientific, Singapore, 1992), pp. 777-780.

[6] F. Bechstedt H. Grecke, and H. Grille, Phys. Rev. B **47**, 13540 (1993).

[7] C. Molteni, L. Colombo, L. Miglio, and G. Benedeck, Phys. Rev. B **50**, 11684 (1994).

[8] C. L. Collins and P. Y. Yu, Phys. Rev. B **30**, 4501 (1984).

[9] L. G. C. Rego and A. C. S. Algarte, Phys. Rev. B **49**, 7257 (1994).

[10] K. Krâl, Phys. Rev. B **50**, 7988 (1994).

[11] See for example, B. Jusserand, D. Paquet and A. Regreny, Phys. Rev. B **30**, 6245 (1984).

[12] J. A. Kash, J. M. Hvam, J. C. Tsang, and T. F. Kuech, Phys. Rev. B **38**, 5776 (1988); J.A. Kash, S. S. Jha, and J. C. Tsang, Phys. Rev. Lett. **58**, 1869 (1987).

[13] B. Koiler and R. B. Capaz, Phys. Rev. Lett. **74**, 769 (1995).

[14] See for instance, J. F. Ryan, in *Hot Carriers in Semiconductor Nanostructures: Physics and Applications*, edited by J. Shah (Academic Press, Boston, 1992).

[15] D. S. Kim and P. Y. Yu, in *Ultrafast Laser Probe Phenomena in Bulk and Microstructure Semiconductors*, edited by R. R. Alfano, SPIE Symposia Proceedings No. 1282, p. 39 (SPIE, Bellingham, 1990).

Figure Captions for Chapter V

Fig. 5-1 A schematic diagram of Raman backscattering geometry. $\mathbf{k}_i$, and $\mathbf{k}_s$, are, respectively, the incident and scattered photon wave vectors outside the sample. Similarly, $\mathbf{k}_i$' and $\mathbf{k}_s$' are incident and scattered wave vectors inside bulk GaAs. The Raman active LO phonon has a wave vector roughly equal to $Q_0=2k_i'=2nk_i$ (n is the index of refraction), since $k_i \approx k_s$ and $k_i' \approx k_s'$. The wave length of the Raman active LO phonon is then $\lambda_0 \equiv 2\pi/Q_0 \approx 900$ Å for the excitation photon energy of 2 eV.

Fig. 5-2 A schematic diagram of Raman backscattering in $GaAs/Al_xGa_{1-x}As$ with folded or propagating optical phonons (thus corresponding to small x). The Raman active GaAs LO phonon wave function, which is in the form of $\exp(iQ_0z)u(z)$ (u: periodic function with period L_z+L_b), is schematically represented by solid lines. The dominant Fourier component of this wave function occurs at $q=Q_0$.

Fig. 5-3 A schematic diagram of Raman backscattering in $GaAs/Al_xGa_{1-x}As$ with confined or localized optical phonons (thus corresponding to large x). The localized GaAs LO phonon wave function is schematically represented by solid lines. In this case, the wave vectors probed by Raman scattering is determined not by GaAs bulk property and photon energy, but by the well width.

Fig. 5-4 Nonequilibrium LO phonon population at t=1 ps as a function of wave vector q, assuming delta function excitation at t=0 with 2 eV incident photons. The region of

wave vectors probed by Raman scattering is denoted as a vertical solid line. Inset: same NOP distribution plotted on a semi-logarithmic scale.

Fig. 5-5 Nonequilibrium LO phonon population at t=1 ps as a function of q, assuming delta function excitation at t=0 with 2 eV incident photons (solid lines). The Fourier transform of a Gaussian wave function, F(q) with η=100 Å, is represented by dotted lines. In this case, the region of wave vectors probed is much more extended, so that contributions from small N_q's are significant.

Fig. 5-6 A schematic diagram of the Bloch wave function with a Gaussian envelope function (Eq. (5-14)). The size of the wave packet is ξ. For convenience, Q_0 is set to zero.

Fig. 5-7 Non-equilibrium phonon occupancy as a function of the coherence length ξ calculated from the results of Fig. 5-4 and Eq. (5-14).

Fig. 5-8 Experimental non-equilibrium phonon occupancy (solid squares) probed by picosecond Raman scattering in GaAs/$Al_xGa_{1-x}As$ quantum wells as a function of alloy concentration x. Smooth fit to the data points is represented by the solid line.

Fig. 5-9 Coherence length ξ deduced from the results of Fig. 5-7 and the analytical fit of Fig. 5-8, as a function of alloy concentration x in GaAs/$Al_xGa_{1-x}As$.

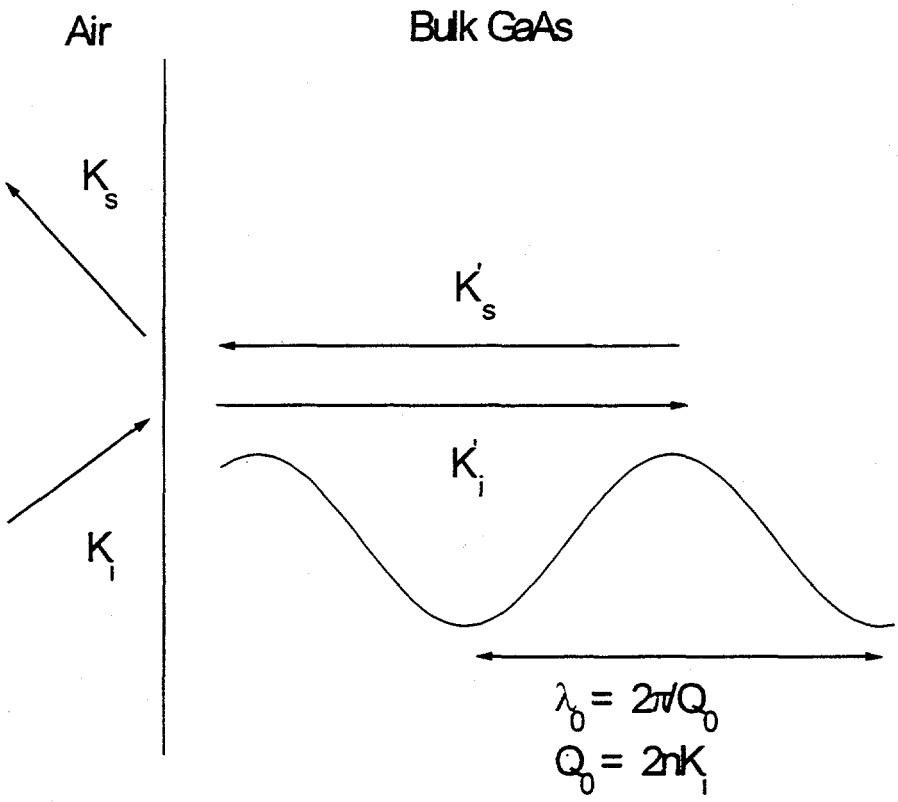

Figure 5 - 1

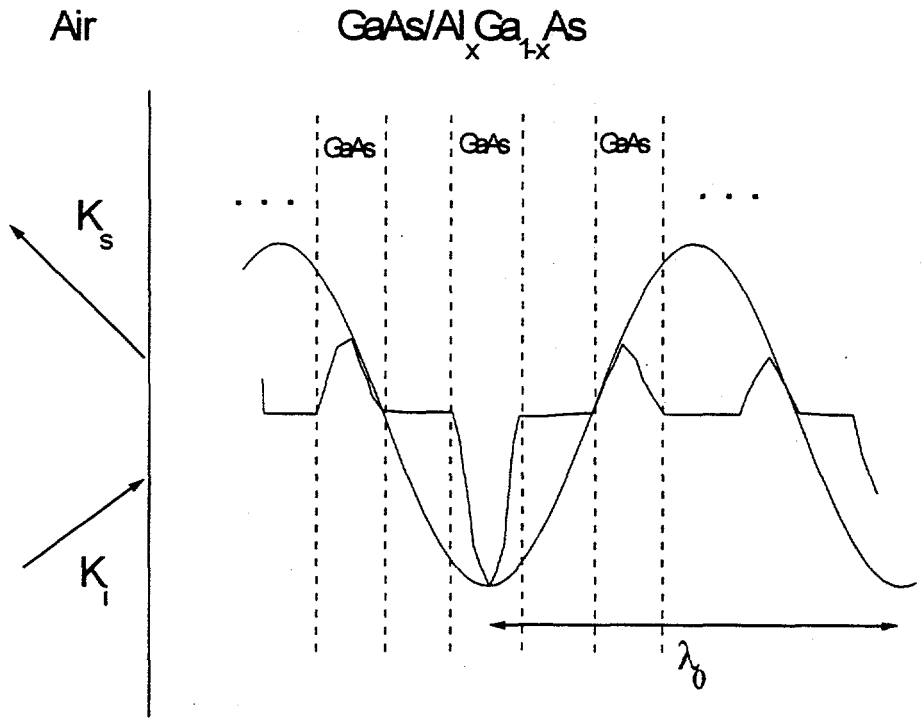

Folded or propagating phonons

Figure 5 - 2

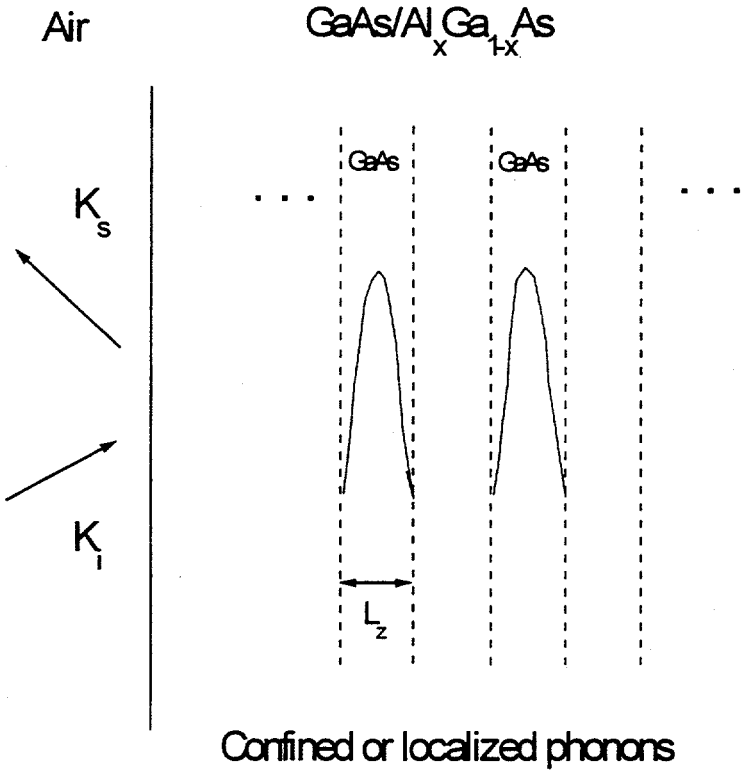
Air
GaAs/Al$_x$Ga$_{1-x}$As
GaAs
GaAs
K_s
K_i
L_z
Confined or localized phonons

Figure 5 - 3

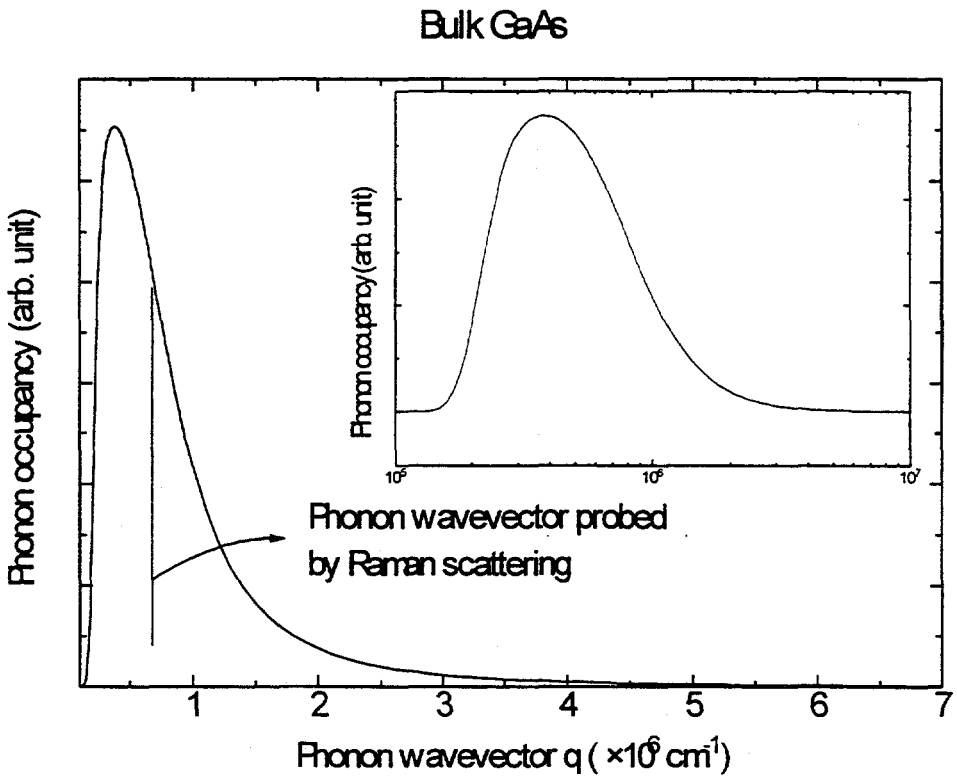
Bulk GaAs
Phonon occupancy (arb. unit)
Phonon occupancy(arb.unit)
Phonon wavevector probed
by Raman scattering
1
2
3
4
5
6
7
Phonon wavevector q (×10^6 cm^-1)

Figure 5 - 4

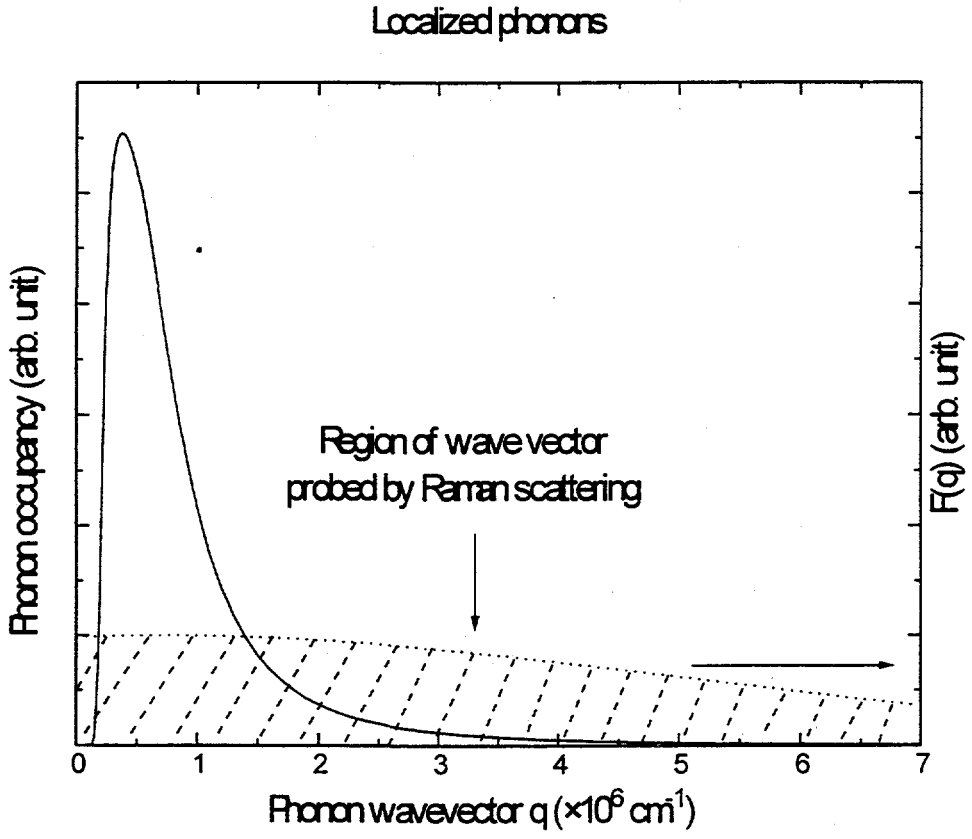
Localized phonons
Phonon occupancy (arb. unit)
F(q) (arb. unit)
Region of wave vector
probed by Raman scattering
0
1
2
3
4
5
6
7
Phonon wavevector q (×10^6 cm^-1)

Figure 5 - 5

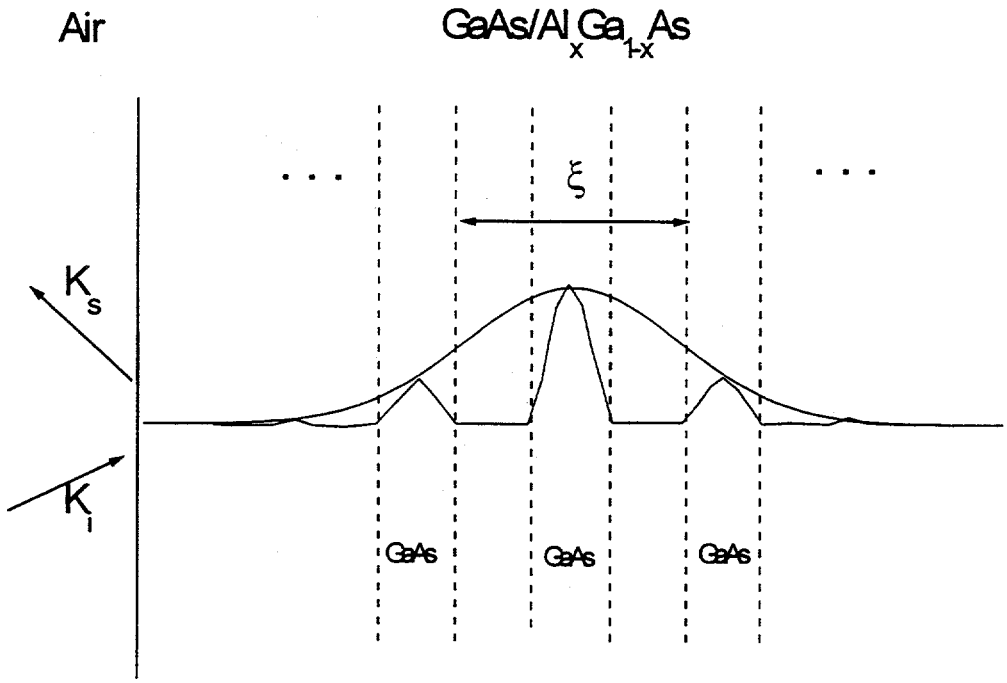

Phonon wave function with finite spatial extent ξ

Figure 5 - 6

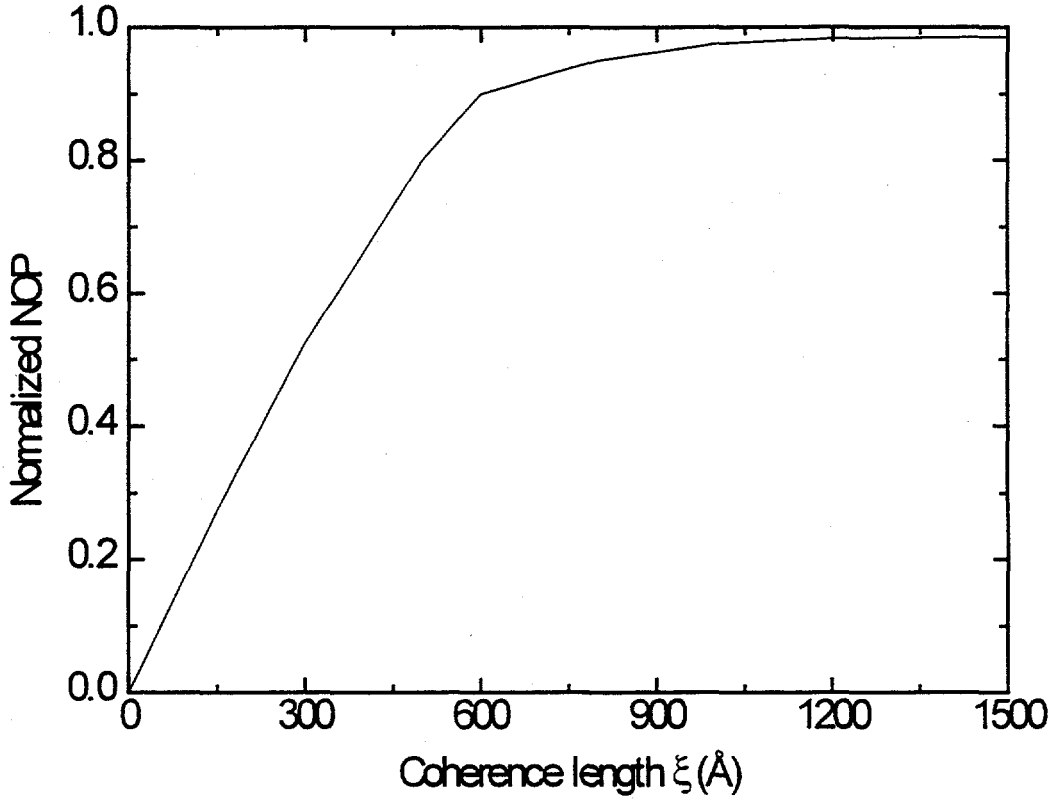
1.0
0.8
0.6
0.4
0.2
0.0
Normalized NOP
0
300
600
900
1200
1500
Coherence length ξ (Å)

Figure 5 - 7

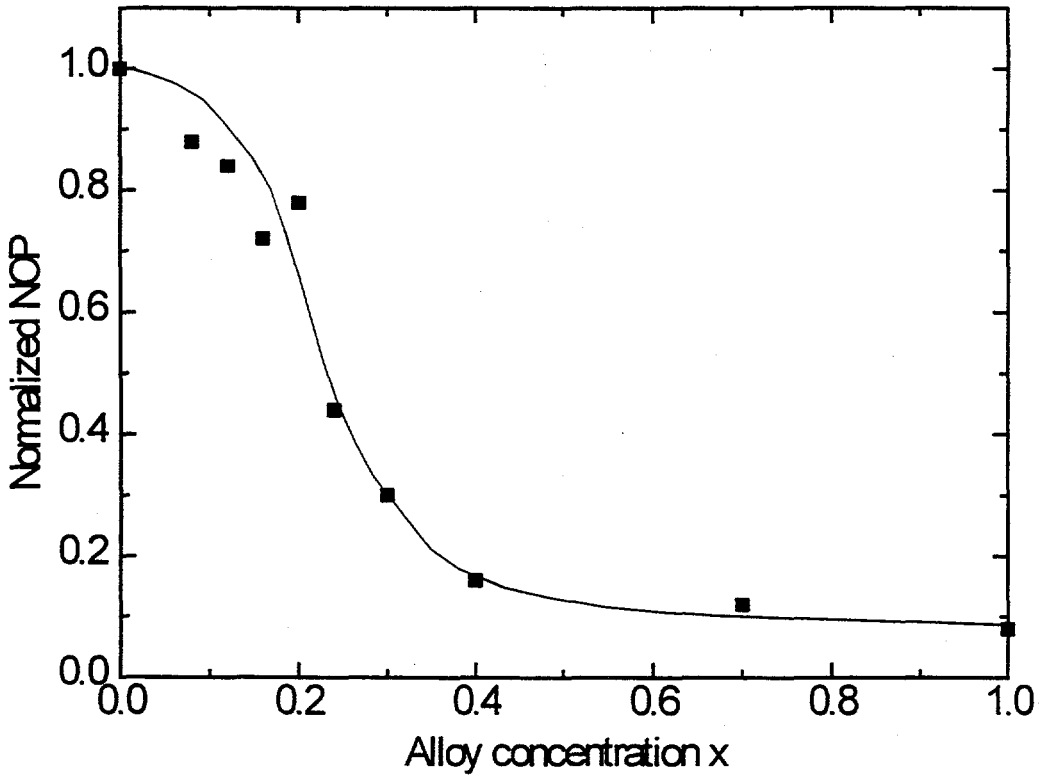
Normalized NOP
1.0
0.8
0.6
0.4
0.2
0.0
0.0
0.2
0.4
0.6
0.8
1.0
Alloy concentration x

Figure 5 - 8

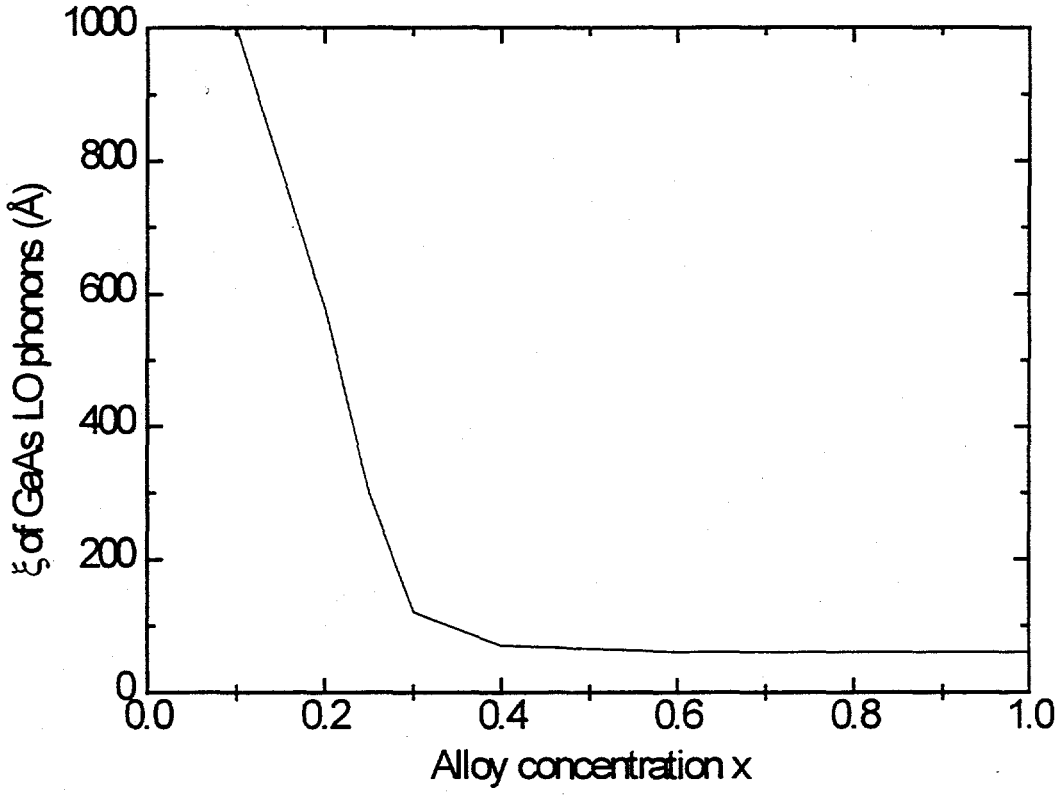
1000
800
600
400
200
0
ξ of GaAs LO phonons (Å)
0.0
0.2
0.4
0.6
0.8
1.0
Alloy concentration x

Figure 5 - 9

Chapter VI: Conclusions

In this thesis we have studied non-equilibrium phonons in GaAs/$Al_xGa_{1-x}As$ quantum wells through model calculations and picosecond time-resolved Raman scattering and photoluminescence experiments. We have investigated three subjects, the resonant intersubband scattering of optical phonon (RISOP); photoluminescence of quantum wells under high intensity excitations; and propagation and confinement of optical phonons in quantum wells. In studying RISOP, we have addressed the issue of whether one can measure the phonon occupancy in quantum wells and superlattices using the technique of Raman scattering. We have shown experimentally that by taking into account the time-reversal symmetry relationship between the Stokes and anti-Stokes Raman cross sections, one can correct the spurious effect caused by resonant Raman scattering and successfully determine the phonon occupancy in quantum wells. We applied our technique to study RISOP in GaAs/AlAs quantum wells. Our results suggest that interface roughness in quantum wells and superlattices play an important role in the resonant Raman scattering. The breakdown of quasi-momentum conservation due to interface roughness enables resonant Raman scattering to probe a wide range of in-plane phonon wave vectors. The consequence of this change in the Raman-active phonon wave vectors is that one will be able to observe non-equilibrium phonon in Raman scattering which, in the general cases, would not be possible if quasi-momentum is strictly conserved in Raman scattering. This also means that the chance that one will measure the enhancement in non-equilibrium phonon occupancy predicted by RISOP when the

intersubband separation is equal to the LO phonon energy is greatly reduced. Our experimental results agree with our model calculations based on the Huang-Zhu model when we choose the size of the smooth regions at the interface to be of the order of 100 Å. This size deduced from our experiment is consistent with the result of recent experimental work on acoustic phonon scattering in the literature. In our experiments on the photoluminescence from highly excited GaAs/AlAs quantum wells, we have shown that band non-parabolicity has little effect on the electron energy levels in quantum wells with width of about 200 Å. The electron subbands are found to be well described by the parabolic band approximation even for energy as much as 250 meV above the bottom of the subband. This surprising finding may require additional theoretical investigation. In studying the confinement and propagation of optical phonons, we have combined our model calculation with the experimental results of *Kim et al.*, and shown that Raman scattering of non-equilibrium phonons can be a sensitive measure of the spatial extent of the LO phonons, and can be used to detect the transition of phonon mode from a propagating state to a confined state. We have correlated the measured non-equilibrium phonon occupancy to the coherence length ξ of the LO phonons, and deduced ξ of the GaAs LO phonons in GaAs/$Al_xGa_{1-x}As$ quantum wells as a function of the aluminum concentration x.